Dual-Pulse Laser Induced Breakdown Spectroscopy in the Vacuum Ultraviolet with Ambient Gas: Spectroscopic Analysis and Optimization of Limit of Detection of Carbon and Sulfur in Steel

A THESIS SUBMITTED FOR THE DEGREE OF

DOCTOR OF PHILOSOPHY

PRESENTED TO:

THE SCHOOL OF PHYSICAL SCIENCES AND TECHNOLOGY,
FACULTY OF SCIENCE AND HEALTH,
DUBLIN CITY UNIVERSITY

AUTHOR

XI JIANG

B.Sc., M.Sc.

Research Supervisors

PROF. EUGENE KENNEDY, PROF. JOHN COSTELLO

Declaration

I hereby certify that this material, which I now submit for assessment on the programme of study leading to the award of Ph.D is entirely my own work, and that I have exercised reasonable care to ensure that the work is original, and does not to the best of my knowledge breach any law of copyright, and has not been taken from the work of others save and to the extent that such work has been cited and acknowledged within the text of my work.

Signed: _____ **ID No.:**

Date: _____

For my mother

Acknowledgements

First and foremost, sincere thanks to Prof. Eugene Kennedy and Prof. John Costello, both as my supervisors for giving me the opportunity to study and work in DCU and for guiding my work.

Many thanks to postdocs Paddy Hayden, Pat Yeates, Patrick Casey for kind help and useful chat, and to senior/previous members of the physics group in DCU: Eoin O'Leary, Mohamed, John, Caroline, Phil, Padraig, Conor, Mairead, Patrick, Brian, Ricky, Mahua.

Thanks to all the current colleagues in DCU physics department: Colm, Conor, Ruth, Mossy, Eanna, Seamus, Nicky, Hooiling, Catherine, Jack, Joe, Darrick, Justin, Yang, Barry, Rajani, Aurora, Barbara and many others.

Thanks to Ricarda and Nadia who were two short term visiting students here, thank you both for co-working in the lab and bringing joy to the group!

Thanks to the school secretaries Shiela and Lisa for taking care of the paper works, and to Daz, Ray Murphy, Pat Wogan, Alan Hughes for technical support. Thanks also to the entire staff and faculty of physics school and NCPST.

Thanks also to all my friends including my old friends in China, my college mates (mostly) in the US, my Chinese friends in Ireland and the local Irish friends, as well as friends in Europe and other places around the world. Thank you for making my life so wonderful.

Finally, my most sincere thanks to my family, thank you for supporting my adventure so far both spiritually and financially.

Abstract

Laser Induced Breakdown Spectroscopy (LIBS) in the vacuum ultraviolet (VUV) spectral region was applied to standard steel samples in dual-pulse excitation mode with an ambient gas. Two lasers were employed in collinear geometry, one as an ablation laser (Spectron: 200mJ/15ns) and the other a reheating laser (Surelite: 665mJ/6ns).

A dual-pulse scheme was applied to the traditional single-pulse LIBS and led to a significant enhancement, increasing both the signal to background ratio (SBR) and concomitantly the limit of detection (LOD). Three types of gases, nitrogen, argon and helium were investigated individually as ambient environment. The variation in signal gain with ambient gas pressure was measured.

The feasibility study of dual-pulse (DP-) LIBS) in the deep VUV spectral region was carried out by optimizing a number of parameters for limit-of-detection (LOD) calibration. The pulse energy choices of laser beam, the signal recording position for the space-resolved detection system, the CCD exposure time and the number of laser shots accumulated for a spectrum were among the first few parameters optimized for the current LIBS system.

The dependence of emission intensity on focusing conditions was investigated for both single-pulse (SP) and dual-pulse (DP) mode. In DP mode, the lens-to-target distance of the reheating pulse was varied while the ablation pulse was held at a fixed focusing condition. The optimal focusing for signal enhancement was found to be about 10 mm under the sample surface for single-pulse laser beam and 5 - 10 mm for the reheating pulse in dual-pulse mode.

The effect of inter-pulse delay on the emission intensity were studied in vacuum and in ambient gas background in the dual-pulse configuration. An intensity peak at about 100 ns and an intensity revival in the μs range were observed on the intensity vs. inter-pulse delay curves. The optimal inter-pulse delay was considered to be 100 ns. The μs range intensity plateau led to a discussion on the plasma expansion dynamics in dual-pulse mode.

Finally the limit of detection (LOD) of C and S in steel was improved by a factor of 2 or more over single pulse LIBS with the combination of optimized experimental parameters. The initial measurements and results suggest that DP-LIBS in an ambient gas environment for VUV spectroscopy is practicable and brings with it even further improvement of the LIBS performance in the VUV regime.

Thesis Organization

This thesis is divided into 10 chapters as follows:

Chapter 1 - *Laser produced plasmas in spectroscopy*

The first part of the thesis provides some of the theoretical aspects of laser produced plasmas including a fundamental overview of laser produced plasmas and the atomic processes involved. The principles for using laser plasmas as light sources for quantitative analytical spectroscopy is explained at the end of this chapter.

Chapter 2 - *The fundamentals of LIBS*

This chapter is a general introduction to Laser Induced Breakdown Spectroscopy (LIBS) and contains a literature review of LIBS development. A particular emphasis is placed on the basics of studies performed on determining concentrations of light elements in steel in terms of the limit of detection (LOD).

Chapter 3 - *The experimental setup*

This chapter contains a description of the equipment used in the experiments performed for the present work including details of the laser system employed, the spectrometers, operational characteristics and the method by which radiation from the laser plasma was captured.

Chapter 4 - *The basic LIBS analysis*

This chapter demonstrates how LIBS is used for direct detection of trace elements in steels. A number of hardware parameters including the laser pulse energy choices, observing position for space-resolved detection system, CCD exposure time and number of shots accumulated for a spectrum are discussed and optimized. Following the basic settings, the computing processes for limit of detection (LOD) calibration including wavelength calibration and the data handling process are also introduced. The complete procedure of spectroscopic analysis by a basic LIBS system is summarized at the end of this chapter.

Chapter 5 - *The improvement techniques*

This chapter provides a comprehensive study of dual-pulse LIBS in ambient gas environments. Firstly the dual-pulse or DP-LIBS and the ambient gases are introduced to the basic LIBS setup. Then the DP-LIBS operation and the VUV emission in several ambient gases are studied. A series of spectral comparisons are provided. Emphasis is placed on the combination of dual-pulse and ambient gas techniques as a further improvement to the conventional LIBS system.

Chapter 6 - *The effects of laser beam defocusing*

The laser beam defocusing is one of the parameters which can affect the signal intensity significantly in both single- and dual-pulse LIBS. This chapter provides a

detailed investigation of the effect of laser beam defocusing. In single-pulse mode, the defocusing effect means the influence of the relative distance between the focal point and the sample surface on the plasma emission behaviors. In dual-pulse mode, the defocusing effect refers to the defocusing effect of the second/reheating laser beam. The observations and discussions in both single- and dual-pulse mode are provided in this chapter.

Chapter 7 - *The effect of inter-pulse delay*

Another worth-noting effect in the optimization process for dual-pulse LIBS is the effect of inter-pulse delay. At certain inter-pulse delay times, the emission intensity was dramatically enhanced. The optimal inter-pulse delay of 100 ns has been achieved during the optimization process in chapter 5. When the inter-pulse delay was extended to the μs range, an intensity revival was found in the cases with ambient gas. Efforts have been made to investigate these interesting observations. Questions are asked and addressed within the scope of the current work.

Chapter 8 - *Emission enhancement mechanisms in dual-pulse LIBS*

Two emission enhancements have been clearly shown and proved in the previous chapter 7 and the unique characteristics (i.e. ambient gas and pressure dependence) of the second enhancement indicate a new enhancement mechanism distinct from the first one. Further investigations regarding the enhancement mechanisms in dual-pulse LIBS, especially with low-pressure ambient gases, have been performed. A process of "phased enhancement" is proposed along with a brief literature survey seeking more evidences on multi-phase enhancement.

Chapter 9 - *Limit of detection calculation and comparison*

Having optimized all possible parameters in dual-pulse LIBS in ambient gas, the limit of detection (LOD) of carbon (C) and sulphur (S) in steel are extracted under optimized conditions. The comparisons are also provided which include the goodness of LOD calibration curves and the final LOD values obtained under different conditions. Finally the best LOD results achieved under the optimal conditions in the current work are compared to those in the literature.

Chapter 10 - *Conclusions and future work*

This final chapter provides a summary of the experimental work and the general conclusions formed as a result of the above research. Some future interests are outlined in the context of the current research direction.

To help the reader with a clear view of the thesis, the thesis structure is summarized in figure 1.

Introductions	Chapter 1 Laser plasmas Chapter 2 LIBS introduction	Theories of Laser induced plasma and introduction to LIBS
	Chapter 3 Experimental	Experimental
Results	Chapter 4 Basic LIBS Chapter 5 Improvements	Basic LIBS procedure and dual-pulse (DP) LIBS in ambient gas(es)
	Chapter 6 Defocusing Chapter 7 Inter-pulse delay Chapter 8 Mechanism	Further discussions of some topics on LIBS including Laser beam defocusing; Inter-pulse delay; Enhancement mechanisms of DP-LIBS
	Chapter 9 L.O.D.	Final calibration of limit of detection (LOD)
Conclu- sions	Chapter 10 Conclusions	Summary

Figure 1: Outline of the thesis.

Contents

1 Introduction to Laser Plasmas and Vacuum Ultraviolet Spectroscopy 5

1.1 Plasma formation and post-breakdown phenomena on solid targets . 6
1.2 Atomic processes in laser induced plasmas 7
1.2.1 Free-free transitions 7
1.2.2 Free-bound transitions 8
1.2.3 Bound-bound transitions 8
1.3 General characteristics of plasmas 9
1.3.1 Debye sheath and plasma frequency 9
1.3.2 Thermodynamic equilibrium in a plasma 11
1.4 Quantitative spectroscopy in the VUV 12
1.5 Analytical figures of merit 16
1.6 Summary 17

2 Introduction to Laser Induced Breakdown Spectroscopy 18

2.1 An overview of LIBS 19
2.1.1 LIBS fundamentals 19
2.1.2 Brief outline of LIBS instrumentation 20
2.1.3 LIBS Applications 20
2.2 Literature survey of LIBS 22
2.2.1 A brief history of LIBS 22
2.2.2 LIBS in recent years 24
2.3 Aims and objectives of the present work 26
2.4 Summary 27

3 Equipmental System 28

3.1 The laser system 30
3.2 Target chamber and targets 32
3.3 GCA and the spectrometer 35

3.4 The Rowland circle and off-Rowland mount . . . 37
3.5 Resolving power of the spectrometry system . . . 40
3.6 Signal detection and recording system . . . 42
3.7 Summary . . . 44

4 Basic LIBS: Typical LIBS Analysis Process 45
4.1 Choice of laser pulse energies . . . 46
4.2 Time-integrated space-resolved LIBS system . . . 47
4.3 The optimal observing position . . . 49
4.4 CCD exposure time and number of shots accumulated . . . 51
4.5 Wavelength calibration . . . 51
4.6 Data handling . . . 55
4.7 LOD calculation . . . 58
4.8 Summary . . . 58

5 Dual-pulse LIBS in the VUV in Ambient Gases: Preliminary Results 61
5.1 Introduction of two major technical improvements to basic LIBS . . . 62
5.2 Experimental settings for dual-pulse LIBS in ambient gases . . . 63
5.3 Dual-pulse LIBS operation . . . 64
5.3.1 Inter-pulse delay generator . . . 65
5.3.2 Dual-pulse LIBS spectrum . . . 66
5.3.3 Optimal inter-pulse delay time . . . 69
5.4 Ambient gases . . . 72
5.4.1 Emission in ambient gases . . . 72
5.4.2 VUV light transmission in ambient gases . . . 77
5.5 Summary . . . 82

6 Effects of Laser Beam Defocusing 83
6.1 Defocusing effect in single-pulse mode . . . 84
6.1.1 Observations of the laser beam defocusing effect . . . 84
6.1.2 Discussion of defocusing effect in single-pulse mode . . . 85
6.1.3 Summary of on-focus, before- and beyond-focus defocusing conditions . . . 88
6.2 Defocusing effect in dual-pulse mode . . . 89
6.2.1 Observations of the reheating pulse defocusing effect . . . 89
6.2.2 Discussions of the reheating pulse defocusing effect . . . 90
6.3 Summary . . . 90

7 The Effect of Inter-Pulse Delay **92**
7.1 The inter-pulse delay effect in vacuum and in ambient gas 93
7.2 The 100 ns peak 93
7.3 The plateau and three questions about it 95
7.4 Is the plateau an actual intensity revival? 95
7.4.1 Inter-pulse delay in nitrogen 95
7.4.2 Inter-pulse delay in helium 98
7.4.3 Inter-pulse delay in argon 98
7.5 What made the plateau appear? 102
7.5.1 Gas pressure vs. plateau: a case study in argon 102
7.5.2 Gas pressure vs. plateau: nitrogen and helium 104
7.5.3 Ambient gas only experiments 105
7.5.4 Inter-pulse delay effect is independent of emitting elements . 106
7.6 Could the plateau be enhanced more significantly than the first peak? 106
7.7 Summary 108

8 Emission Enhancement Mechanisms in Dual-Pulse LIBS **109**
8.1 Introduction to the expansion mechanics of laser induced plasma . . 110
8.2 The phased enhancement 113
8.3 A survey of inter-pulse delay effect on DP-LIBS in the UV/IR compared with DP-LIBS in the VUV 116
8.4 Summary 122

9 Limit of Detection **124**
9.1 LOD Calibration Curves for Carbon and Sulphur 125
9.1.1 LOD calibration on the C^{2+}97.7 nm line in single- and dual-pulse mode 125
9.1.2 LOD calibration on the S^{4+}78.65 nm line in single- and dual-pulse mode 128
9.2 Calculated LOD Values Under Different Conditions 128
9.3 Optimized LOD Values for C and S 133
9.4 Summary 136

10 Conclusions and Future Work **138**
10.1 General Conclusion of Dual-Pulse LIBS in Ambient Gas Condition . 138
10.2 Future Work on LIBS 140
10.2.1 The understanding of the LIBS process 140
10.2.2 The development of the dual-pulse LIBS technique 141

Summary **143**

Publications and Conference Presentations **145**

Appendices **146**

A Criteria for Thermodynamic Equilibrium **146**

B Kirchhoff's Law of Radiation **149**

C A Quick Note on Atomic Spectral Lines **151**

D More Details on Inter-pulse Delay Time Investigations **154**

E Goodness-of-Fit Statistics **157**

Chapter 1

Introduction to Laser Plasmas and Vacuum Ultraviolet Spectroscopy

This chapter deals with the fundamental physics of laser-induced plasmas including the atomic processes involved in the plasma expansion and vacuum ultraviolet (VUV) spectroscopy, followed by an introduction to the figures of merit which are crucial to laser-induced plasma VUV emission measurements.

1.1 Plasma formation and post-breakdown phenomena on solid targets

When a Q-switched Nd:YAG laser pulse is focused onto a solid target with sufficient energy, a certain amount of material is vaporized and thus a plasma is formed on the target surface. Reported values of the laser-induced plasma breakdown threshold of a solid target lie between 10^8 W/cm^2 and 10^{10} W/cm^2 [1]. For the work reported here, the maximum Nd:YAG laser pulse energy lay between 600 mJ and 800 mJ, operating at its fundamental wavelength 1064 nm with a 6 ns pulse duration. Focused by a spherical lens with a spot diameter around 100 μm, the calculated power density approached 10^{12} W/cm^2, well above the breakdown threshold.

When the laser irradiance is high enough to initiate a plasma on the sample surface, some of the pulse energy heats, melts and vaporises material into a plume above the target surface. Almost simultaneously, some seed electrons are produced by one or more processes such as multiphoton ionization, laser assisted photoabsorption, etc. to form a weakly ionized plasma. These seed electrons allow for further laser radiation absorption by the process of inverse bremsstrahlung which in turn causes further ionization. The process is regenerative and results in avalanche ionization since an increase in ionization rate results in an increase in laser light absorption which in turn results in an increase in ionization rate and so on. Eventually, the plasma can become opaque to the laser pulse and the surface is shielded from it. The plasma density at which the plasma becomes opaque to the incoming laser light is termed as the critical density and can be calculated using equation 1.1.

$$n_c = \frac{m_e \omega^2}{4\pi e^2} \cong \left(\frac{10^{21} \mu m}{\lambda^2} \right) /cm^3 \tag{1.1}$$

Symbols in the equation are:
m_e electron mass;
ω frequency of the laser radiation;
e electron charge;
λ laser wavelength measured in μm.

The critical density for the fundamental wavelength (1064 nm $\approx$ 1 μm) of a Nd:YAG laser is approximately 10^{21} cm^{-3}. When the plasma density reaches the critical value, a large portion of the incident laser energy is reflected by the plasma at and near the critical density zone. At this stage, the plasma starts to expand rapidly from the initial point. The expansion reduces the electron density, the laser

light is once again able to pass through the plasma and heat the target. This cyclical process continues until the termination of the laser pulse(s). After the excitation process, the plasma initiated by the laser pulse expands into vacuum or ambient atmosphere. During the plasma formation and evolution, collisional ionization and recombination processes dominate energy transfer in the plasma.

1.2 Atomic processes in laser induced plasmas

Atomic processes are key mechanisms of energy transfer between various species in the plasma. The significance of these processes depends on the populations of different energy levels and the ionization stages in the plasma. The ionization stages depend on the electron temperature and density of the plasma [2]. Identification of each process during the plasma evolution provides a better understanding of the plasma behavior under various conditions. The following subsections describe three fundamental atomic processes occurring in the plasma which are: free-free, free-bound and bound-bound transitions.

1.2.1 Free-free transitions

Free-free transitions are processes where two or more particles are involved in an interaction after which they remain free (Hughes, 1975 [3]). Bremsstrahlung radiation is caused by collisions between free electrons, ions or neutrals. It occurs mainly during the early stages of the laser plasma's lifetime when the density is high. It can be represented by the pseudo-equation (using X to represent the ion or neutral, e^* or e^{**} for a free electron, the kinetic energy of electron e^{**} (i.e., before the collision) is greater than that of electron e^* (i.e., post-collision) and γ for a photon):

$$X + e^{**} \rightarrow X + e^* + \gamma \tag{1.2}$$

The opposite process is termed inverse Bremsstrahlung. This interaction can be described by:

$$X + e^* + \gamma \leftrightarrow X + e^{**} \tag{1.3}$$

In inverse Bremsstrahlung, a free electron absorbs a fixed energy laser photon in the vicinity of a nearby ion. It is raised to a higher energy level and hence its kinetic energy is increased. This process is considered to be the main mechanism of laser heating and ionization in the formation of laser plasmas. That is to say, it is the main source of energetic electrons which ionize the target during the laser pulse.

1.2.2 Free-bound transitions

Free-bound processes can happen in one of two ways. In electron collisional ionization, an electron collides with an atom or ion, with the result that another electron is freed from the parent particle, while the exciting electron remains free, with less kinetic energy. The inverse process, three-body recombination, involves a collision between an electron and an ion resulting in the capture of the electron, with the excess energy absorbed by a second free electron in close proximity. These processes are shown as:

$$X^{n+} + e^{**} \leftrightarrow X^{(n+1)+} + e^{*} + e^{*} \tag{1.4}$$

Photoionisation happens when a photon of energy greater than the ionization potential of the target atom or ion is absorbed by an electron. The electron then has enough energy to escape the atomic or ionic potential with an energy given by the usual photoelectric process equation:

$$E = \frac{1}{2}mV^2 = hv - E_i \tag{1.5}$$

where $\frac{1}{2}mV^2$ is the kinetic energy of the electron, hv is the incident photon energy and E_i is the ionization potential of the atom/ion. This "atomic photoelectric effect" can be represented as:

$$X^{n+} + hv \leftrightarrow X^{(n+1)+} + e^{*} \tag{1.6}$$

Therefore, the inverse or radiative recombination process is simply the capture of an electron by an ion with the surplus energy emitted as a photon. In general, free-bound processes occur at intermediate times in the plasma lifetime when the plasma is in transition from continuum-dominated to line-dominated radiation [4].

1.2.3 Bound-bound transitions

Bound-bound interactions are responsible for the discrete line emission from the various atomic species in the plasma. Mainly occurring when the bulk of the plasma has cooled significantly from the initial formation, line radiation from the plasma is used mostly for plasma diagnostics and also LIBS studies. These processes again consist of radiative or collisional interactions. In collisional interactions, two atomic species collide with each other with a net energy loss from one particle and a corresponding energy gain by the other. Collisional de-excitation is simply the inverse of this process: an excited electron drops into a lower energy

state of the atom or ion with the surplus energy transferred to the colliding particle in the form of excitation into a higher energy state. Both processes are shown as:

$$X^* + X^{'} \leftrightarrow X + X^{'*} \tag{1.7}$$

The radiative bound-bound processes are identical to the collisional ones, except that the energy source for the excitation is a photon. These radiative processes can be shown as:

$$X + hv \leftrightarrow X^* \tag{1.8}$$

In the inverse process, a photon is emitted when the atom/ion drops to a lower energy bound state. It is extremely important to the application of plasma spectroscopy since this process yields the characteristic line spectra used for spectrochemical analysis.

1.3 General characteristics of plasmas

A plasma is a group of charged particles, which consists of free positive and negative charge carriers (Griem and Lovberg, 1970 [5]). In a partially or fully charged plasma, the total number of positively charged and negatively charged particles are balanced so that the plasma stays in a neutral state. The relationship between the number density of electrons n_e and charged ions n_z is described as:

$$n_e = \sum_z n_z z \tag{1.9}$$

where z is the charged state of an ion. From this description, it is the charged particles that distinguish plasmas from ordinary gases. The plasma characteristics are determined by the charged particles and the interactions between them.

1.3.1 Debye sheath and plasma frequency

The electrons in the plasma produce electric fields which can be described by *Coulomb's Law*. The Coulomb forces between charged particles in this Coulomb field are strong and long-ranged compare to an ordinary gas. Hence, if an electron or ion is displaced from its equilibrium position it can affect or disturb its neighboring electrons or ions. It in turn can react to these disturbed charged particles. When electrons are displaced from the equilibrium position in a plasma they oscillate together or "collectively" thereby creating an electron wave motion. The same ap-

plies to ions when displaced from equilibrium, they too move collectively and give rise to ion waves. Since the ions are much more massive than the electrons, their natural frequency of oscillation is much lower than that of the electrons. In low density plasmas, this can be at acoustic frequencies and hence sometimes they are referred to as ion-acoustic waves. In a laser produced plasma as described in the previous section 1.1, with an electron density as high as 10^{21} cm^{-3}, the plasma is dominated by the collective phenomena.

A charged particle in the plasma interacts with its immediate neighbors with a calculable Coulomb force. At greater distances the Coulomb force is weakened and eventually cancelled by other surrounding charged species of opposite sign. The distance that defines the region of the effective Coulomb interaction is known as the Debye Length λ_D which is given by:

$$\lambda_D = \sqrt{\frac{\varepsilon_0 kT}{n_e e^2}} \tag{1.10}$$

where ε_0 is the dielectric constant, k is Boltzmann's constant, T is the plasma temperature, e is electron charge and n_e is the electron number density. In a plasma dominated by collective phenomena, the physical dimension of the plasma, L, must be on a macro scale compared to the Debye length:

$$L >> \lambda_D \tag{1.11}$$

When electrons in such a plasma are displaced collectively from the positive ions [6], the plasma is polarized and the electrons tend to move back to their original equilibrium position [7]. The resulting oscillation of electrons in the plasma is referred to as plasma oscillation, and the frequency of this oscillatory motion is termed the plasma frequency ω_p which is given by:

$$\omega_p = \sqrt{\frac{n_e e^2}{m_e \varepsilon_0}} \tag{1.12}$$

where ε_0 is the electric constant, m_e is the electron mass, n_e is the electron number density and e is electron charge. Frequencies of ion oscillations can be described and computed in the same way by simply replacing the electron mass m_e by the ion mass m_i in equation 1.12.

The plasma frequency determines the response of a plasma to an incoming electromagnetic radiation source such as a laser beam. Consider an incident wave of frequency ω, when it matches the characteristic frequency of the plasma the energy

transfer from the electromagnetic wave to the plasma will be significantly enhanced due to the resonance interaction between them. The dependance of ω on the propagation constant $k = 2\pi/\lambda$ of the incoming electromagnetic wave is given by:

$$\omega^2 = \omega_p^2 + c^2 k^2 \tag{1.13}$$

where ω_p is the plasma frequency and c is the speed of light. As the plasma frequency ω_p varies with the electron density n_e, when $\omega > \omega_p$, k is real and the wave propagates through the plasma; when $\omega < \omega_p$, k is imaginary and the wave does not pass through, i.e., it is reflected or absorbed; when $\omega = \omega_p$, the wave is reflected, the electron density at this moment is then called the critical density n_c. At this point, consider that $\omega = 2\pi f = 2\pi(c/\lambda)$, a radiation source in the UV wavelength range will penetrate a dense plasma to a greater extent than that in the VIS-IR wavelength range. This is why X-ray sources are often used to probe laser produced plasmas.

1.3.2 Thermodynamic equilibrium in a plasma

In an ideal thermodynamic enclosure, the plasma properties such as temperature, density, and composition (when multi-elements are presented) can be fully characterized by a finite number of thermodynamic variables. This complete thermodynamic equilibrium state is described by Carroll and Kennedy [6]. The criteria for a system to be in thermodynamic equilibrium system are: a) all particles including electrons, ions and neutral species obey the Maxwell velocity distribution; b) the population distributions over the states of any atom or ion are described by the Boltzmann formula; c) the relationship between the number of ions in stage z and the number in stage $(z-1)$ is given by the Saha equation; d) the intensity distribution of the radiation in the cavity is given by the Planck formula.

In practice, thermodynamic equilibrium is rarely complete and so an approximation called local thermodynamic equilibrium (LTE) is applied. It only requires that the equilibrium exists in small regions in the plasma, although each local equilibrium state may vary from region to region. When collisions occur in a plasma as described in the previous section 1.3.1, heavy particles (ions and atoms) and light particles (electrons) are more likely to achieve equilibrium separately since energy is likely to be distributed more equally between colliding particles with similar masses. LTE or near-LTE in a laboratory plasma may be achieved after a sufficient number of collisions occur between electrons and ions. Thus LTE is more likely to be achieved at high electron densities since the radiative rate is significantly smaller

than the collisional rate. The electron density required for LTE to hold in a plasma was proposed by McWhirter [8] to be:

$$n_e \geq 1.6 \times 10^{12} T_e^{1/2} \chi^3 cm^{-3} \tag{1.14}$$

where T_e is electron temperature in Kelvin and χ is the excitation energy potential (in eV) of the corresponding transition or emission line under study. Griem [9] provided the example of a hydrogen plasma where his analysis suggested that for a temperature of 1 eV ($\sim$ 11000 K) and atmospheric pressure, an electron density of $10^{17}/cm^3$ would ensure that LTE prevailed. This implies that LTE can be achieved in a LIBS plasma generated by an irradiance of $> 10^8 W/cm^2$ (section 1.1).

1.4 Quantitative spectroscopy in the VUV

High-power pulsed lasers have the ability to produce dense hot plasmas which can generate VUV emission in the wavelength range from 35 nm to 200 nm for spectroscopic analysis. Light emitted from the plasma is dispersed by a diffraction grating, so that photons of different frequencies fall on the photo-sensitive detector (charge coupled device or CCD) as an array of energies of the emitted light. The resulting spectrum distribution is calibrated and plotted as intensity (counts) against wavelength (nm). A spectrum often consists of a number of characteristic spectral lines of a particular atom or ion as stated in section 1.2. These lines indicate the presence of particular species and their intensities are related to the number densities of the corresponding species while the number density of a specific charge state, in turn, depends on the plasma temperature. Although the intensity of an emission line can be related to the number density of the emitting species present in the plasma, the radiation, on passing through the plasma can be scattered, absorbed or otherwise affected, leading to a different measured intensity at the detector. Thus, not only the origin, but also the transport of radiation through the plasma must be accounted for in any analysis of line spectra of laser induced plasmas. The following treatment follows Corney [10] and demonstrates the relationship between spectral line intensities and plasma conditions.

The change of intensity $I_\omega(x)$ of an approximately collimated beam of radiation confined to the solid angle $d\Omega$ as it propagates in the direction 0 - x through a gas of excited atoms is schematically illustrated in figure 1.1.

The radiation is assumed to be unpolarized and its angular frequency ω is chosen to lie close to that of an atomic absorption line, ω_{ki}. The absorption and

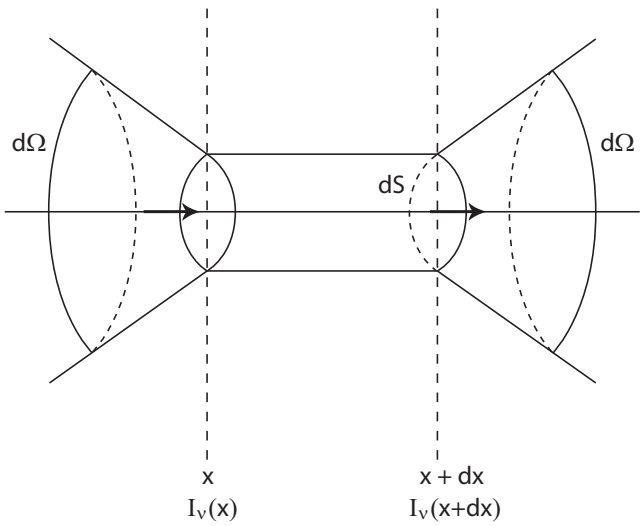

Figure 1.1: The geometric volume-element considered in the derivation of the equation of radiative transfer for a beam of light confined to the solid angle $d\Omega$ ([10]).

emission coefficients of the gas will then be determined by the Einstein A- and B-coefficients associated with the transition k - i (appendix C). The transfer equation is obtained by considering the change in the radiant energy contained within the angular frequency interval $d\omega$ as the beam passes through a cylindrical volume-element of cross-section dS and length dx.

As $dx \to 0$ we have:

$$[I_\omega(x+dx) - I_\omega(x)]dSd\omega d\Omega dt = \frac{dI_\omega}{dx}dxdSd\omega d\Omega dt \tag{1.15}$$

The energy absorbed E_{abs} from the beam as it passes through the volume-element is given by the energy of one photon multiplied by the number of upward transitions occurring in the time interval dt. If there are N_i atoms per unit volume in the lower energy level i we have:

$$E_{abs} = \hbar\omega N_i dxdSB_{ik}^I g(\omega)d\omega\frac{d\Omega}{4\pi}I_\omega(x)dt \tag{1.16}$$

The line shape factor $g(\omega)$ has been introduced to describe the atomic frequency response or lineshape (Appendix C). The term $d\Omega/4\pi$ takes account of the fact that we are considering transitions induced by a collimated beam of radiation confined to the solid angle $d\Omega$. Atoms in the excited level k give energy to the beam by both spontaneous and stimulated emission of radiation into the solid angle $d\Omega$ and frequency interval $d\omega$. The energy emitted E_{emit} in the time interval dt is given as:

$$E_{emit} = \hbar\omega N_k dx dS A_{ki} g(\omega) d\omega \frac{d\Omega}{4\pi} dt + \hbar\omega N_k dx dS B^I_{ki} g(\omega) d\omega \frac{d\Omega}{4\pi} I_\omega(x) dt \qquad (1.17)$$

Taking equation 1.16 and equation 1.17 and substituting them into equation 1.15, the radiation transfer equation becomes:

$$\frac{dI_\omega}{dx} = \frac{\hbar\omega}{4\pi}[A_{ki}N_k + (B^I_{ki}N_k - B^I_{ik}N_i)I_\omega]g(\omega) \qquad (1.18)$$

As $g_i B^I_{ik}$ = $g_k B^I_{ki}$, the equation of radiation transfer can be written more concisely as:

$$\frac{dI_\omega}{dx} = \epsilon_\omega - \kappa_\omega I_\omega \qquad (1.19)$$

where ϵ_ω and κ_ω are the volume emission and absorption coefficients respectively defined by:

$$\epsilon_\omega = \frac{\hbar\omega}{4\pi} A_{ki} N_k g(\omega) \qquad (1.20)$$

and

$$\kappa_\omega = \frac{\hbar\omega}{4\pi} B^I_{ik} N_i \left(1 - \frac{g_i N_k}{g_k N_i}\right) g(\omega) \qquad (1.21)$$

Once the emission and absorption coefficients of the excited gas are specified as functions of frequency and position, the equation of transfer 1.19 may in principle be solved to obtain the intensity. In practice this equation is difficult to solve in all but some of the simplest possible situations.

In the current case, the laser was point-focused by a spherical lens onto a flat surface, the laser-induced plasma can be considered as a uniformly excited source. In this context, we assume that the volume emission and absorption coefficients are independent of x, i.e. the atomic densities N_k and N_i and the line shape factor $g(\omega)$ are constant. In this case the equation of transfer 1.19 may be solved by multiplication by the factor $exp(\kappa_\omega x)$, giving:

$$\frac{d}{dx}[I_\omega exp(\kappa_\omega x)] = \epsilon_\omega exp(\kappa_\omega x) \qquad (1.22)$$

If the excited gas is taken to be in the form of a slab bounded by the planes $x = 0$ and $x = L$, the intensity of radiation at the angular frequency ω that would be observed at the face $x = L$ is given by

$$I_\omega(L) = I_\omega(0) exp(-\kappa_\omega L) + \frac{\epsilon_\omega}{\kappa_\omega}[1 - exp(-\kappa_\omega L)] \qquad (1.23)$$

where $I_\omega(0)$ is the intensity of the beam of radiation incident on the sample at $x = 0$.

The ratio $S_\omega = \epsilon_\omega/\kappa_\omega$ in equation 1.23 is usually referred to the *source function* and the quantity $\tau(L) = \kappa_\omega L$ is known as the *optical thickness* of the source [10]. It determines the amount by which a collimated beam of intensity $I_\omega(0)$ is attenuated as it passes through the medium. When the absorption coefficient is a function of position, a more general expression for the optical thickness is:

$$\tau_\omega(z) = \int_0^z \kappa_\omega(z^{'})dz^{'} \tag{1.24}$$

where $z = L - x$ is measured from the plane $x = L$ into the medium. In this case $\tau_\omega(z)$ would more correctly be termed the *optical depth*. The distance z at which $\tau_\omega(z) \approx 1$ represents the effective depth within the sample from which most of the light of frequency $\omega/2\pi$ is emitted.

Optically thin sources, $\tau_\omega(L) << 1$

To investigate the intensity of radiation emitted by a uniformly excited column of gas of length L, we set the incident intensity $I_\omega(0) = 0$ and equation 1.23 becomes:

$$I_\omega(L) = \frac{\epsilon_\omega}{\kappa_\omega}[1 - exp(-\kappa_\omega L)] \tag{1.25}$$

In an optically thin plasma, the effective optical depth is very small i.e., $\tau_\omega(L) = \kappa_\omega L << 1$. Expanding the exponential factor in equation 1.25 we have:

$$I_\omega(L) \approx \epsilon_\omega L = \frac{\hbar\omega}{4\pi} A_{ki} N_k g(\omega) L \tag{1.26}$$

In this case the intensity is proportional to the density of excited atoms N_k, to the spontaneous emission transition probability A_{ki}, and to the length of the excited gas L. The spectral distribution of the emitted radiation is identical to the intrinsic line profile $g(\omega)$. The measurement of the intensities of spectral lines emitted by optically thin sources is the basis of two widely used techniques: the spectrochemical analysis of metals and other materials and the determination of oscillator strengths of atomic and molecular transitions.

Optically thick sources, $\tau_\omega(L) >> 1$

In the case of spectral lines which terminate on the ground, metastable, or resonance levels of an atom the assumption that $\tau_\omega(L) << 1$ is no longer valid. Sub-

stantial populations accumulate in these levels in a gas discharge and consequently the emitted radiation has a large probability of being re-absorbed before it leaves the source. When the optical depth is of the order of, or greater than unity, the ϵ_ω and κ_ω in equation 1.25 can be substituted by expressions 1.20 and 1.21. Finally the emitted intensity is given by

$$I_\omega(L) = \frac{\hbar\omega^3}{4\pi^3c^2}\frac{1 - exp(-\kappa_\omega L)}{(N_i g_k/N_k g_i) - 1} \tag{1.27}$$

As the number density of atoms or the length of the plasma is increased, there is initially a proportional increase in the emitted intensity $I_\omega(L)$. However when the optical depth $\kappa_\omega L$ is of the order of unity, self absorption becomes appreciable and the intensity increases more slowly. Simultaneously the profile of the emitted radiation becomes broader and then starts to flatten off. Thus self absorption tends to level out intensity differences between spectral lines. Self absorption may also distort the intensity distributions predicted in fine or hyperfine structure multiplets. Eventually when $\kappa_\omega L >> 1$, self absorption leads to an equilibrium between the radiation and the collision processes responsible for the excitation of atoms in the plasma. If the populations of the levels i and k are maintained in thermal equilibrium at the electron temperature T_e then the limiting intensity, obtained by using $\kappa_\omega L >> 1$ in equation 1.27, is given by the black-body distribution. Thus the measurement of the absolute intensity of an optically-thick line would enable the effective temperature of the system to be determined [10].

1.5 Analytical figures of merit

One of the most important figures in analytical spectroscopy is the limit of detection (LOD). It is defined as being "the smallest measure that can be detected with reasonable certainty for a given analytical procedure" by the International Union of Pure and Applied Chemistry (IUPAC). LOD depends on the statistical distribution of data points in a spectrum using the Gaussian distribution which is given as:

$$P(x;\mu,\sigma) = \frac{1}{\sigma\sqrt{2\pi}}e^{-(x-\mu)^2/2\sigma^2} \tag{1.28}$$

It is a function describing the statistics of an event or data occurring within an interval defined by the standard deviation (σ) and the mean value (μ) of the data. In terms of quantitative spectroscopic analysis, the general expression for a gaussian

distribution is integrated and the integral is normalized to unity:

$$\int_{-\infty}^{+\infty} P(x, \mu, \sigma)dx = 1 \tag{1.29}$$

When the limits of the integral are changed to values of σ, it give the probability of a data point lying within the integrated area. And so the probability of a data point lying outside the integrated area is 1 - $P(-\sigma \leq x \leq \sigma)$. If the standard deviation and mean are calculated from the background signal in a spectrum, the probability that a data point lies outside the normal distribution can be estimated, within a stated confidence limit. The confidence limit set by IUPAC for a particular analyte in a matrix is 3σ, giving a confidence level of 99.87% that a point is not part of the background. That means the lowest quantity of a substance that can be distinguished from the absence of that substance (a blank value) within a confidence level of 99.87% is:

$$x_L = \mu + 3\sigma \tag{1.30}$$

For a typical calibration curve, the intensity or line ratio is plotted versus the concentration of analyte. The limit of detection can then be calculated as:

$$L.O.D. = \frac{3\sigma_B}{S} \tag{1.31}$$

σ_B is the standard deviation of the background component of the spectrum with the lowest concentration of analyte. S is the slope of the calibration curve. This is justified by the assumption that, in a calibration curve with slope S , any x value (elemental concentration) can be obtained by dividing the intensity by the slope at a certain point $y/(\frac{y}{x}) = x$. When the value of $3\sigma_B$ is substituted for the intensity of the analytical line, the limit of detection is calculated.

1.6 Summary

Plasma formation and evolution processes were introduced with an emphasis on the post-breakdown phenomena on solid targets. Three atomic processes in the plasma and the general characteristics of a plasma were introduced. The bound-bound transitions provide the characteristic emission lines that are essential to laser induced plasma or LIP diagnostic and analysis. The basic principles of VUV emissions and the analytical figures of merits of LIBS analysis were described at the end of the chapter.

Chapter 2

Introduction to Laser Induced Breakdown Spectroscopy

The introduction to laser induced breakdown spectroscopy (LIBS) includes an overview of the LIBS technique, a brief literature survey of the development of LIBS, and the aim of the current work in a wider scientific context with an emphasis on direct detection of light elements in steel.

2.1 An overview of LIBS

Laser-induced breakdown spectroscopy (LIBS) is an atomic emission spectroscopy technique which utilizes a highly energetic laser pulse as the excitation source. LIBS can be used to analyze any matter regardless of its physical state: solid, liquid or gas. Even aerosols, gels, and other aggregates can be readily investigated by using LIBS. LIBS can detect almost all elements since all elements emit light when excited to sufficiently high energies, limited only by the power of the laser as well as the sensitivity of the dispersed radiation detector and wavelength range of the spectrometer.

The description of the LIBS technique can be divided into three parts: LIBS fundamentals, instrumentation and applications. The following three subsections discuss each category respectively.

2.1.1 LIBS fundamentals

Laser-Induced Breakdown Spectroscopy (LIBS) also called Laser-Induced *Plasma* Spectroscopy (LIPS) uses a pulsed laser to generate a plasma composed of a small amount of a sample. Spectra emitted by the excited species, mostly atoms and lowly charged ions, are used to develop both qualitative and quantitative analytical information.

LIBS operates by focusing the laser beam onto a small area at the surface of the sample to be analyzed. When the laser pulse is fired onto the target it ablates a very small amount of material which rapidly absorbs laser energy to form a plasma plume with temperatures typically ranging from a few 1,000 to 1,000,000 K. For LIBS plasmas, the temperature is often in the range of 10,000-20,000 K. At these temperatures, the ablated material dissociates (breaks down) into excited ionic and atomic species. During this time, the plasma emits a continuum spectrum which does not contain any spectral lines and so does not provide any useful information about the individual atomic and/or molecular species present. However, within a very small timeframe the plasma will have expanded at supersonic velocities and cooled down. This entire process includes the generation and properties of the energetic laser pulse, the formation and features of the plasma and the evolution of the laser induced plasma (LIP).

2.1.2 Brief outline of LIBS instrumentation

In LIBS, a high powered pulsed laser is used to generate a laser-induced plasma (LIP) on the solid sample surface in vacuum or in a gaseous environment where the pressure can typically vary from 1 to 1000 mbar (atmospheric pressure). Winefordner et al [11] reviewed the advantages and convenience of LIBS in elemental analysis compared to several other atomic spectrometric methods. A number of figures of merit, including detection power, selectivity, multi-element capability, cost, application areas etc. have been considered. Song et al [12] provided a description of the most recent development of LIBS instrumentation. Excimer, CO_2, and Nd: YAG laser systems and their performances for LIBS measurement were included in the discussion. The authors also described several new approaches including dual pulse UV-Vis LIBS, multi-fiber, resonant ablation, and combination with laser induced fluorescence (LIF) techniques. The echelle spectrometer was also considered with the combination of various charge coupled devices or CCDs.

In the work presented here the instrumentation for LIBS generally consists of a pulsed laser beam for sample ablation or breakdown, the optics for focusing the laser beam and collecting the plasma emission, an ablation chamber, and a spectrometer system for detection and the determination of specific elements in the plasma. In the vacuum ultraviolet (VUV) region of the spectrum, the configuration is a little more complex due to the nature of the radiation under investigation. Since air is a VUV absorber, experiments must be performed in either partial or good vacuum conditions. This means that the target, spectrometer and detector must be held under vacuum conditions. However, ambient gases are sometimes used to buffer laser plasma expansion, thus local pressure in the ablation chamber must be generated separately from the spectrometer (which remains in vacuum throughout the entire experiments). Details of the setup for the LIP VUV emission measurements will be provided in the experimental chapter (Chapter 3).

2.1.3 LIBS Applications

Since the invention of the laser in the 1960s, diverse new spectroscopic techniques utilizing the laser have been developed. The main characteristics of lasers compared to conventional light sources are directionality, coherence, high power, pulsed beam and monochromaticity. Because of these unique characteristics of lasers, many new fields of applications in modern spectroscopy have evolved and lasers are considered an essential tool in modern spectroscopic techniques.

A large number of publications provide good reviews on LIBS applications.

These reviews include books [1, 13, 14] on general LIBS and articles on analytical chemistry trends [15], LIBS fundamentals [16, 17], LIBS applications in elemental analysis [18, 19, 20], LIBS for products analysis and applications in the steel industry [21, 22, 23, 24] and other applications in a more general analytical spectroscopy fields [25, 26, 27].

Among these applications, LIBS is particularly attractive for the analysis of alloys because the technique can be employed directly on a solid sample without the necessity for sample pre-treatment, saving time and operating costs. Due to its wide industrial applications, the alloy of greatest interest is steel. Element detection is one of the main applications of LIBS in steel studies.

Steel is an alloy consisting mostly of iron, with a carbon content between 0.1-1.7%. Carbon is the most cost-effective alloying material for iron. For example, the carbon content in alloys that are used to manufacture car bodies and central heating radiators must not exceed 0.3%, which are known as low carbon steels. Bridges and ships use alloys that contain a medium concentration of carbon between 0.3% and 0.7%. In addition, high carbon steels are those that have carbon in the range from 0.7% up to about 1.3% and are used to make various cutting tools because of their hardness. Other elements such as Al, Co, Cr, Cu, Mn, Mo, Ni, Si, Sn, Ti and V, act as a hardening agent, preventing dislocations in the iron atom crystal lattice. All of these elements can have a significant influence on the structure and physical properties of carbon-steel alloys [28]. High precision of the chemical composition of steel is desired for numerous tasks associated with process control in the steel industry. The limit of detection (LOD) calibration results for various elements in steel have been improved to the part per million (ppm) range. Great efforts have also been made to enhance the LIBS technique system for better LOD result. Here are some examples of elemental studies of steel using enhanced LIBS.

Sturm and Vrenegor et al. [23, 24] investigated the use of the multi-pulse excitation LIBS with steel alloys. In 2000, they focused on the analyses of light elements including C, P, S, Mn, Ni, Cr and Si, in the vacuum ultraviolet spectral region [23]. Analytical curves with good correlations and detection limits in the range of 7 to 11 μg/g were obtained. After that they compared the triple-pulse configuration with single-pulse and double-pulse in 2004 [24]. C, P, S, Al, Cr, Cu, Mn, and Mo were quantified. An increase in detectability was observed due to an enhancement of material ablation. Good detection limits around 7 to 10 μg/g for Al, C, Cu, Mn, Mo and detection limits two or three times greater for Cr, Ni, P and S were achieved. In the following year, they quantified the content of Ni, Cr, Cu, Mo, Si, Ti, Mn, Al and C in high alloy steel [29]. Investigations were made with single and double-pulse

configurations with the same total energy and two different laser burst energies. One particularly interesting conclusion was that the single-pulse mode was better for Cr, Ni, Cu, Mo and the double-pulse mode was better for Si, Ti, Mn and C. The use of inter-elemental corrections which improved the detection limits up to two or three fold was also discussed.

Khater et al [30, 31] quantified carbon in steel alloys in the vacuum ultraviolet spectral region. The analytical capability of laser-produced plasmas in combination with time-integrated, spatially-resolved (TISR) emission spectroscopy in the vacuum ultraviolet (VUV) was investigated. For the first time, a study of the selection of the most appropriate spectral lines for carbon analyses in standard reference steels was presented. In Khater's work, four spectral lines (C^{2+} 45.96 nm, C^{+} 68.73 nm, C^{2+} 97.70 nm, C^{2+} 117.57 nm) were identified to present the best performance and the 97.70 nm C^{2+} line allowed for the lowest detection limit and the best linear analytical curve. With an optimization of experimental setup parameters, the detection limit of carbon in steel was improved to (1.2 ± 0.2 μg/g) for the 97.70 nm spectral line.

O'Leary [4] achieved low-level quantitative determination of sulphur in steels in both vacuum and gaseous atmosphere studies. Two approaches to the calibration curves were used: the internally referenced method and the unreferenced method. The internally referenced calibration curve resulted in a limit of detection of 1.8 ppm (part per million), while the unreferenced curve resulted in 1.7 ppm. Both of these limits are far better than those produced in vacuum and almost three times better than the best available LIBS limit of detection published in the literature to date.

2.2 Literature survey of LIBS

In addition to the introduction of LIBS fundamentals, the instrumentation and applications by example, a literature survey is provided, reviewing the development of LIBS and to look at the future of LIBS.

2.2.1 A brief history of LIBS

With the invention of the Ruby laser in 1960, a laser-induced plasma was observed. The laser was used primarily as an ablation source in the early stages of the laser technique development. In 1963, Debras-Guedon and Liodec published its first analytical use for spectrochemical analysis of surfaces [32], marking the birth of

laser-induced breakdown spectroscopy (LIBS). LIBS experiments were carried out on solid surfaces, in gases and in liquids. The requirements for studies to be carried out on different materials using LIBS resulted in the development of instruments specifically targeted on LIBS.

The early instrumental development included laser ablation and cross-excitation with a conventional spark (e.g. by electrode). The spark could contaminate and complicate the analysis through the introduction of electrode material and so cross-excitation by electrode-less methods were also developed (e.g. inductively coupled plasma, ICP). Although these instruments could handle nonconducting samples, they could not typically compete in accuracy and precision with conventional spark spectroscopy. A discussion of those devices and the associated techniques can be found in Moenke-Blankenburg's book [33], *Laser Micro Analysis*.

In the beginning of the 1970s, with more sophisticated LIBS instruments becoming available, time-resolved spectroscopic analysis of laser-induced plasmas was developed to monitor the plasma evolution and help discriminate the continuum background from the line spectrum. Different detection systems were also employed to obtain temporally resolved spectra. As detectors have developed, the preferred methods for time-resolved LIBS measurement have moved to gated, intensified charge coupled detectors (CCD). These early innovative studies on the spectral imaging and recording systems include Schroeder et al. [34, 35], Menzies et al. [36], Koppel et al. [37], Brunol et al. [38].

Time-resolved laser plasma studies extended into the 1980s and the research field widened as the in-situ advantages of the laser plasma became more obvious when lasers and other LIBS components became more compact and user friendly. During this period, laser induced plasma analysis covered spatial/temporal plasma evolution [39, 40, 41], physical and chemical matrix effects on elemental analysis [42], plasmas in water [43, 44], LIBS on aerosols [45, 46] and other functional materials (e.g. [47]). Progress in both apparatus and understanding of laser plasma fundamentals and techniques have made LIBS more capable of challenges such as detection of toxic dust in air and on filters [48, 49], hazardous gases [50], aerosols [46] and liquids [51].

Other studies focused on plasma diagnostics and enhancements from the late 1980s to the early 1990s. Characterization of laser induced plasmas and determination of plasma parameters such as electron temperature and density were carried out by various groups (e.g. Essien and Radziemski in 1988 [52], Grant et al. in 1990 [53], Sabsabi in 1995 [54]). Attempts were also made to enhance the plasma emission by a magnetic field [55] or an electric field [56].

From the 1990s to 2000, applications and fundamental studies developed rapidly. The improvements on LIBS quantitative analysis continued. Quantitative LIBS have been improved for aerosol analysis [57], artworks [25], ores [58] and also remote-LIBS [59]. Remote-LIBS, which began in the 1980s, has been developed rapidly since the 1990s and includes topics such as remote elemental analysis [60] and the fiber optic probe in remote applications [61, 62]. LIBS for the analysis of lunar surfaces was first mentioned by Blacic et al. [63] and Kane et al. [64]. A series of works by Knight et al. [65] and Wiens et al. [66] provided further contributions to planetary exploration and analysis with the aid of LIBS.

2.2.2 LIBS in recent years

Since the first international meeting on LIBS held in 2000 in Pisa, Italy to the most recent Euro-Mediterranean Symposium of LIBS, LIBS has gradually developed into a powerful and versatile analytical technique. Its maturity has also been marked by its adoption in planetary geology on the 2009 mission to Mars.

New areas of study include increasing exploration of the vacuum ultraviolet region of the spectrum, biological applications on human teeth, bones and tissue, surface mapping and imaging (scanning LIBS), instrumentation for commercial and marketing purpose and sophisticated statistical techniques to enhance the efficiency and reliability of LIBS analysis.

Here is a brief summary of the topics presented at the International LIBS conferences held in recent years. These topics represent the current status of LIBS development. Topics included at LIBS-2008 and the numbers of the talks belonged to each topic are listed in table 2.1. The conference proceedings and the short courses topics can be found at `http://www.libs2008.de/`. Among the wide range of

Topics	number of talks
Fundamentals	14
Modeling and Calibration	5
Industrial applications	6
Romote and Environmental	11
Particles and Plasmas	4
Culture and heritage	3
Instrumentation	4

Table 2.1: List of topics discussed at LIBS-2008 conference

LIBS studies, about 1/3 of the talks were dedicated to the fundamental and theoretical (including modeling and calibration) studies. There was a particular focus on

double pulse (DP) techniques which included DP-LIBS with femto-second lasers (Pinon, Spain), high resolution LIBS of sapphire using femto second double pulses (Baumert, Germany), emission enhancement by a simultaneous CO_2 laser pulse with the combination of ablative Nd:YAG laser (Waterbury, FL, USA), a fundamental study of the effect of DP-LIPS (Giacomo, Italy) and comparison study of laser ablation (LA) with double- and single-pulse excitation (Cristoferetti, Italy). Other techniques also aiming for the enhancement of breakdown based spectroscopy included filament-induced breakdown on organic thin films (Baudelet, MD, USA), microwave enhancement for spark-induced breakdown (Kaneko, Japan) and laser-assisted microwave enhancement of LIBS (Efthimion, NJ, USA). Besides the modeling studies aimed at providing a deeper understanding of the plasma evolution process, topics concerning multiple emission line (Mungas, USA) or multi-element analysis (Death, Australia) were discussed and found to be appealing for some LIBS applications. The multivariate approach turned out to be a useful tool for LIBS analysis and this topic attracted numerous research groups in a short time.

The topics presented at the LIBS-2010 are categorized as in table 2.2. The conference proceedings and short courses are available at `http://www.icet.msstate.edu/libs2010/`. The multivariate analysis was remarked as a great contribution

Topics	number of talks
Fundamentals	5
Analysis	7
Industrial	6
Applications	8
Aerosol and Environment	4
Instrumentation/Commercialisation	4
Biomedical	3
Hyphenated Techniques	4

Table 2.2: List of topics at LIBS-2010 conference

to the traditional LIBS analysis as it provides the ability to perform simultaneous observation and analysis of more than one statistical variable. Multivariate techniques, often refereed to in this context as chemometrics, have been applied to multi-element analysis, analytes in complex matrices, or residue mixtures on multiple substrates. The combination of LIBS and chemometrics has widened the analysis ability of LIBS. LIBS analysis has extended to encompass samples like mineral ores, seawater, aerosols or solid samples covered by water droplets, biological and organic samples, and other geochemical analysis.

As a further enhancement to LIBS, efforts have been made to modernize some

of the traditional spectroscopy based methods by combining LIBS with Raman spectroscopy or spark-induced breakdown spectroscopy (SIBS), laser-induced fluorescence (LIP), laser ablation-inductively coupled plasma-mass spectroscopy (LA-ICP-MS) and resonance-enhancement. As presented at LIBS-2010, there was an increasing emphasis on commercialization and novel applications such as portable LIBS. These applications are particularly popular in security and forensics.

From the above literature survey, one can conclude that LIBS has now been developed into a unique and versatile analytical method. On the one hand, expanding the analytical capability of LIBS has never stopped, either by enhancing the LIBS analysis procedure or by combining LIBS with other new or developed techniques. On the other hand, many of the earlier studied topics in LIBS history have re-surfaced because of increased needs or improved instrumental capabilities. These are the two main trends of the LIBS development and leads one to believe that LIBS will always be a powerful analytical tool in many areas.

2.3 Aims and objectives of the present work

The ultimate goal of the current work is to improve the detection limit of light elements (C and S) in steel using LIBS in the VUV regime. The investigations were carried out using space-resolved spectroscopy which provides the spatial structure of a laser-induced plasma (LIP) as an alternative to the more commonly used time-resolved spectroscopy. A number of standard steel samples with carbon/sulphur concentration varying from 0.001% to 1.32% were used to construct the calibration curves from spectral data. A 1 meter normal incidence VUV spectrometer equipped with a 1200 lines/mm reflective concave grating was used to disperse the emitted plasma radiation while a VUV sensitive CCD camera was employed to detect the emission signal.

To achieve a better limit of detection (LOD), dual-pulse operation was introduced for the first time to the space-resolved LIBS system in the VUV emission regime. Thus two Nd:YAG lasers were employed for the experiments. The Spectron laser of 1064 nm wavelength, 15 ns pulse duration and 200 mJ output served as the ablation laser, while the Surelite laser with 1064 nm wavelength, 6 ns pulse duration and 665 mJ maximum output was used as the re-heating laser in a collinear geometry. A number of important parameters in the dual-pulse LIBS scheme including pulse energy, (de)focusing and inter-pulse delay time were studied in detail.

All experiments were carried out in the vacuum ultraviolet spectral range. How-

ever the efficiency of signal collection was low due to the fast expansion of the plasma in vacuum, especially with high energy dual-pulse excitation. The aim of bringing in ambient gas(es) was to buffer the expanding plasma in the chamber thus increasing the overall signal level. The effects of gas pressure and gas type were investigated in detail, considering especially the absorption of VUV light caused by gases as a function of pressure. Dual-pulse parameters including re-heating pulse focusing and inter-pulse separation were also re-examined in pressure controlled ambient gases.

Applying the combination of dual-pulse irradiation in an ambient gas to the LIBS VUV emission system is unique in the current literature and the overarching aim of this work is to explore it parametrically and attempt to optimize it.

2.4 Summary

This chapter provided a comprehensive introduction to LIBS including the fundamentals, instrumentals, applications and an overview of LIBS in the literature of laser-induced plasmas analysis. LIBS development in recent years was also described based on a brief survey of LIBS conferences in the recent few years. The brief but up-to-date literature survey of LIBS was followed by the aims and objectives of the present work, given in the last sections 2.3.

Chapter 3

Equipmental System

This chapter provides a description of the component parts of the DCU LIBS system including lasers, targets, spectrometer, and detection system.

The basic LIBS experimental setup is shown schematically in figure 3.1. The essential parts of a typical LIBS system include the laser system, chamber, targets, laser focusing optics, spectrometer and signal detecting system.

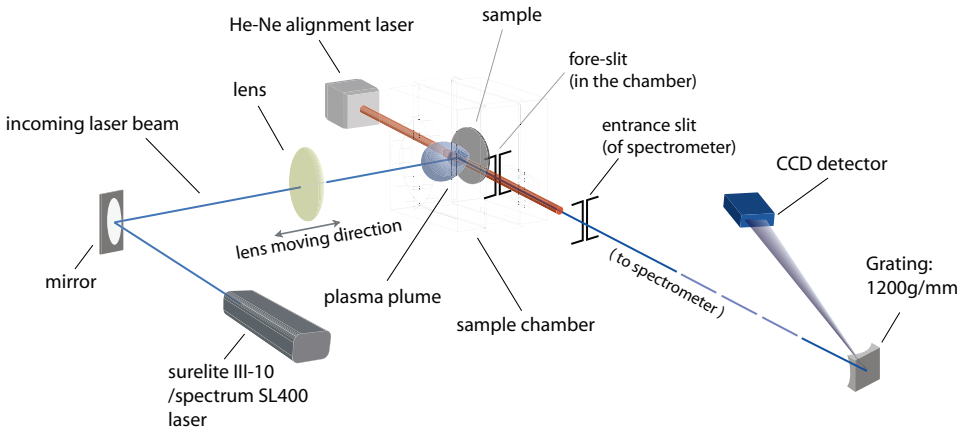

Figure 3.1: Basic LIBS experimental layout.

In the vacuum ultraviolet (VUV) region of the electromagnetic spectrum, the experimental configuration was a little more complex than a typical LIBS setup due to the nature of the radiation under investigation. Since air is a VUV absorber, the target, spectrometer and detector must be held under vacuum conditions. As gases were sometimes used to buffer laser plasma expansion, partial pressures must be generated in the target chamber and separated from the spectrometer using differential pumping techniques. As can be seen in figure 3.1, the system consisted of the key components for radiation generation, dispersion and detection, i.e., the laser pulse, target chamber, spectrometer, grating and CCD camera respectively. Two lasers were employed in this experiment, one was a Continuum Surelite model III-10, capable of producing an optical pulse carrying an energy of up to 820 mJ at a wavelength of 1064 nm (the Nd:YAG fundamental wavelength) in 6 ns. The other laser was a Spectron SL404 laser with a maximum energy of 400mJ at 1064 nm delivered in a pulse of 15 ns duration. The target chamber was a simple aluminum cube (with sides of length 12.5 cm) which had been hollowed out. Two slits were employed to enable space-resolved spectroscopy: a fore-slit (250 μm width) mounted in the target chamber combined with an entrance slit (10 - 40 μm width) placed at the entrance of the spectrometer. The spectrometer was a 1m normal incidence Acton Research Corporation model VM-521 equipped with a 1200 grooves/mm Bausch and Lomb Al+MgF2 coated holographically-ruled diffraction grating. The radiation detection system was a back-illuminated, VUV-sensitive An-

dor Technology CCD camera. In what follows the individual system components are described.

3.1 The laser system

The main laser used in our experiments was a Continuum Surelite model III-10, capable of producing a pulse with a maximum output energy of 820 mJ at a wavelength of 1064 nm (The Nd:YAG fundamental wavelength) with a pulse width of 6 ns. The variation in the output pulse energy from this laser is typically 5%, which is ideal for laser plasma experiments where repeatable results are highly desirable. Figure 3.2 illustrates the optical layout of the Surelite laser.

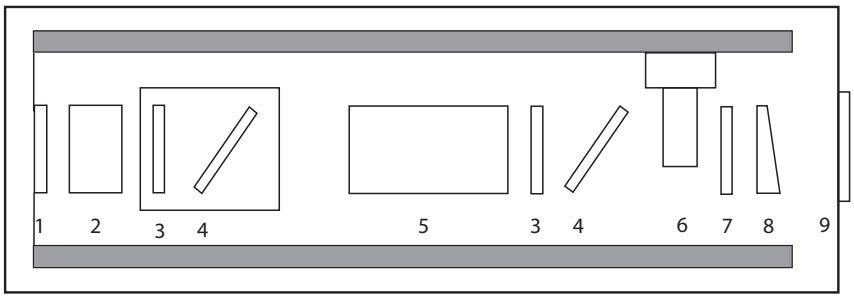

Figure 3.2: Surelite III-10 Laser Optical Layout.

The main components are as follows:

1. Rear mirror, 100% reflectance
2. Pockels cell
3. $\lambda/4$ plate
4. Dielectric polariser
5. Laser head - 2 flashlamps, Nd:YAG rod, cooling system
6. Intra-cavity shutter
7. Gaussian mirror
8. Output beam compensator
9. Exit port

Laser action requires the generation of a "population inversion" where the number of atoms of the lasing host material in an excited state exceed those in some lower state. Stimulated emission, the process underpinning light amplification, can then proceed between these states. In the case of the Continuum and Spectron lasers used here, one or more flashlamps are fired to produce broad band radiation extending from the near UV to IR spectral region. By appropriate choice of flashlamp filling gas and pressure, one can tune the peak wavelength and bandwidth to best match the absorption band in the laser host material. A certain amount of this pumping light energy is absorbed by the lasing material (Nd ions in a YAG crystal matrix, YAG: yttrium aluminum garnet). When the pumping energy is sufficiently high, the population inversion is established among the Nd ions in the laser rod (see No.5 in figure 3.2). When the lasing medium is pumped, it contains atoms with electrons in the upper level of the lasing transition. These excited atoms can decay to the lower energy level of the lasing transition emitting photons at the laser wavelength. When one of these photons encounters another atom that has an electron in the excited upper state of the lasing transition, stimulated emission can occur. The first photon can stimulate or induce atomic emission such that the subsequent emitted photon (from the second atom) produces a quantum of radiation with the same frequency, direction and phase as the incoming photon leading eventually to a monochromatic, collimated and coherent light beams respectively. The incoming and stimulated photons continue their journey through the laser medium and stimulate two more photons. Ignoring loss mechanisms, these 4 can produce 8 in subsequent interactions and so the radiation field grows along the laser medium, doubling at each interaction. In practice the gain is lower as photons are lost through other loss mechanisms such as fluorescence outside the laser emission band, and other parasitic losses. The net effect is Light Amplification via the Stimulated Emission of Radiation or LASER action. The laser rod is typically enclosed in a resonant cavity composed of two mirrors which reflect some of the amplified light back to the laser rod so that more atoms are de-excited and emit more such photons via stimulated emission, when the reflected photons re-pass through the laser rod. Thus significant amplification of light at the wavelength of the lasing transition can be achieved in many passes of the radiation field until so many atoms in the upper lasing level have been depleted that the population inversion is lost, the stimulated emission process is switched off and the Nd ions begin to absorb radiation again.

To obtain a short pulse on the nanosecond timescale, a Q-switched shutter is placed in the cavity to prevent photons from completing the full path of the laser

rod, thus the stimulated emission is interrupted and the population inversion between the upper and lower levels of the lasing transition can become very large. When the Q-switch is activated by a timed gate pulse, the laser cavity transmission is suddenly increased to close to 100% which allows the photons to pass through the laser rod so that the excited atoms are stimulated to decay very rapidly (usually in a couple of passes of the optical cavity corresponding to a few nanoseconds), resulting in a high power laser pulse of short duration on the order of 5 - 10 ns. The Continuum and Spectron lasers are normally internally triggered at a pulse repetition frequency (or PRF) of 10 Hz and pulses were selected by gating the trigger pulses for the Pockels cells. This repetition rate can also be adjusted to lower frequencies down to 1 Hz. They can also be triggered manually for asynchronous operation. For the experiments throughout this work the pulse repetition frequency was fixed at 10 Hz.

3.2 Target chamber and targets

The target chamber used as part of the experimental system is an aluminum block with a hollowed interior. While the block is cubic with sides of 12.5 cm, the interior has been hollowed by simply drilling cylindrical holes through the block along three orthogonal directions. Each hole has been drilled from face to opposite face; the radius of each cylinder is 3.5 cm. This makes for a total internal volume of about 0.75 L. All sides were polished to accommodate standard o-ring sealed flanges, which require rubber o-rings to form a vacuum tight physical seal between outside fittings such as windows and connectors and the chamber itself. A photo of the chamber is shown in Figure 3.3.

In order to optically align the system with the spectrometer and CCD camera, a helium-neon laser was mounted on a 2-dimensional translation stage, and passed straight through the fore-slit and the entrance slit of the spectrometer, onto the centre of the grating and reflected onto the centre of the "exit arm" of the spectrometer with the grating set to the zero order position.

It is also important to align the Glass Capillary Array (GCA) with the optical axis. This is done by placing the GCA in its holder and centering it on the optical axis of the spectrometer. The He-Ne laser was passed through the GCA which was adjusted until the characteristic diffraction pattern was centered on the spectrometer entrance slit at which point its entrance and exit faces are orthogonal to the He-Ne beam ensuring maximum transmission of the VUV radiation. The target surface was aligned with the optical axis of the experiment by moving the target

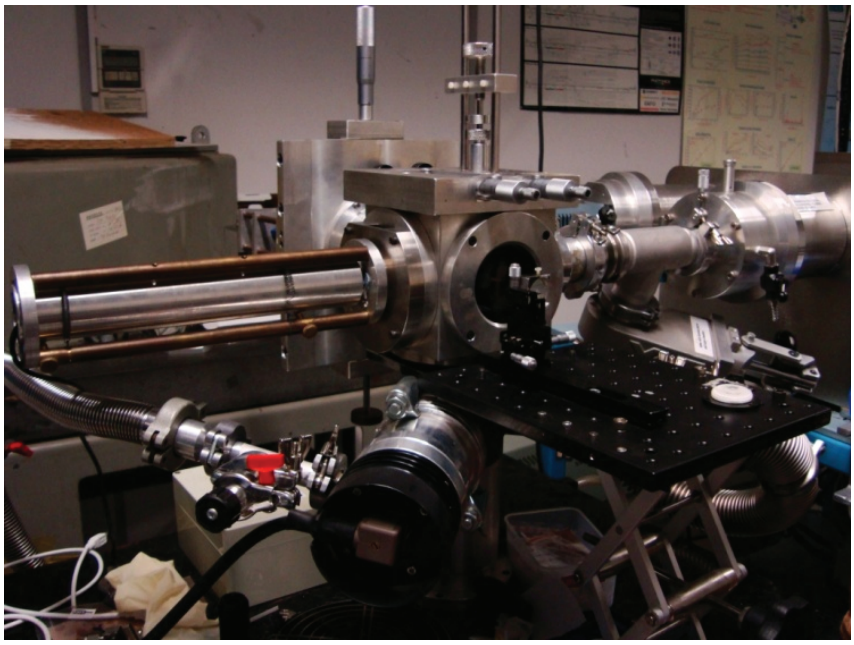

Figure 3.3: Target chamber and associated vacuum and optical components.

until the He-Ne laser beam was blocked by the front edge of the target.

The targets used in this experiment were mounted on an externally controlled XYZ stage, shown in Figure 3.4. The target was screwed onto a post, which was coupled to a micrometer outside the chamber so that it could be moved in the Z-direction (towards/away from the optic axis of the spectrometer). The post itself went through a pair of aluminum plates that were driven by separate micrometers in the orthogonal (X, Y) directions, giving 3 dimensional motion control of the target in the chamber. All moving parts were O-ring sealed so that the target could be moved during experiments with the chamber remaining under vacuum.

A wide range of targets (Carbon/Steel) with varying analyte concentrations were purchased from Glen Spectra Reference Materials^{TM}. For initial studies, a single sample with a high concentration of the analyte was chosen and placed in the target chamber. When optimum conditions were extracted from these studies, samples with varying concentrations of analyte were machined and placed into a carousel which had space for up to 6 targets as shown in Figure 3.5.

In this way, multiple samples could be studied while maintaining an identical vacuum environment and ensuring that each target was automatically aligned with the optic axis. One of the advantages of LIBS is that targets require very little preparation before study. Target surface cleaning was achieved in vacuum conditions in

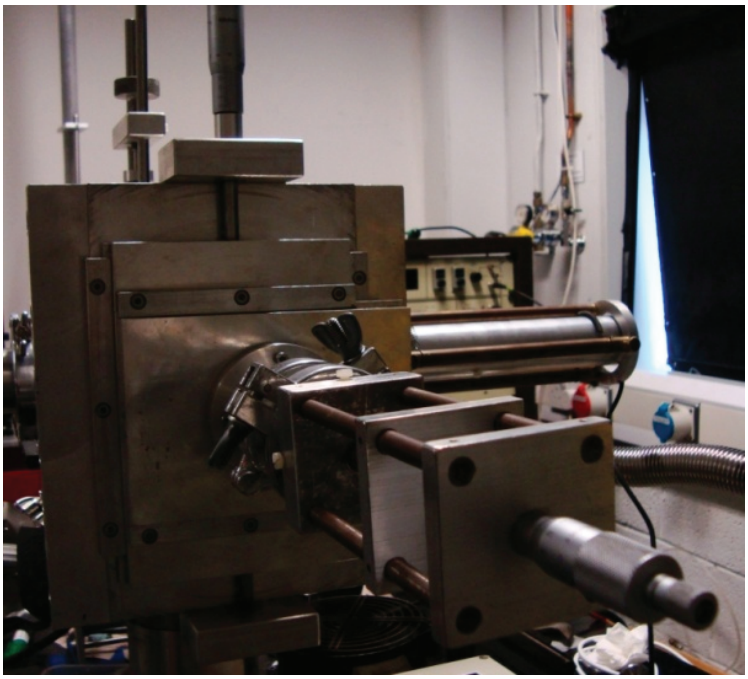

Figure 3.4: Target XYZ Manipulater (at the backside of the target chamber).

Figure 3.5: Target carousel loaded with six steel targets with varying carbon concentrations.

the chamber by firing unfocused laser shots onto the target surface to remove any surface contaminants like dirt or rust which were sometimes present. In addition to these precautions, the target surface was rotated periodically in order to expose a fresh surface after every train of shots; this reduced the possible effects of cratering e.g., plasma confinement and/or occlusion by the target surface.

The targets (12 steel samples) with various light element concentrations employed in the study are listed in table 3.1.

		Concentration (w/w%)		
No.	Sample	C	S	Fe
1	361-50E	0.001	0.0119	99.83
2	084-CRMFE1	0.005	0.0027	99.75
3	361-XAAS	0.041	0.009	99.41
4	361-XCCV	0.44	0.024	97.35
5	361-2932	0.208	0.02	98.14
6	361-54D	0.668	0.046	97.09
7	351-215/3	0.91	0.031	98.00
8	371-229/1	1.32	0.021	97.71
9	15704a-1	0.34		99.35
10	15704a-2	0.013		99.81
11	15704a-3	0.018		99.62
12	15704a-4	0.087		99.17

Table 3.1: The steel samples used in the work reported in this thesis. The concentration is given in weight/weight percent (W/W%) which is normally defined as 100 $\times$ the ratio of the solute weight to the solution weight. Here the solute is the carbon (analyte) content (in grams) and the solution is the Fe (matrix) weight (also in grams).

3.3 GCA and the spectrometer

As previously described, positioned in between the target chamber and the spectrometer, there is another important part of the LIBS-VUV spectroscopy system, a so-called Glass Capillary Array (GCA). A GCA is a vacuum optical component that allows pressure differences to exist between two separate parts of a vacuum system while leaving the aperture between these two areas mostly transparent to light. A GCA is basically a glass plate with very fine holes bored in it - these are capable of maintaining up to 3 orders of magnitude pressure difference between its entrance and exit faces, depending on the individual capillary diameters and the thickness of the array itself. They are in effect bare micro-channel plates without the usual

dynode coating material on the channel walls or any cathode or phosphor coatings on the entrance/exit faces. A microscope image of a GCA is shown in Figure 3.6 below, taken from the Burle Industries Inc. website. The GCA shown has a pore diameter of 5 μm.

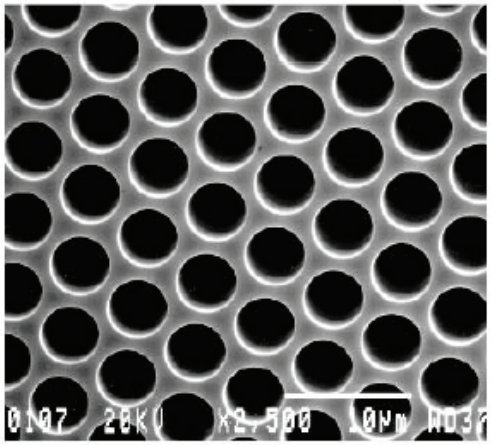

Figure 3.6: Microscope image of a typical GCA (from Burle Industries Inc.).

The GCAs provided by Collimated Holes Inc. and used in the current experiments were 25mm in diameter, 3mm thick and had a pore diameter of 50 μm. They were made from lead-alkali silicate.

The spectrometer used was a 1 m normal incidence Acton Research Corporation^{TM} model VM-521 equipped with a 1200 grooves/mm Bausch and Lomb^{TM} Al+MgF2 coated holographically-ruled diffraction grating. The stated spectral range of the spectrometer extends from 30 to 325 nm but in practice this is limited by the efficiency of the grating at longer wavelengths to the 30 to 160 nm range. Gratings blazed for longer wavelengths are available. The lower wavelength limit is considered to be the transition wavelength between VUV and EUV radiation bands where normal incidence optics tends to fail and reflectivity can be restored only by setting optics at grazing incidence to the radiation. Hence, below 30 nm or so, grazing incidence reflecting optics must be used due to the poor reflectivity of normal and near normal incidence single layer metal coatings at EUV wavelengths.

The Al/MgF_2 coating on the grating ensures enhanced reflection efficiency at VUV wavelengths. The spectrometer uses an off-Rowland circle mount for the diffraction grating. This means that, if an image is in focus on the entrance slit of the spectrometer, it will be in focus on the exit slit so long as the exit slit is on the Rowland circle.

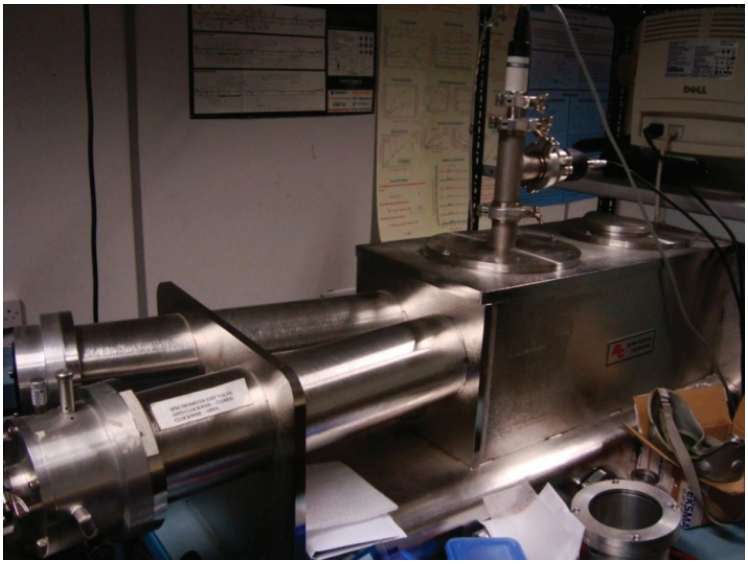

Figure 3.7: ARC VM-521 Spectrometer.

3.4 The Rowland circle and off-Rowland mount

The Rowland circle, as shown in Figure 3.8, is a spectrometer/grating combination that employs a concave grating with radius of curvature R with entrance and exit slits located on a circle of radius R/2. This combines in simple terms the dispersion properties of a plane diffraction grating, with the focusing power of a concave mirror.

The grating is located in the spectrometer vacuum chamber so that both the entrance slit and CCD camera face lie on the Rowland circle when the grating is at the zero order position where both the incident and reflected radiation lie at an angle of 7.5^o to the grating normal. In other words, a point source on the entrance slit is focused to a point image at the exit slit of the spectrometer. It should also be noted that the geometrical location of both the vertical focus (which lies on a tangent to the Rowland circle perpendicular to the grating normal) and the horizontal focus (which lies on the Rowland circle itself) begin to coincide for small angles of incidence and diffraction. So normal incidence VUV spectrometers suffer less astigmatism than do grazing incidence systems that employ concave gratings. Using corrective (usually toroidal) optics, astigmatism can be significantly reduced for EUV spectrometers, at least over selected wavelength ranges.

Diffraction by the spherical concave grating of the constituent wavelengths of light emerging from the entrance slit is described by the same formula that is used

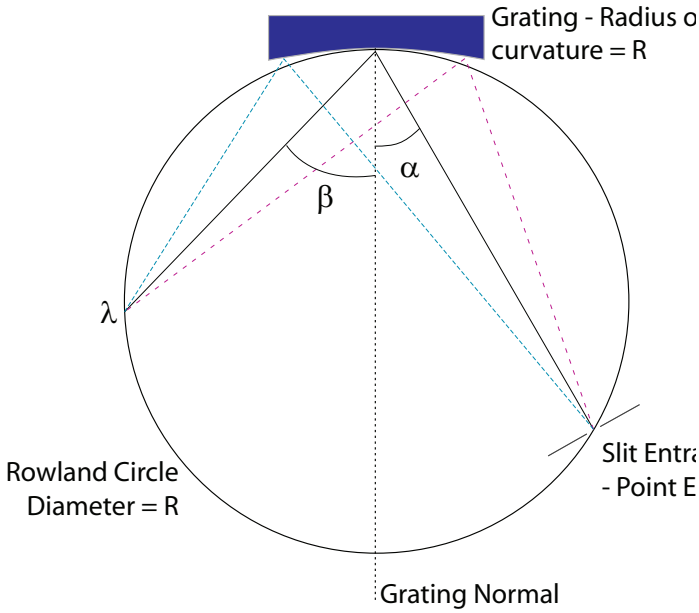

Figure 3.8: Rowland Circle.

for a plane diffraction grating which is given by:

$$\pm m\lambda = d(sin\alpha + sin\beta) \tag{3.1}$$

where m (= 1, 2, 3, ...) is the spectral order, λ is the wavelength, and d is the inter-groove spacing (d = 8.33 $\times$ 10^{-4} mm for the 1200 grooves/mm grating used). The positive sign gives the inside spectrum positioned along the Rowland circle between the central image and the entrance slit. The negative sign describes the outside spectrum that lies along the Rowland circle between the zero order position or the central image and the tangent to the grating. As for the configuration of the spectrometer used in our experiments, only the inside spectrum is recorded so equation 3.2 becomes:

$$m\lambda = d(sin\alpha - sin\beta) \tag{3.2}$$

since α and β lie on opposite sides of the grating normal, they have opposite signs The spectral region from 35 nm to 70 nm is predominantly first order light due to the lower efficiency of the grating for short wavelengths below 35 nm. Higher spectral orders of wavelength λ/m that satisfy equation 3.2, overlap first order spectral light.

Light with different wavelengths is diffracted into different angles. The wavelength distribution across the Rowland circle is called the angular dispersion of

the grating. It is the ability to disperse radiation of different wavelengths per unit angle, $\partial\beta/\partial\lambda$, which is expressed as:

$$\frac{\partial\beta}{\partial\lambda} = \frac{m}{dcos\beta} \tag{3.3}$$

A more practical property of the grating is the *Reciprocal Linear Dispersion*, $d\lambda/dl$, which gives the degree to which radiation is dispersed along the Rowland circle. It is expressed as:

$$\frac{\Delta\lambda}{\Delta l} = \frac{\Delta\lambda}{\Delta\beta} \times \frac{\Delta\beta}{\Delta l} \tag{3.4}$$

If R$\Delta\beta$ = Δl, then,

$$\frac{\partial\beta}{\partial\lambda} = \frac{1}{R\left(\frac{\Delta\beta}{\Delta\lambda}\right)} \tag{3.5}$$

From equation 3.3,

$$\frac{d\lambda}{dl} = \frac{dcos\beta}{mR} = \left(\frac{cos\beta}{mR}\right) \times 8.33 \times 10^{-4} mm \tag{3.6}$$

where R is the radius of curvature of the Rowland circle measured in meters. These expressions are not sufficient to completely describe the spectrometric system as they assume a fixed angle of incidence and the exit arm is expected to be rotatable to collect signal at different points along the Rowland circle. For a spectrometer with fixed exit arm as in our case, an off-Rowland Mount is used to solve the problem.

The off-Rowland mounting system for a concave grating operates by moving the grating on a fixed path along the bisector while rotating it through an angle θ to the grating normal. The original state is θ = 0, and α = β, the centre of Rowland circle is positioned as the bisector of the entrance arm. When the grating is rotated, a portion of the inside spectrum appears on the exit slit/detector, the grating and the Rowland circle are correspondingly rotated through an angle θ and shifted a distance x along the bisector as shown in figure 3.9.

For the off-Rowland setting, the entrance slit and exit slit each have a displacement s and s' respectively after the grating was shifted. From the diagram we have:

$$Rcos\alpha + s = Rcos\beta - s' \tag{3.7}$$

where R is the radius of curvature of the grating. When the change in α over the observed wavelength range is small, we assume that $s = s'$, and let α_0 be the angle

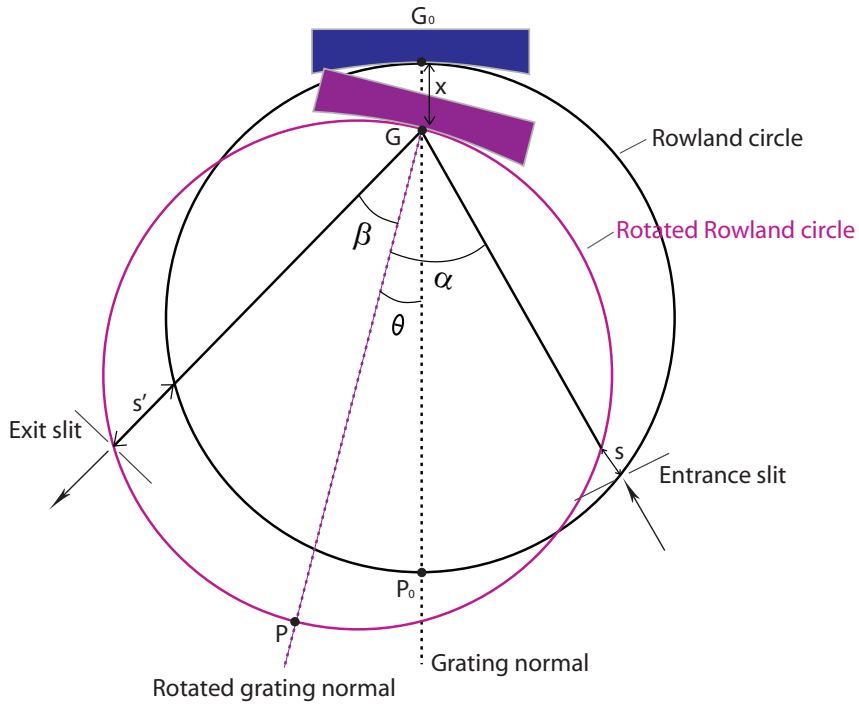

Figure 3.9: Off-Rowland mount configuration.

subtended by the entrance arm at $\theta = 0$, giving us that:

$$s = Rsin\alpha_0 sin\theta \tag{3.8}$$

From the diagram, $R = x + GP_0$ and $GP_0 \cong Rcos\theta$, the linear movement x can be written as:

$$x = R(1 - cos\theta) \tag{3.9}$$

The operating range of the spectrometer is 30 - 325 nm, the grating will rotate from 0^o to 20^o. Therefore the total linear translation of the grating along the grating normal will be from 0 to 60 mm. The grating currently used in the VM-521 spectrometer is blazed for a wavelength of 80 nm in the first order. In other words, the grating works most efficiently at reflecting light at 80 nm.

3.5 Resolving power of the spectrometry system

An important parameter is the resolving power which is defined as $\lambda/\Delta\lambda$. The theoretical limit to the resolving power of an instrument is given by Namioka ([67])

as:

$$\Delta\beta = \frac{\lambda}{Ndcos\beta} \tag{3.10}$$

When $\Delta\lambda$ is expressed in terms of $\Delta\beta$ as $\Delta\lambda = \Delta\beta(d\lambda/d\beta)$s, and from equation 3.5 and equation 3.10, we have

$$\Delta\lambda = \frac{\lambda}{mN} \tag{3.11}$$

So the resolving power is:

$$\lambda/\Delta\lambda = mN \tag{3.12}$$

where m is the order of the radiation and N is the number of illuminated grooves. More detailed information can be found in Namioka [67] and O'Leary [4]. In the current case of our off-Rowland mount, shown in figure 3.9, the entrance and the slit arm of the spectrometer are both set at 7.5^o to the normal. Thus $\alpha = 7.5 + \theta$ and $\beta = 7.5 - \theta$, where θ is the angle through which the grating has been rotated. The grating equation 3.2 is now rewritten as:

$$m\lambda = d\left(sin(7.5^o + \theta) - sin(7.5^o - \theta)\right) \tag{3.13}$$

it can be reduced to

$$m\lambda = 2d(cos7.5^o sin\theta) \tag{3.14}$$

The linear dispersion is redefined in terms of $\delta\theta$ so that

$$\frac{\delta\lambda}{\delta l} = \frac{\delta\lambda}{\delta\theta} \cdot \frac{\delta\theta}{\delta l} \tag{3.15}$$

From equation 3.14 we have

$$\frac{\delta\lambda}{\delta\theta} = \frac{2dcos7.5^o cos\theta}{m} \tag{3.16}$$

And

$$\frac{\delta\theta}{\delta l} = \frac{\delta\theta}{\delta\beta} \cdot \frac{\delta\beta}{\delta l} = \frac{1}{2} \cdot \frac{\delta\beta}{\delta l} = \frac{1}{2R} \tag{3.17}$$

The reciprocal linear dispersion of the grating as a function of grating angle is now written as

$$\frac{\delta\lambda_\theta}{\delta l} = \frac{dcos7.5^o cos\theta}{mR} \tag{3.18}$$

At the blaze wavelength of 80 nm where the grating is at an angle of 2.75^o to the grating normal, the dispersion is calculated to be about 0.83 nm/mm, which in agreement with the manufacturer's stated dispersion of 0.83 nm/mm. The actual

resolving power of the system can be estimated by Namioka's definition of $\Delta\lambda$ as

$$\Delta\lambda = \frac{W_s d}{m} \tag{3.19}$$

W_s is the standard slit width of 50 μm, then the corresponding instrumental width of the grating is 0.042 nm.

In the current work, the Andor^{TM} CCD is 26.6 mm wide and has 1024 pixels along this axis. The capture interval of the camera is about 22 nm. It means that the spectral distance between pixels is about 0.0215 nm. A previous estimate by Khater [7] using low pressure Helium and Argon discharges in the 75 - 85 nm range produced lines with had a Full Width at Half Maximum (FWHM) of about 2.1 pixels. Thus the instrumental width of the entire optical system was 0.045 nm at 80 nm, compared to the theoretically calculated value of 0.042 nm. The resolving power $\Delta\lambda/\lambda$ of the system using the values above is approximately 1780 at 80 nm using a 50 μm entrance slit.

3.6 Signal detection and recording system

The radiation detection system used in the LIBS experiments was a back-illuminated, VUV-sensitive Andor Technology^{TM} CCD (charged couple device) camera, model number DV420-BN. CCD cameras are devices which convert photons into electronic charge packets that can be stored, transferred, digitized and processed in the chip and by the associated readout and signal conditioning electronics. The CCD chip is a two dimensional array of Metal Oxide Semiconductor (MOS) capacitors. The capacitor is composed of a layer of silicon dioxide (SiO_2) grown on a silicon substrate; a metal electrode is then evaporated on top of the oxide layer, see figure 3.10. The metal electrode is known as the gate and is biased positively with respect to the silicon substrate.

When the gate is biased positively, photogenerated electron-hole pairs become separated and the electrons are attracted to the SiO_2 surface under the gate. It is similar to a p-n junction, the potential well formed under the gate contact is also called the depletion region which depletes the majority carriers (holes in p-type silicon). The amount of trapped charge in the potential well is proportional to the total integrated light flux incident on the CCD sensor during the measurement period. As the number of trapped electrons rises with increasing integration time and/or flux, the depletion region is widened, and the voltage between the gate and the p-type silicon is consequently increased. This voltage is in opposition to

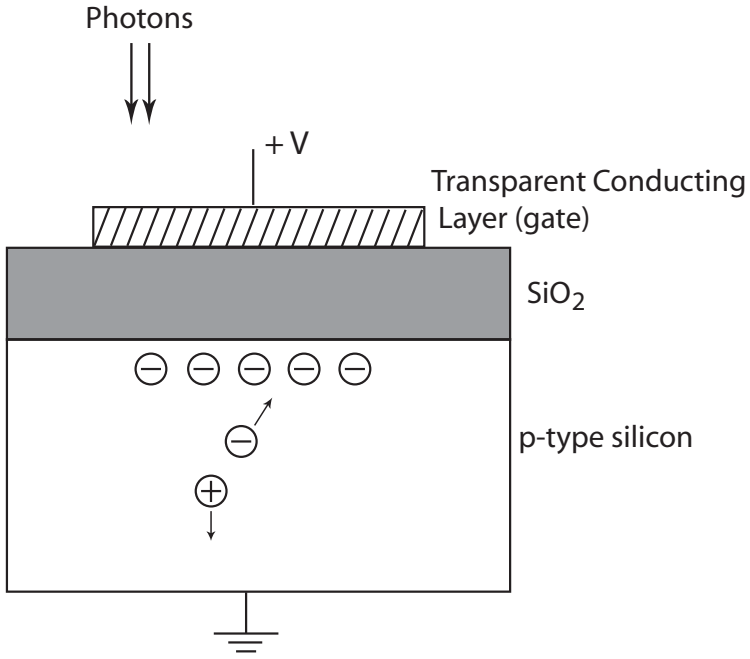

Figure 3.10: MOS capacitor structure.

the original gate bias, it is thus called the reverse-bias voltage. The strength of the depletion zone electric field is also increased as the reverse-bias voltage increases. Once the electric field strength is increased beyond a critical level, the depletion zone breaks down and the reverse-bias voltage reverts to the original level. This breakdown is reversible so long as the sensor is exposed to incident photons, and the process is repeated [68].

The basic design of a CCD is shown in figure 3.11 to demonstrate how the signal is read out. The geometric arrangement of the CCD pixels for the DV420-BN is a rectangular array of dimensions 1024×512. The electronic image intensity signal, represented by the geometric pattern of stored charges in the CCD pixel array, is read out by shifting each row vertically downward, one at a time, into the shift register which is then read out sequentially. After the pixel information in the shift register is read out, all rows are shifted down one row again and the new data in the shift register is read out.

In the LIBS experiments conducted in this work, the camera was used in "full vertical binning" mode. In this mode the charges stored in each vertical column are summed so that the final image is a one-dimensional (1D) one. This can be done quickly by adding each vertically clocked row to the previously accumulated values until all 512 rows in the case figure 3.11 have been added in the readout shift

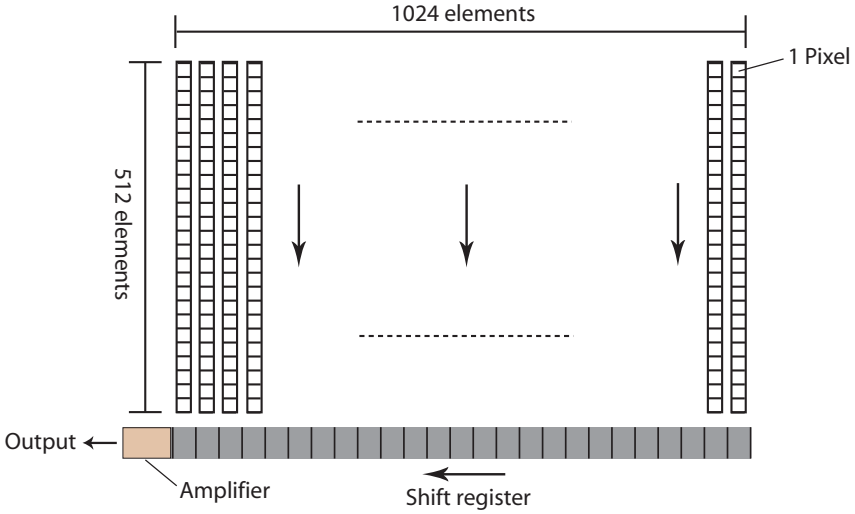

Figure 3.11: Design of a CCD.

register. The remaining 512 horizontal pixel values are then read out.

The thermally generated background signal (and hence the noise fluctuations on it) can be reduced by lowering the temperature of the CCD chip which is accomplished with the aid of a thermo-electric or Peltier cooler. The temperature for the Andor Technology camera can be reduced to -80^{o}C with water assisted cooling. Finally, read out noise, which is due to incomplete transfer of charge when the readout frequency is too high, can be reduced most obviously by increasing the readout time per pixel (i.e., reducing the readout frequency).

3.7 Summary

In this chapter, the equipment used in the LIBS experiments has been described. The major features of the experimental setup included the Nd:YAG lasers, the vacuum system, the spectrometer & grating and the CCD camera. All these components have been introduced and explained individually.

Chapter 4

Basic LIBS: Typical LIBS Analysis Process

This chapter provides a detailed description of the basic LIBS analysis procedure including the choice of laser parameters, CCD settings, data calibration steps which transfer the raw pixel data to analytical spectrum and finally some of the data handling needed to extract useful and reliable information from the spectra for LOD (limit of detection) calculation. In this chapter, carbon is chosen as the exemplar element as it is an important light element in steel. Carbon spectra from graphite and steel plasmas will be used to illustrate all of the above procedures.

4.1 Choice of laser pulse energies

The pulse energy of the Surelite laser could be attenuated by a combination of a half-wave plate and a polarizer. In single-pulse mode, the effect of laser energy in the range of 200mJ to 800mJ has been presented by Khater et al. [31]. In his work, line and background emission showed a monotonic increase with laser energy. In our experiment, the polarizer can be rotated from 0^o to 360^o, the corresponding output energy and the C 97.7 nm line intensity from a graphite sample are shown in figure 4.1.

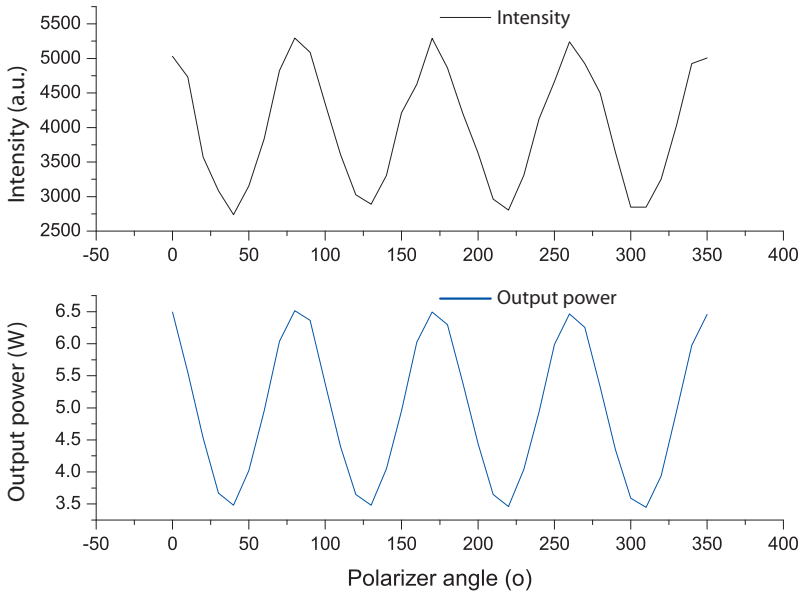

Figure 4.1: Top panel: Modulation of the 97.7 nm line intensity resulting from the laser pulse energy modulation shown in the panel below. Bottom panel: Modulation of the laser pulse energy obtained with the aid of a halfwave plate and a high power polariser combination.

As can be seen from the energy calibration curves, the average laser power was a little more than 6.5 watts and lowest was about 3.4 watts. The pulse repetition frequency was 10 Hz and therefore the estimated output pulse energy ranged from 650 mJ to 340 mJ. Within this energy range the intensity variation is proportional to the pulse energy.

4.2 Time-integrated space-resolved LIBS system

A fore-slit of 250 μm was placed in the chamber approximately 40 mm from the plasma and 350 mm from the entrance slit of the spectrometer. The combination of both slits yielded a spatial resolution of the plasma emission along the z-axis direction (perpendicular to the sample surface). Figure 4.2 schematically demonstrates the time-integrated and space-resolved (TISR) principle.

The laser beam comes from the right hand side along the z-axis, indicated by the red arrow in figure 4.2. The incoming laser beam is perpendicular to the sample surface. The plasma was observed to expand along the axis of incident laser beam (z-axis) but in the opposite direction. This direction is denoted as the plasma expansion direction here. As can be seen, the fore slit and the entrance slit are aligned normal of the plasma expansion direction. Radiation from the plasma can pass through the small gap, reach the grating in the spectrometer, be reflected onto the CCD and finally be recorded as a spectrum.

Only a 'slice' of the plasma radiation that passes through the small gap defined by the two slits is detected by the CCD camera. It is like observing the plasma radiation through the slits and so the position where the two slits are aligned is so called the observing position, denoted as P. The distance from P to the sample surface, denoted as s, is usually comparable to the size of the plasma because there will be too much continuum emission if P is too close to the sample surface ($s <$ 1 mm) where the very dense plasma core is, and the signal will be very weak if P is too far from the sample surface ($s >$ 10 mm) as the plasma will decay before expands to the observing position P. Thus an optimal observing position, yielding bright line emission and minimal continuum emission, will lie somewhere between 1 and 10 mm from the target surface.

By adjusting the relative position between the sample surface and the slit centre, emission intensity can be recorded at different observing positions. At one particular observing position P, for example, when s = 4 mm, the total emission from the plasma is implied by the curve in the bottom diagram in figure 4.2. However the recorded emission signal is only the shaded area in the diagram. The emission in the first 40 ns is not recorded because it takes about 40 ns for the plasma to expand to s = 4 mm and reach the observing position P. In fact, the very early stage of a plasma is often dominated by continuum emission [1] and thus, by keeping the observing position a certain distance above the sample surface, the continuum emission can be screened out efficiently, as indicated by the empty area covered by the dashed curve in figure 4.2.

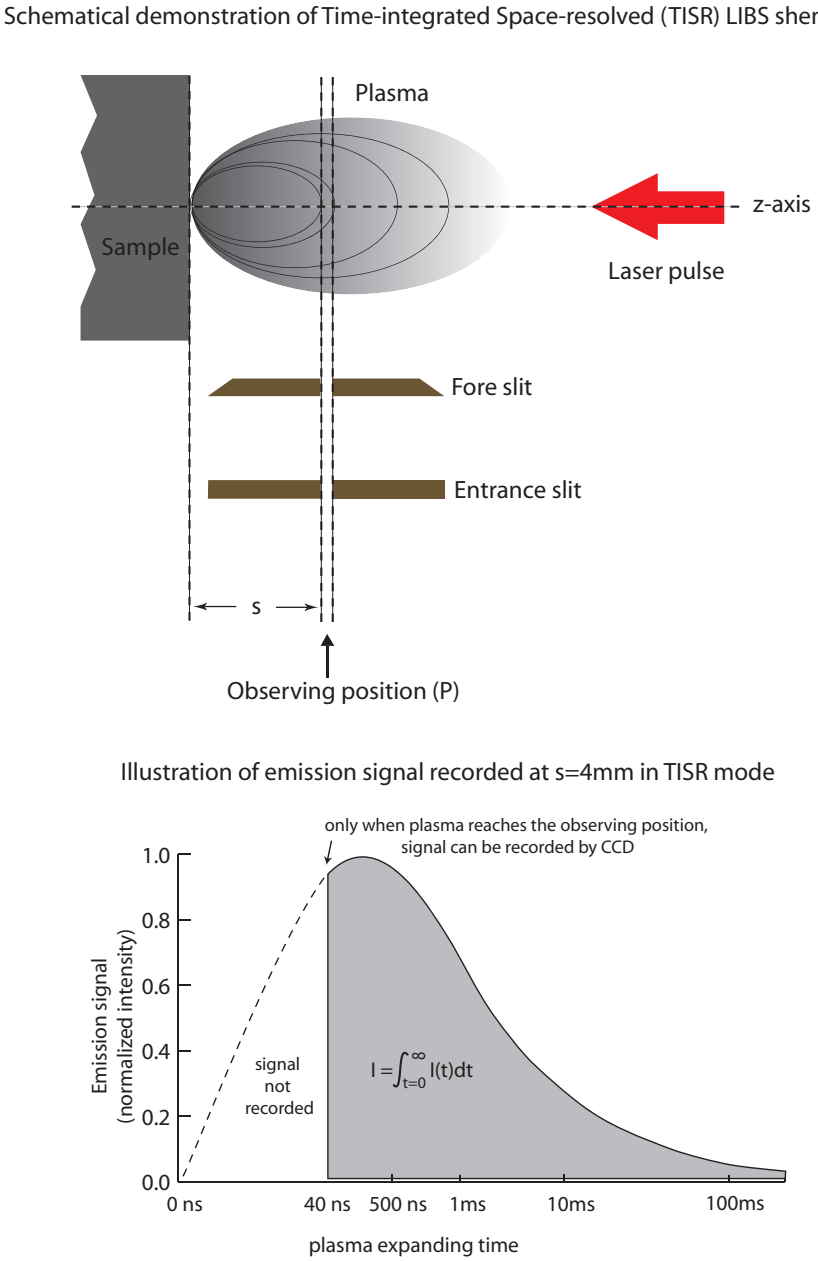

Figure 4.2: Schematic diagram of the observing position and the TISR scheme.

The CCD exposure time is usually set at one or more seconds so that the signal is recorded from the moment the expanding plasma reaches the observing position till the plasma completely decays (the shaded area in the bottom diagram in figure 4.2). This is so called the time-integrated space-resolved or TISR method.

In practice, a laser with a 10 Hz repetition rate is often used to generate the plasmas. In that case, one plasma is formed every 0.1 second and the emission signal from each plasma is recorded from the moment the plasma reaches the observing position till it decays (usually before the next plasma is formed). Within 1 second CCD exposure time, 10 plasmas are formed in sequence and the emission signal from each plasma is recorded by the space-resolved recording system, i.e., the continuum emission is screened out for each plasma while the characteristic emission is accumulated in one spectrum. Increasing the exposure time/shots number further will increase the detected VUV signal further but also the background level, this will be discussed later in section 4.4.

4.3 The optimal observing position

In the context of time-integrated space-resolved (TISR) LIBS, experiments were carried out to record the emission intensities at a number of observing positions from 2.5 - 5 mm. The spatially resolved intensity variations are shown in figure 4.3. The sample position and lens positions were moved synchronously along the z-axis to ensure that the focus condition of the laser beam was fixed while the relative position of the plasma and two aligned slits varied along z-axis. In other words, the signal-acquisition position (i.e. observing position) of the plasma was moved thus providing a spatially resolved intensity distribution along the z-axis.

As can be seen from figure 4.3, the intensity decreased with distance of the observing position from the sample target while the signal-to-background ratio (SBR) increased with it and reached a plateau at approximately 4.5 mm above the sample surface. Both intensity and SBR trends were quite similar in vacuum and gas (at different pressures). It shows that the observing position between 3.5 mm and 4.5 mm is a common optimal position for both vacuum and gas conditions. Unless specified, we use 4.0 mm as the observing position for all the experiments throughout the remaining chapters.

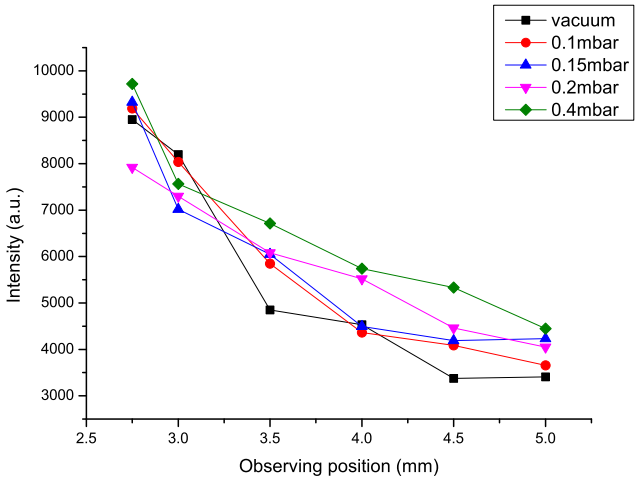

(a) Intensity

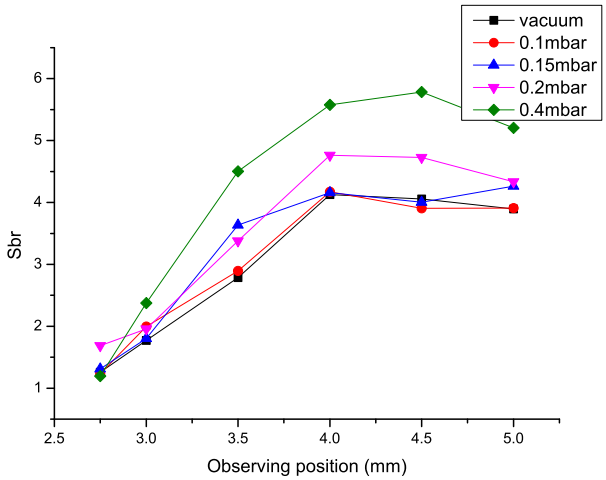

(b) S/B

Figure 4.3: C^{2+} 97.7 nm line intensity (4.3a) and signal to background ratio (SBR) (4.3b) at different observing positions along the z-axis.

4.4 CCD exposure time and number of shots accumulated

The number of single shot spectra accumulated for each spectrum is directly proportional to the CCD exposure time in our time-integrated LIBS system. As the pulse frequency (f_p) was fixed at 10 Hz (see the previous statement in section 3.1), we can easily obtain the relationship between the accumulated number of shots ($N_{(shots)}$) and the exposure time (T_{expo}):

$$N_{(shots)} = f_p \times T_{expo} = 10 \cdot T_{expo} \tag{4.1}$$

A large number of shots is desirable to increase the accumulated line intensity from the laser plasma, nevertheless one of the concerns with a large number of shots on target is the effect of plasma confinement in the cratered target [69]. The resulting plasma expansion from the target surface can be affected and the electron densities and temperatures in the crater can be altered. Along with the effect of plasma confinement, the more shots to be accumulated, the longer exposure time is needed (see equation 4.1), in that case the more dark noise signal is recorded in the spectrum. To optimize the number of shots, an experiment was carried out to record spectra with the accumulated shots number varying from 10 to 80. The corresponding variations of C^{2+} 97.7 nm line intensity and signal-to-background ratio (SBR) are shown in figure 4.4.

The raw line intensity increased with the number of shots while the SBR leveled off after the integration of 20 shots and started to drop from 60 shots integration onwards. The general trend of line intensity and SBR indicated that with the accumulation of between 20 and 30 shots, the intensity was fairly good and the SBR was optimal which was appealing for the final LOD calibration. We chose 20 shots (10 Hz with 2 second exposure time) for all the other experiments presented in this work. In double pulse mode, the number of shots accumulated for each spectrum is then 40 since two lasers both operate at 10 Hz and inter-pulse delay time was in the range of 0 - 10 μs, less than the pulse repetition period 0.1 s (1/(10 Hz)).

4.5 Wavelength calibration

The width of the spectra, over which the emission is captured by the CCD camera, is a little more than 21 nm (section 3.6). The wavelength range of the deep VUV region is more extensive and ranges from 30 nm to 130 nm. Therefore we recorded the spectrum in a number of intervals of less than 20 nm and joined them together

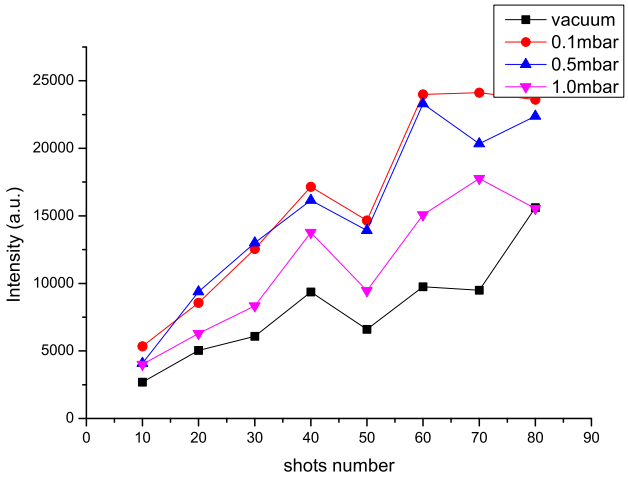

(a) intensity vs. shots number

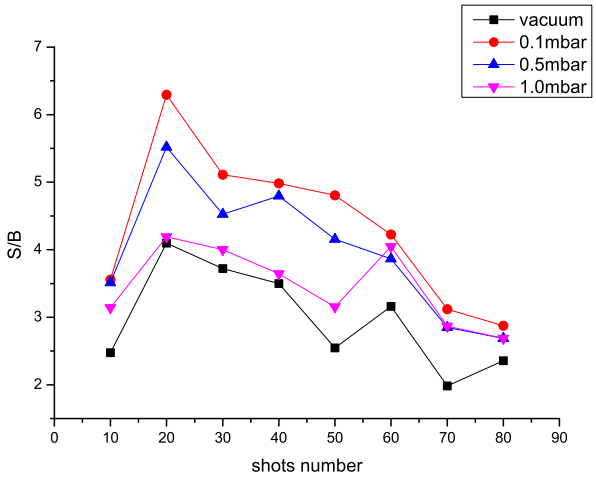

(b) SBR vs. shots number

Figure 4.4: Effect of accumulated shots number on intensity (4.4a) and signal-to-background ratio (SBR) (4.4b) in vacuum (■) and nitrogen at 0.1 mbar (●), 0.5 mbar (▲) and 1.0 mbar (▼).

to form a single trace as shown in Figure 4.5.

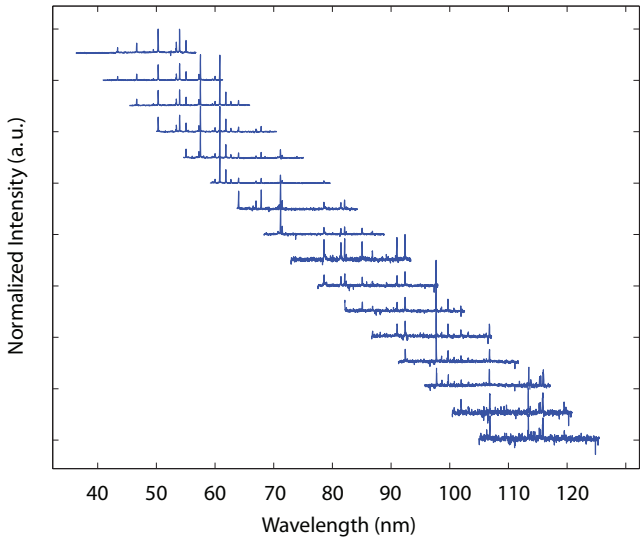

Figure 4.5: Series of carbon spectra from a graphite sample recorded with the LIBS system.

Each wavelength range was overlapped with the adjacent ones; they were joined together by matching corresponding peaks in the overlap regions. The x-axis scale in the figure is wavelength and the y-axis scale is the intensity (in CCD counts). The intensity of each spectrum was normalized to the maximum intensity (in each spectral segment) so the intensity range of each spectrum was normalised to (0, 1]. Sixteen spectra were taken to cover a major part of the VUV region (30nm to 130 nm). The center wavelength of each spectrum was varied from 35 nm to 110 nm in steps of 5 nm. To display all of the spectra in one figure, they were separated vertically by adding an intensity value of unity to each successive spectrum. The spectra were joined together to constitute the full spectrum of carbon in the deep VUV region as shown in figure 4.6. The x-axis scale is wavelength and the y-axis scale is intensity in relative CCD counts, i.e., spectra with different centre settings were multiplied by a normalising coefficient to match overlapping line intensities

The detector software does not have wavelength calibration tables for the type of spectrometer used in these experiments, so manual calibration of the wavelength scale was performed. The NIST spectral line database was used as the basic source of information on line position, and on relative intensities when lines from different ion stages were to be identified. The calibration of C neutral and ion lines is shown in figure 4.7.

By comparing the experimental spectrum and the corresponding spectrum ob-

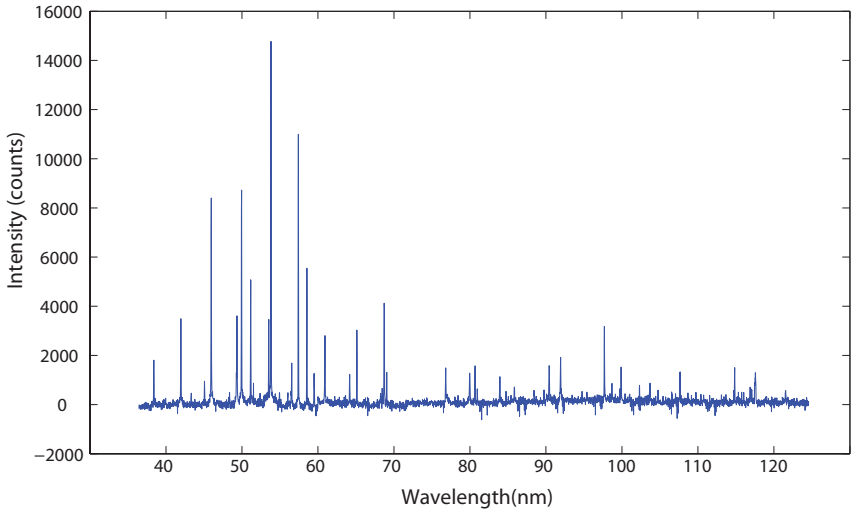

Figure 4.6: Wavelength calibration of carbon spectrum - step 1: composite carbon VUV spectrum (graphite sample).

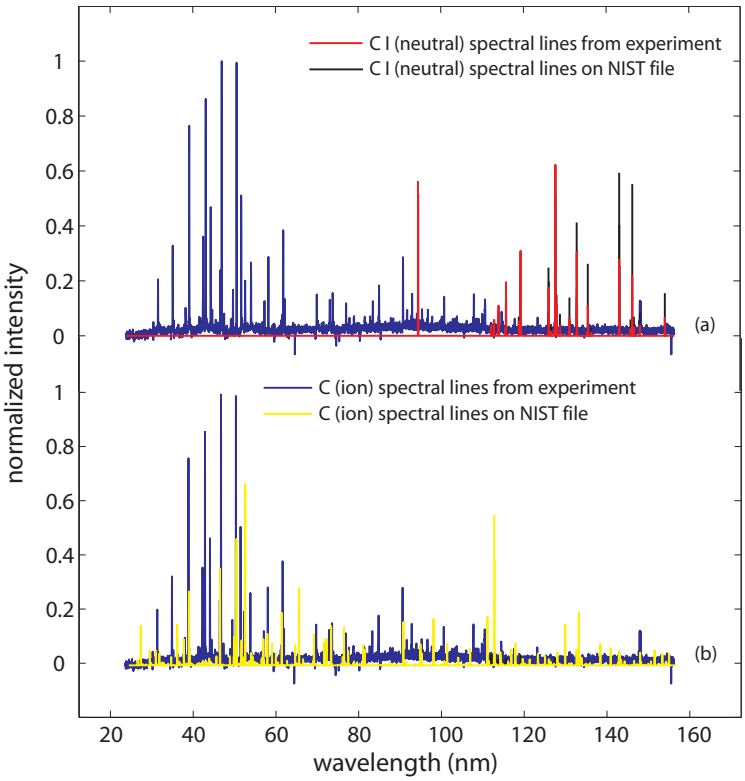

Figure 4.7: Wavelength calibration of carbon spectrum - step 2: spectral line reference and identification according to NIST.

tained from the NIST database, we obtained a calibrated VUV spectrum in the range of 70 nm to 105 nm which contained several strong emission lines of the analytes of interest. The spectrum with identified emission lines is shown in figure 4.8. As one can see, apart from those Fe (matrix element) lines, a number of highly charged ion lines from trace/light elements (C and S) were also found in this region. Among those lines, C^{2+} 97.7 nm line and S^{4+} 78.65 nm line were superior to other existing lines as they had a relatively high intensity and were isolated from other strong lines (thus avoiding a high background level). These two lines were chosen as representative trace elements to be studied intensively throughout the work.

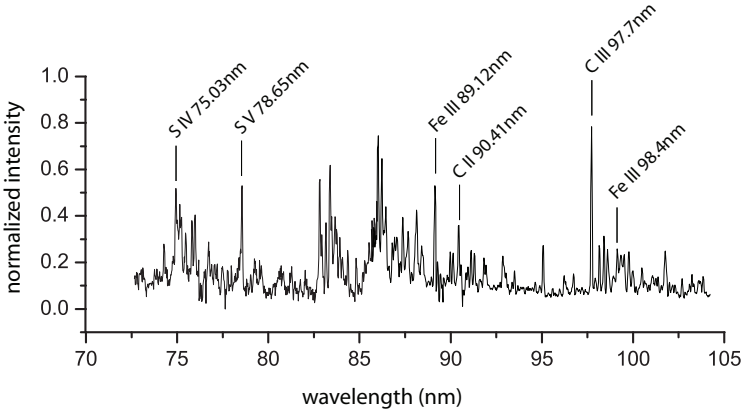

Figure 4.8: A typical VUV spectrum containing carbon and sulphur lines obtained from a steel plasma.

4.6 Data handling

The experimental settings have been discussed in the last few sections. In this section, two essential data handling processes which have been applied to the spectral analysis procedure are discussed.

One of the processes is *background elimination*, which simply refers to the reduction of the background on the spectra. The causes of the 'background' include the dark noise, the continuum emission, or even emission lines from other elements underneath or very close to the line of interest. As we have employed a water-cooling system for the CCD camera (chapter 3) to reduce the dark noise, we have also selected isolated spectral lines on the spectrum to eliminate the influence of other lines. The remaining cause of the background is then the continuum emission.

To eliminate the continuum emission on a spectrum, a computer program was developed to locate the "background area" near the selected spectral line, take records of the intensities in the background area and simulate the background intensity underneath the spectral line. Since the actual background continuum cannot be detected directly from the spectrum, the simulation process took the average value of the intensities in the background area near the selected spectral line. For each count on the intensity-axis (y-axis) that was integrated across the spectral line profile, an averaged background count was subtracted from the intensity count. The background underneath the chosen spectral line was then eliminated. By doing so, we have obtained a more reasonable value of the integrated "line intensity".

The other process to improve the calibration of limit of detection (LOD) is *internal referencing*. This approach uses relative intensities of the trace elements to the matrix element instead of absolute intensities of the trace elements for LOD calibration. It is based on the influence of the emission source, i.e. the plasma. To reduce the random errors we have taken a number of spectra and used the average value for the line intensity and repeated the procedure a few times to ensure the reproducibility. In this process, the plasma conditions (i.e. the plasma temperature and the electron density) vary for each spectrum. This type of variation applies to the absolute line intensities of the emission elements but can be adjusted by comparing them to the line intensity of another more "stable" element. This "stable" element must exist in each sample with a reasonably high concentration, and it must have distinct emission lines in the same spectral region chosen for the selected lines. Based on these considerations, the matrix element Fe is the best choice. It has a high concentration of more than 99.8% in each sample and has several strong lines in the VUV range. Since the influence of the plasma conditions (e.g. temperature) applies to all the species in the plasma, it can be canceled by dividing the Fe line intensity into the C or S line intensity.

Figure 4.9 gives an example of the calibration curve before and after internal referencing. Each data point in figure 4.9a was an integrated line intensity (with background elimination) of the C^{2+} 97.7 nm line. The linear fit of those data points has a high deviation. Figure 4.9b shows the results after internal referencing, the linear fit was much better than that in figure 4.9a. This procedure reduced the effect of the variation caused by the plasma and better reflected the variation of analyte concentration as a variation in carbon line emission intensity.

To complete the internal referencing process, the unit of intensity was converted from ratios (C/Fe) back to counts for the limit of detection (LOD) calculation. The conversion procedure was fairly simple, simply multiply the C/Fe ratios with the

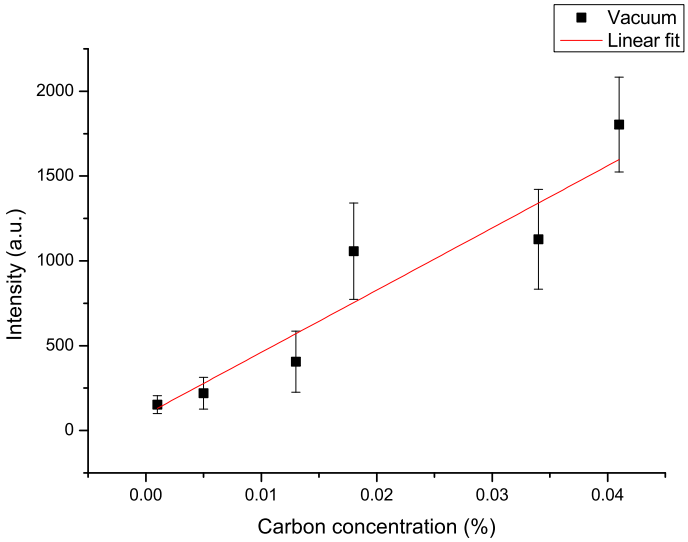

(a) Before internal referencing

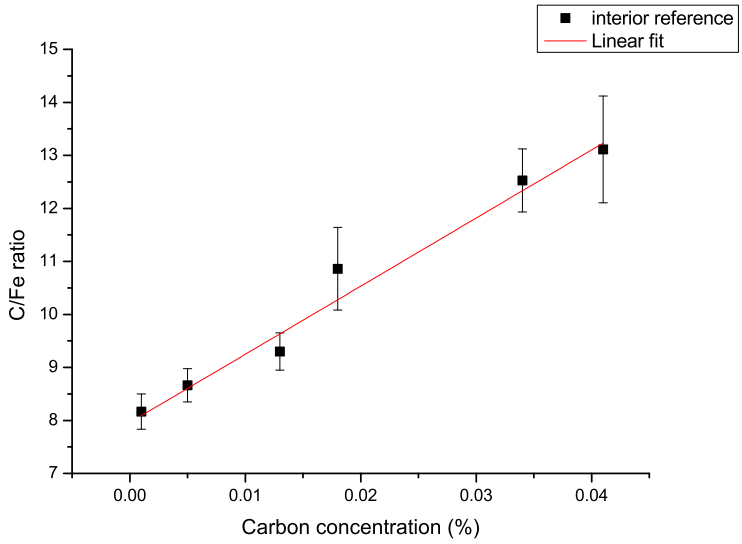

(b) After internal referencing

Figure 4.9: Interior referencing applied to calibration of C^{2+} 97.7 nm line intensity.

average absolute Fe line intensity. So the C/Fe ratios were converted to calibrated C line intensities. In this way, the original raw carbon line intensities were optimized for LOD calibration.

4.7 LOD calculation

The final step of a basic LIBS analysis is the limit of detection (LOD) calculation. We have introduced the definition of LOD in chapter 2 as,

$$L.O.D. = \frac{3\sigma}{S} \tag{4.2}$$

where σ is the standard deviation of the background and S is the slope of the calibrated LOD curve. To calculate the slope of the LOD curve is fairly simple. The linear fit to a basic LOD curve yields a function of intensity (y) v.s. concentration (x): $y = ax + b$. The slope of the linear fit is then the slope of the LOD curve:

$$S = \frac{dy}{dx} = \frac{\Delta y}{\Delta x} = \frac{y_2 - y_1}{x_2 - x_1} \tag{4.3}$$

so that any two well separated points on the fitted curve can define the LOD slope.

The standard deviation of the background is based on the background selection process. Close to the spectral line selected for LOD calculation, a line-free area is considered to be a background area. This background area is usually wider than the selected line width, it does not contain any spectral line and is not close to any other spectral line. These three criteria help us to define the background for the LOD calculation. A relatively "good" background area is wide enough to ensure a reliable standard deviation and is not affected by any other spectral line. Once the background area is selected, the standard deviation can be easily determined as:

$$\sigma = \sqrt{\frac{1}{N}\sum_{i=1}^{N}(x_i - \mu)^2}; \mu = \frac{1}{N}\sum_{i=1}^{N} x_i \tag{4.4}$$

With σ and S both determined, the LOD can be calculated from its definition.

4.8 Summary

This chapter introduced the basic procedure underlying a typical LIBS analysis. From the hardware settings (laser and CCD parameters) to the data acquisition

and handling, the basic LIBS analysis procedure is summarized in figure 4.10.

The procedure begins with the raw pixel data extracted directly from the CCD recordings. The first step is to calibrate and convert the count vs. pixel data to intensity vs. wavelength. Then identify the spectral lines with the aid of the standard database (NIST). The next step is to select spectral lines for the LOD calculation and to extract the line intensity of the selected line. The line intensity data is processed with background elimination and internal referencing. The processed data is converted back to the line intensity vs. concentration plot. This LOD plot is then ready for calculation. The linear fit to the LOD plot gives the value of the LOD slope, the standard deviation is determined from the background on the spectrum. With known values of both the LOD slope and the background standard deviation, the final LOD value is then determined by equation 4.2. This procedure is applied to every analysis process throughout the work. Unless specified, the intensities used in the current work are all from the processed data.

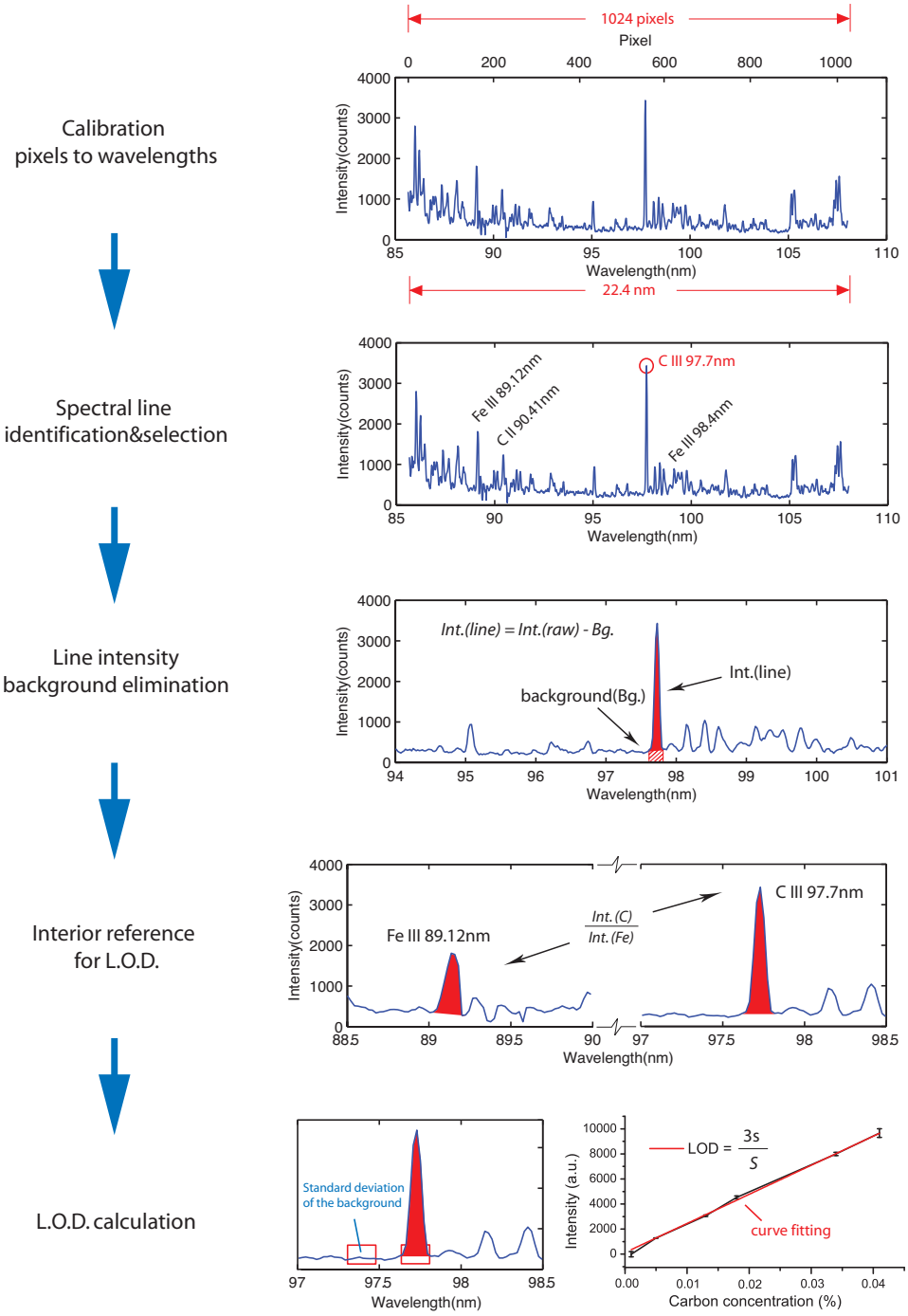

Figure 4.10: Basic LIBS analysis procedure.

Chapter 5

Dual-pulse LIBS in the VUV in Ambient Gases: Preliminary Results

In this chapter we will introduce two improvement techniques to the basic LIBS, which are the dual-pulse and ambient gas. Laser induced plasma (LIP) emission intensities in dual-pulse mode are compared to that in single-pulse mode. The emission behaviors in ambient gases are compared to those in vacuum. Some core parameters are optimized for dual-pulse with ambient gas configuration.

5.1 Introduction of two major technical improvements to basic LIBS

The ultimate goal of any quantitative LIBS analysis is to determine with high precision and accuracy the concentration of a species in a sample (e.g. parts-per-million), the absolute mass of a species (e.g. ng in a particle) or a surface concentration (e.g. ng/cm^2) [1]. The quantitative analysis usually begins with obtaining the calibration curve based on a set of (more than two) samples with given concentrations of an analyte. The concentration of this specific species in an unknown sample then can be calculated from the calibration curve. The analytical figure of merit for this type of LIBS analysis is termed the limit of detection (LOD). It is defined as the ratio of three times the standard deviation of the background on the spectrum to the slope of the calibration curve. Thus it is strongly dependent on the analysis conditions through out the LIBS process (from plasma formation, light emission to signal collection).

There are many parameters that affect the quantitative LIBS measurement. Some of these can be controlled, such as the laser harmonic and pulse energy, optical path and timing of the CCD, others are related to sampling or ablation processes over which there may not be a high degree of control. Besides these factors, the advantage of LIBS that materials can be directly sampled with little or no sample preparation is also a challenge because the physical and chemical properties of the sample can also have a strong effect on the quantitative data. A list of important parameters that affect a LIBS analysis is presented in table 5.1.

Source	Factor(s)	Comment
Laser(s)	Laser harmonics, pulse energy	section 4.1
	Single/Double pulse(s) operation	section 5.3
Detector	Exposure time,	section 4.4
Environment	Atmosphere above sample	section 5.4.1
Sample	Uniformity of composition/surface, Physical/Chemical matrix effect	

Table 5.1: Factors affecting quantitative LIBS analysis

In this list, laser harmonics decides the wavelength of the output laser pulse which was discussed in a previous work [7] by M. Khater. The laser pulse energy and the detector exposure time are categorized as hardware settings and have been discussed in the experimental chapter (chapter 3 Part II). The samples used in this work are standard steel samples purchased from Glen Spectra Reference

Materials^{TM}. Thus the composition of those samples was presumed to be constant and we refreshed the target surface by rotating the holder (section 3.2) frequently.

5.2 Experimental settings for dual-pulse LIBS in ambient gases

A number of technical upgrades were made to the conventional LIBS system which was introduced in the part I of this chapter. The main upgrades include a second laser and correspondingly an additional set of lenses and mirrors for dual-pulse generation, an inter-pulse delay-time generator and a needle valve, a gauge and a pressure meter for ambient gases supplement. The upgraded experimental setup is schematically illustrated in figure 5.1.

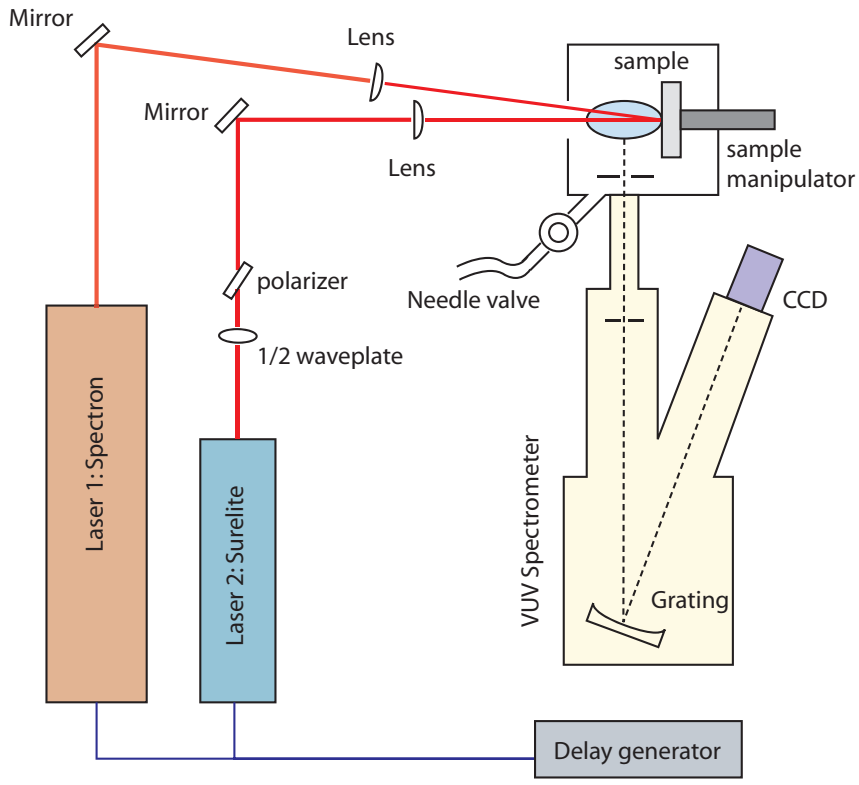

Figure 5.1: Experimental settings for dual-pulse LIBS VUV emission in ambient gas environment.

The two lasers are both Nd:YAG lasers. One is a Q-switched Continuum Surelite (model III-10), operating at the fundamental wavelength of 1064 nm with a pulse width of 6±1 ns and maximum output energy of 800 mJ (see part I sec-

tion 3.1). The second laser is a Spectron SL404 laser, also operating at 1064 nm wavelength with 200 mJ average pulse energy and 15 ns pulse width. The technical characteristics of two lasers are listed in table 5.2. Both Surelite and Spectron lasers produce approximately 10-mm-diameter beams which were focused by two plano-convex lens of 125 mm and 150 mm focal lengths respectively.

	Laser Model	
Characteristic	SL803	Surelite III-10
Manufacturer	Spectron, UK	Continuum, USA
Laser type	Q-switched Nd:YAG	Q-switched Nd:YAG
Wavelength	1064nm	1064nm
Max. O/P energy	450mJ	800mJ
Pulse width	12-15ns	5-7ns
Rep. Rate	10Hz	10Hz

Table 5.2: Main technical specifications of the two lasers used in dual pulse VUV LIBS experiments.

5.3 Dual-pulse LIBS operation

The basic idea of dual-pulse excitation is simply to provide a second time "energy input" to further enhance the optical emission from the plasma formed by the first laser. However there are different dual-pulse schemes. These schemes can be generally categorized into two types: collinear and orthogonal. With both configurations, LIBS emission signals and signal-to-background ratios have been found to be enhanced in many works (e.g. collinear [70, 71], orthogonal [72, 73]).

In the context of the LIBS VUV emission system, the ablation environment is usually set in vacuum or low-pressure ambient gas (below 1 mbar) to guarantee the transmission of VUV light. Thus the advantage of pre-spark approach [73] mostly used in orthogonal geometry is somehow limited. For ablation efficiency, dual-pulse operation is set in collinear geometry with re-heating configuration [74]. For versatility, two independently operating, separately triggered lasers were employed in this work. The pulses could be adjusted to overlap temporally or to be separated by any selected time intervals and the pulse energies could also be adjusted independently.

It is worth noting that while the dual-laser technique has been previously applied in conventional LIBS with temporally resolved detection, the current work is the first to investigate the dual-pulse technique for spatially-resolved time-integrated LIBS in the VUV spectral regime.

5.3.1 Inter-pulse delay generator

To begin with the investigation of the inter-pulse delay time effect, we introduce the inter-pulse generation system. Figure 5.2 gives a schematic illustration of the inter-pulse delay generation scheme.

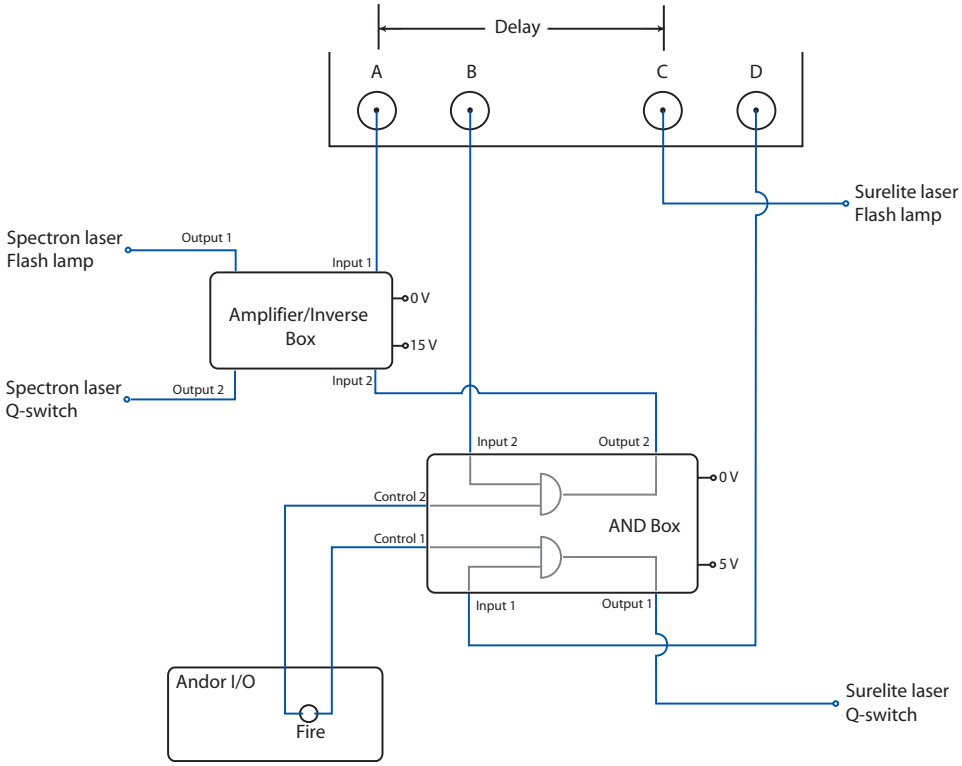

Figure 5.2: Inter-pulse delay time generation system.

The design of the delay generator is fairly simple, it contains an AND box with two AND gates, an amplifier box and an Andor I/O box. The Andor delay-gate generator has four I/O channels A, B, C and D. In our experiments, A and B were assigned to the Q-switch and flashlamp respectively of the Spectron laser, C and D were assigned to the Q-switch and flashlamp of the Surelite laser. Channel A provides a signal to initiate the flashlamp of the Spectron laser which will be providing ablation pulses in the double-pulse mode. Channel B is connected to one of the input ports of the AND gate in the AND box, the other input port of this AND gate is triggered by the Andor I/O FIRE. Channel C provides the signal to start the flashlamp of the Surelite laser which provides the reheating pulses. Channel D is connected to one of the input ports of the other AND gate in the AND box which is also triggered by the Andor I/O FIRE, similar to channel B. There are fixed response

time intervals between channel A and B, C and D (usually in the range of μs). This fixed delay time ensures that the peaks of the flashlamp pulses are overlapped so that the population inversions in each rod are at, or near, maximum when the Q-switches are opened. Hence the Pockels cell can be both opened simultaneously for overlapping optical pulses or delayed with respect to each other in time intervals small compared to each flashlamp pump cycle, typically 0 - 10 microseconds for typical flashlamp cycle times in the 150 to 300 microsecond range. Hence the actual inter-pulse delay is the time delay between channels A and C and it can be adjusted to either positive values (Surelite pulse after the Spectron pulse) or negative values (Surelite pulse before the Spectron pulse).

5.3.2 Dual-pulse LIBS spectrum

To see the differences that dual-pulse excitation has made on the emission spectra, we investigated the spectrum in single- and double-pulse mode in vacuum. Sample spectra are shown in figure 5.3. The top spectrum (a) was recorded in single-pulse mode with the Spectron laser only (pulse energy 200 mJ). The second spectrum (b) was recorded in single-pulse mode with the Surelite laser only (pulse energy 465 mJ). The third spectrum (c) is simply a sum of the above two spectra in single-pulse mode. The next spectrum (d) was taken using single-pulse excitation (using the Surelite laser) with an energy equal to the sum of the first two single-pulse excitation energies (i.e., E_{exc}(d) = E_{exc}(a)+E_{exc}(b), 665 mJ = 200 mJ + 465 mJ). The last spectrum (e) was taken using dual-pulse excitation with a 200 mJ Spectron pulse as the ablating pulse and a 465 mJ Surelite pulse as the reheating pulse.

The first thing one can easily see from the spectra comparison is that the signal enhancement in dual-pulse excitation (e) is greater than any of the other single-pulse cases. Start the comparison from the top spectra (a) and (b), both spectra were taken in single-pulse mode except the excitation pulse energy in case (b) is more than twice that in case (a). However the signal gain is barely seen on the spectra. Next we summed the signals in (a) and (b) obtaining a new spectrum (c). We also combined the pulse energies in (a) and (b), and recorded a spectrum (d) using the combined excitation energy. The signal with combined excitation energy in (d) was indeed greater than that in (a) and (b), but it was less than the sum of the signals in (c). It is hence clear that with the same total amount of excitation energy, two separated single pulses produced more total emission than one single pulse with the combined energy did. Finally those two excitation pulses as in (a) and (b) were operated in dual-pulse mode and the emission was recorded in (e).

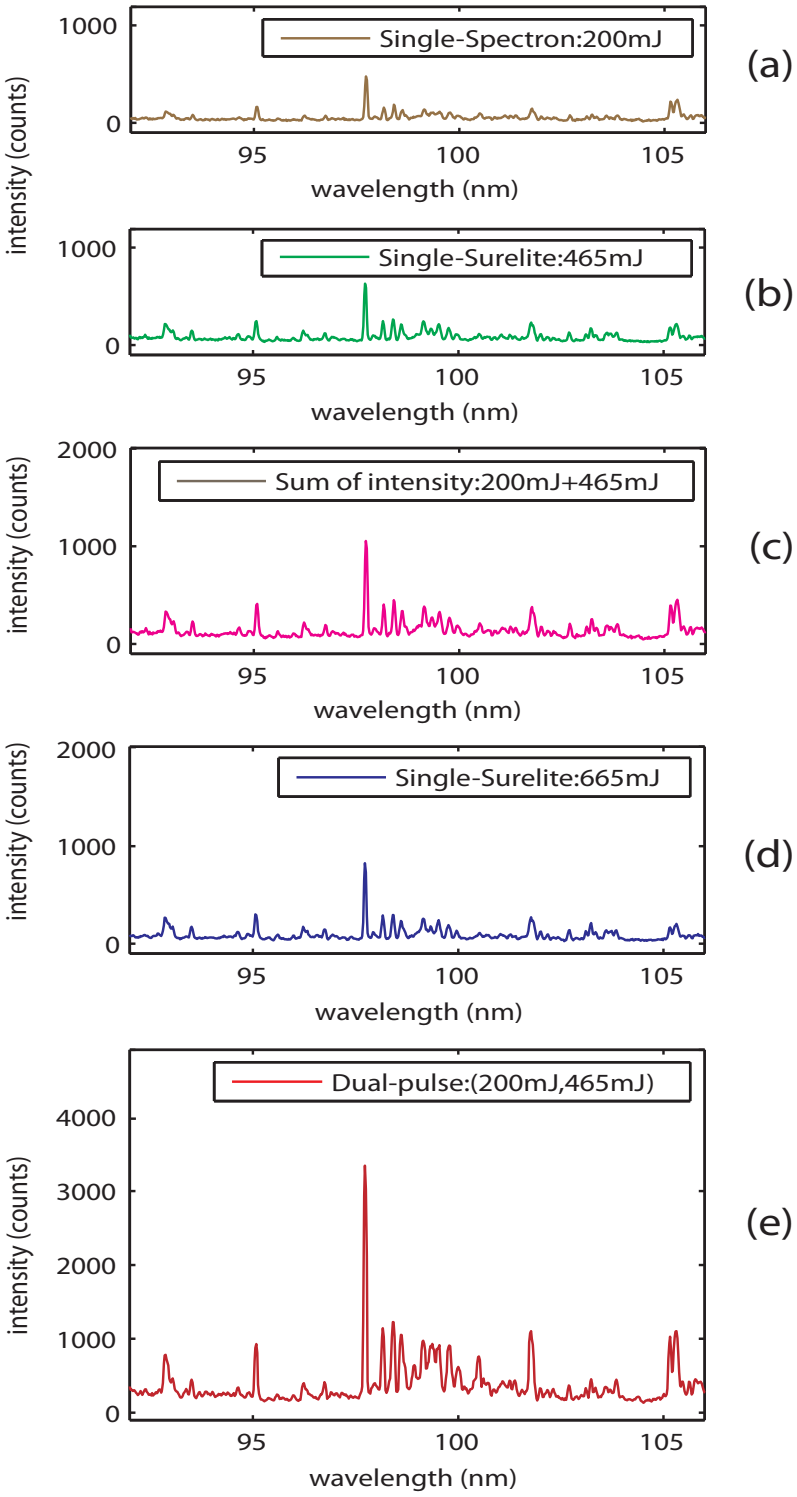

Figure 5.3: A spectra comparison of single- and double-pulse excitation with different energies.

The peak signal in (e) with dual-pulse excitation is about 3 times greater than the sum of the two individual spectra in (c) and nearly 4 times greater than that in (d) using one pulse with the same total amount of energy. It is clear that with the same total amount of energy, dual-pulse operation provides more signal enhancement than the two separated pulses do. The spectra also display background variations. Apart from the spectrum (c) as a summed result, judging from (a),(b),(d) and (e), the background level is proportional to the line intensity level. It is implied that the continuum emission level is affected in the same way as the line intensities by the excitation scheme and pulse energies.

To examine the intensity enhancement quantitatively and thoroughly, the integrated line intensity of the C^{2+} 97.7 nm spectral line was recorded with several different energy combinations. Note that the integrated line intensity is the intensity integration under the line area after subtracting the corresponding under-line background. By doing so any 'false line' (e.g. one single data point appearing at the line area is often caused by random error) and background noise are eliminated. The recorded intensities are shown in Table 5.3.

Case No.	Pulse energy 1^{st}	Pulse energy 2^{nd}	LIBS scheme	Intensity (counts)	Signal gain
1	200mJ	n/a	SP	1039	-
2	n/a	300mJ	SP	1553	-
3	n/a	465mJ	SP	1652	-
4	n/a	665mJ	SP	1769	-
5	200mJ	300mJ	DP	6249	2.4
6	200mJ	465mJ	DP	7823	2.9
7	200mJ	665mJ	DP	8962	3.2

Table 5.3: Comparison of C^{2+} 97.7 nm line peak intensity in single-pulse (SP) and double-pulse (DP) configurations.

In table 5.3, case 1 corresponds to the Spectron laser (1064 nm, 200 mJ, 15 ns, 10 Hz) in single-pulse mode. Intensity values in cases 2, 3 and 4 were recorded in single-pulse mode with the Surelite laser (1064 nm, various outputs, 6 ns, 10 Hz) at three different energies. Cases 5, 6 and 7 correspond to the dual-pulse configuration in which the Spectron laser generated ablation pulses (at a fixed energy of 200 mJ) and the Surelite provided reheating pulses (at various energies, 300 mJ, 465 mJ and 665 mJ) in collinear geometry. All of the results were in vacuum and the exposure time was 2 seconds.

The last column in the table is the signal gain achieved in dual-pulse mode compared to the sum of the corresponding intensities in single-pulse mode. Since

the spectral comparison of the energy set (200 mJ (Spectron) + 465 mJ (Surelite)) has been provided earlier in figure 5.3, we take cases 1, 3, and 6 in table 5.3 for comparison purposes. The integrated intensities obtained with 200 mJ and 465 mJ in single-pulse mode were 1039 and 1652, respectively. The sum of these two values is 1039 + 1652 = 2691. Comparing the intensity sum of cases 1 and 3 to case 6 which used the corresponding 200 mJ pulse and 465 mJ in dual-pulse mode, the signal gain was calculated as: $7823/2691 \approx 2.9$. The same principle was applied to cases 5 and 7. As can be read from the table, the emission signal in DP mode was at lease twice as strong as that in SP mode. Also, with the same ablation energy (200 mJ), greater signal gain was achieved with higher reheating energy (case 7 $>$ case 6 $>$ case 5). It is indicated that stronger reheating pulses provide more signal gain within the current energy range in our experiment. For the following results and discussion the reheating pulse energy was set to 665mJ as it provided the greatest signal enhancement.

5.3.3 Optimal inter-pulse delay time

In the above dual-pulse scheme, the inter-pulse separation was set to 100 ns based on a scan of the intensity over an inter-pulse delay time ranging from 0 - 10 μs. A number of selected emission lines were examined over this inter-pulse delay (Δt) range. The scan result on the inter-pulse delay time is shown in figure 5.4. The experiments were carried out in vacuum with both lasers at their maximum output energies.

As can be seen from figure 5.4, from 0 delay time (simultaneous pulses) to 100 ns, the emission intensity increases rapidly. From 100 ns to 1 μs, the intensity goes through a fast decline, even dropping below the original point ($\Delta t = 0$). Subsequently, the intensity varies very little from 2 μs to 10 μs. The highest intensity is achieved within a time window of 20 ns around 100 ns. The intensity variation over the inter-pulse delay time for each spectral line is quite similar to each other. This similarity implies that the inter-pulse delay effect is independent of the emitting elements or the ion stages and that the intensity behavior of one spectral line can represent the laser induced plasma (LIP) emission behavior. In general, the emission behavior with inter-pulse delay time indicates an optimal Δt of approximately 100 ns.

Since the optimal inter-pulse delay is indicated around 100 ns, a closer look at the peak appearing within the first 500 ns is shown in figure 5.5. The inter-pulse delay time is increased from 0 to 600 ns in 50 ns steps, and in smaller steps (20 or

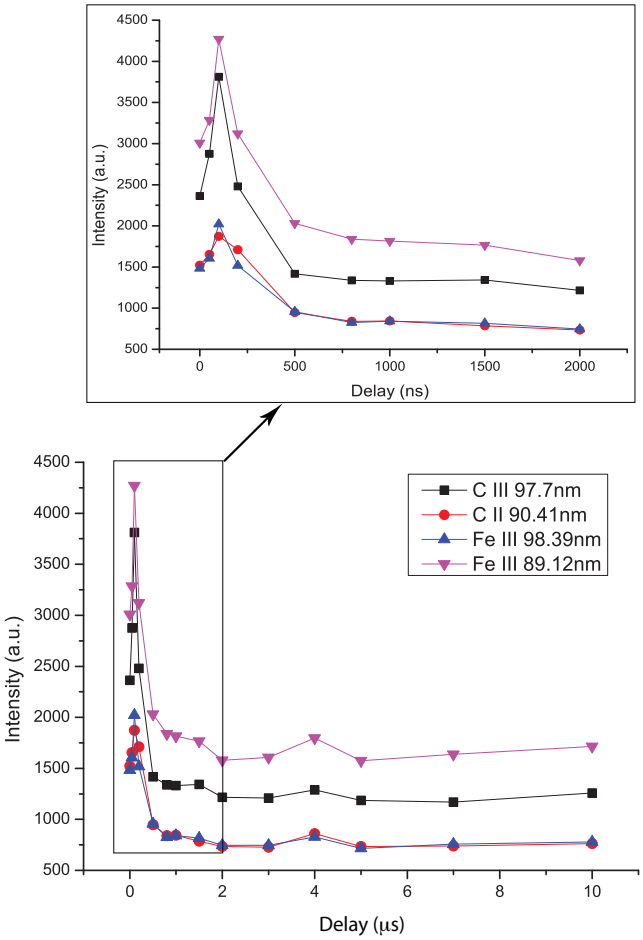

Figure 5.4: Intensity dependence on inter-pulse delay time of several spectral lines in vacuum condition: C^{2+}97.7nm(■), C^{+}90.41nm(●), Fe^{2+}98.4nm(▲) and Fe^{2+}89.12nm(▼). Spectron laser (1064 nm, 15 ns, 200 mJ) and Surelite laser (1064 nm, 6 ns, 665 mJ) in dual-pulse collinear reheating mode.

30 ns) near the peak area from 60 ns to 300 ns. To reduce the random error, each measurement contained 3 sets of Δt ranging from 0 to 600 ns and for each set of Δt, the intensities were recorded in a different order. For example, one measurement recorded the intensities at each Δt in the following order:

(50; 100; 0; 200; 20; 80; 120; 300; 280; 150; 320; 350; 180; 400; 450; 600; 500; 170; 220)

The next measurement recorded the intensities at the same set of Δt but in a different order:

(0; 100; 200; 150; 80; 120; 300; 350; 220; 180; 320; 20; 50; 450; 600; 80; 400; 170; 500)

The third measurement recorded the intensities in a different order to the above two. These three measurements were used to determine the average and the error-bars on each data point indicate the intensity fluctuations.

The detailed scan of the first intensity peak in vacuum is shown in figure 5.5 with a 4th polynomial fit to the curve indicating the peak position and the width of the peak. An optimal inter-pulse delay time of 100 ns within the range of $\pm$ 20 ns is indicated from the curve and the fitting. Based on the above discussion, the inter-pulse delay time for LIP emission intensity in vacuum is optimized to 100 $\pm$ 20 ns.

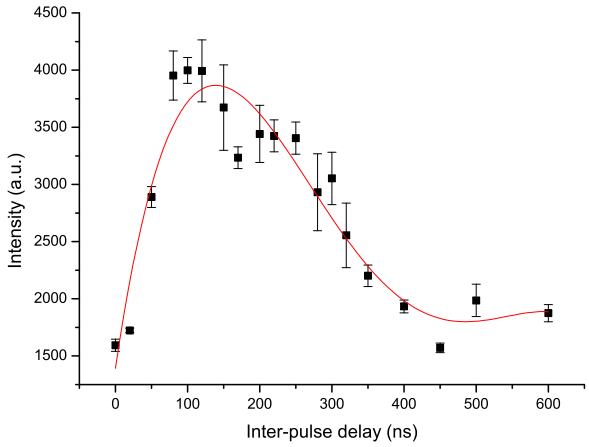

Figure 5.5: The peak intensity as a function of inter-pulse delay within the first 600 ns. C^{2+} 97.7 nm line. Spectron laser (1064 nm, 15 ns, 200 mJ) and Surelite laser (1064 nm, 6 ns, 665 mJ) in dual-pulse collinear reheating mode in vacuum.

5.4 Ambient gases

5.4.1 Emission in ambient gases

LIBS in ambient atmospheres has been performed over the past couple of decades. Not only is it a more natural situation in terms of industrial applications, there are also significant changes in the characteristics of the laser induced plasma (LIP) compared to the vacuum case. The main difference between LIP expansion into vacuum and gas is that instead of free expansion of the plume, a shock wave is formed in front of the expanding plasma as the ambient gas is compressed by the fast-moving particles at the front of the plasma plume. The confinement or the formation of the shock wave increases the collisions of the plasma species and so can be a complimentary to the LIP signal enhancement. A study of LIP in ambient gas with both single-pulse and dual-pulse operations was provided by Cristoforetti et al. [75]. Neutral and singly charged copper lines from LIP on a brass sample were investigated at different air pressures. An increase in the value of the emission signal was obtained in both single- and dual-pulse configurations for pressures ranging from 0.1 torr to 100 torr.

In what follows, we focus on dual-pulse LIBS VUV emission in ambient gaseous atmospheres, specifically in diatomic molecular nitrogen, atomic argon and atomic helium. The intensities of several selected emission lines from a number of species are plotted against gas pressure in figure 5.6. These species (and their corresponding emission lines) include the carbon trace element (C^+ 90.41 nm and C^{2+} 97.7 nm), the steel matrix (Fe^{2+} 98.12 nm and 98.4 nm) and the ambient gases (N^{2+} 91.6 nm and Ar^+ 91.98 nm). Helium does not have any distinct emission lines in this spectral region. Each data point is an average intensity for the corresponding emission line. The average intensity is the mean value of the selected line intensities obtained from three individual spectra taken under the same experimental setting (20 dual-pulses in 2 seconds). This process was performed before any spectral analysis to reduce the random error.

VUV emission in helium atmosphere

As can be seen from figure 5.6a, line intensities grow with helium pressure up to a value of ca. 30 mbar with perhaps a slightly decreasing trend from 30 mbar to 100 mbar, and remain almost constant for pressure in excess of this value up to 1 atmosphere. The pressure scale for helium shown in figure 5.6a is from vacuum to 350 mbar since very little difference is observed from 350 mbar to 1 atm. The next

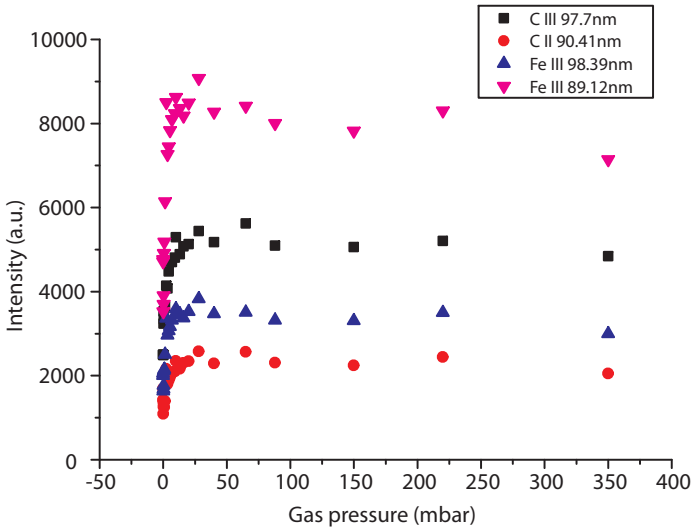

(a) Helium

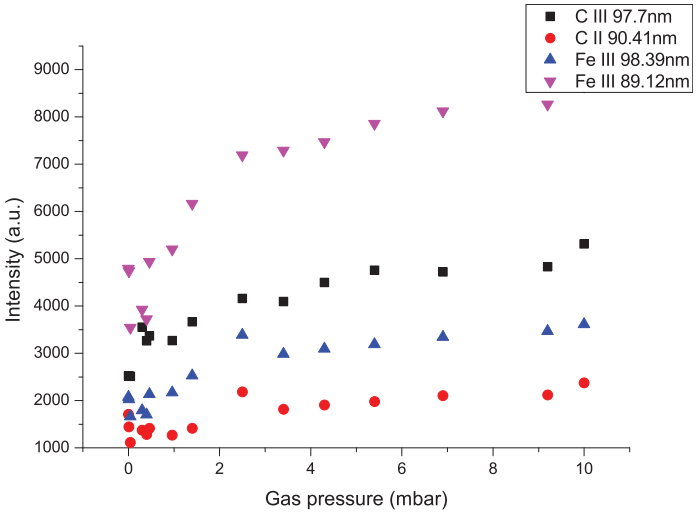

(b) Helium (within the first 10 mbar)

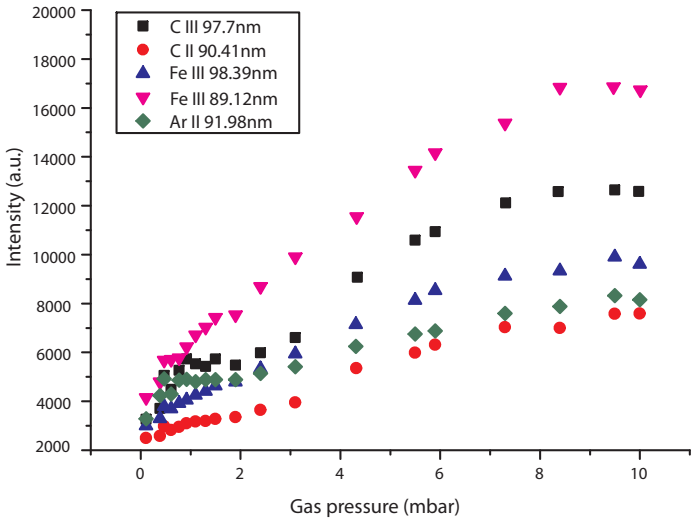

(a) Argon

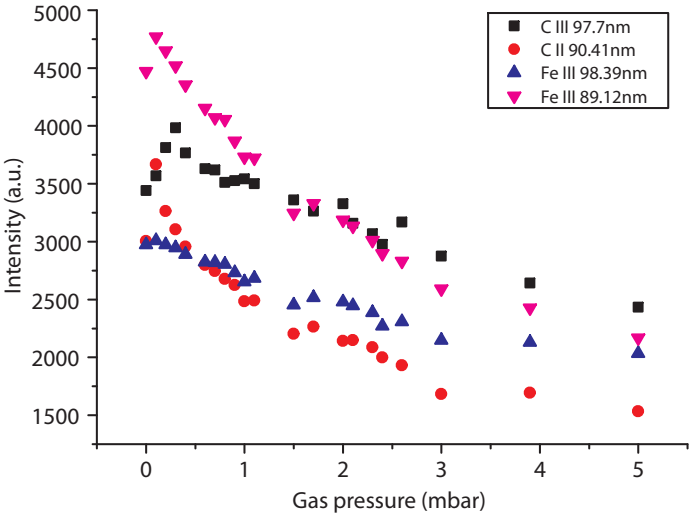

(b) Nitrogen

Figure 5.6: Emission intensity as a function of ambient gas pressure in helium with pressure from 0 to 400 mbar (a), a close look at the first 10 mbar in helium (b), in argon (c) and in nitrogen (d). Spectral lines presented: C^{2+}97.7 nm(■), C^{+}90.41 nm(●), Fe^{2+}98.39 nm(▲), Fe^{2+}89.12 nm(▼), gas element (N^{2+}91.6 nm or Ar^{+}91.98 nm)(◆). Spectron laser (1064 nm, 15 ns, 200 mJ) and Surelite laser (1064 nm, 6 ns, 665 mJ) in dual-pulse collinear reheating mode with inter-pulse delay 100ns.

figure 5.6b provides a close look at the intensity trend from vacuum to 10 mbar. The emission intensity increases rapidly with pressure in the first couple of mbars and slows down gradually as the helium pressure goes higher, the increase stops at around 30 mbar. The optimal helium pressure at which the highest emission signal is achieved is then 30 mbar within the range of $\pm$ 5 mbar.

VUV emission in argon atmosphere

The emission intensity in argon showed a steady increase with the argon pressure from vacuum to about 7 mbar. The increase slowed down from 7 to 8 mbar, reached a plateau at 8 mbar and remained relatively flat thereafter. As a matter of fact, the background continuum on the spectrum also increased with argon pressure. It became difficult to distinguish spectral lines from the overwhelming background level. This was observed directly from the spectra collected at higher gas pressures. Figure 5.7 shows a group of VUV spectra under different argon pressures ranging from 0.5 mbar to 10 mbar.

Note the two marks on the top spectrum, mark 1 corresponds to the C^{2+} 97.7 nm line, mark 2 is the Fe^{2+} 98.39 nm line. Tracking down these two lines on the spectra, one can see that the intensities of 1 and 2 increase dramatically with the argon pressure and so does the underlying background of those two lines. The line widths/ of these two lines are also increased. The intensity ratio of these two lines stays the same through out the comparison which indicates that the effect of ambient gas (argon in this case) is applied to the entire LIP emission. Comparing the bottom two spectra at higher pressures, it is also clear that background is not increased evenly over the spectra, which makes it more difficult to estimate the actual line intensity. Based on these observations the pressure scale for argon is limited to 10 mbar.

VUV emission in nitrogen atmosphere

The emission signal increase is only observed within the first 0.5 mbar in nitrogen. The intensity values decline dramatically with nitrogen pressures beyond 1 mbar. This is due to the strong absorption of VUV radiation by nitrogen gas.

To give a more detailed view on the absorption issue, the nitrogen transmission curve from vacuum to 1 mbar at 97.7 nm is plotted in figure 5.8(a). The recorded C^{2+} 97.7 nm line intensity extracted directly from the spectra is shown in figure 5.8(b). Each recorded intensity value was divided by the transmission coefficients calculated in (a) to correct the absorption by nitrogen, the absorption-

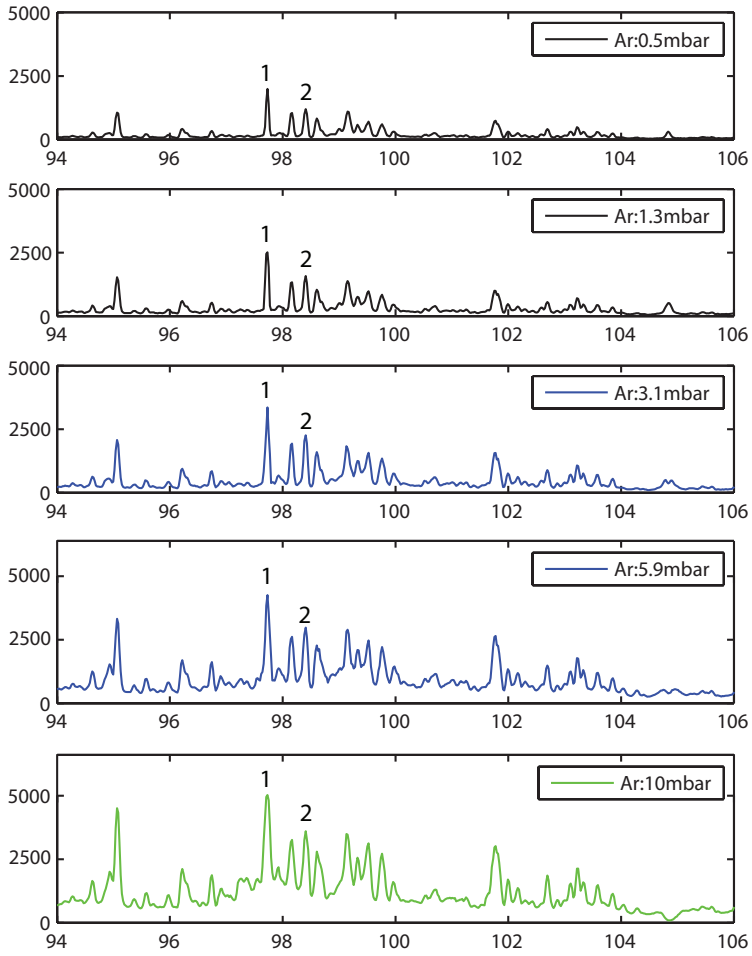

Figure 5.7: Several VUV spectra under different argon pressures. Spectron laser(1064nm,15ns,200mJ) and Surelite laser(1064 nm, 6 ns, 665 mJ) in dual-pulse collinear reheating mode with inter-pulse delay 100 ns.

corrected results are shown in figure 5.8(c). Because of the strong absorption, the emission signal gain due to gas buffering was significantly reduced by the absorption. The actual amount of radiation reaching the detector was even lower than that in vacuum, as shown in the intensity records.

Fortunately, the amount of VUV radiation that is transmitted through nitrogen gas can be calculated according to the standard database (CXRO, X-ray and matter interaction calculator). The transmission efficiency of VUV light in nitrogen at 97.7 nm is ca. 77% for a 10cm long column at a pressure of 0.1 mbar and it drops rapidly to 28% at 0.5 mbar, 8% at 1mbar and below 1% above 2 mbar. So the signal collected for a nitrogen pressure above 2 mbar is less than 1% of the signal without any absorption. The emission signal corrected from N_2 absorption, as shown in figure 5.8(c) suggests that the actual emission scale is approximately linear with gas pressure. In other words, the corrected emission signal would have been over 100 times more than the recorded signal.

It is interesting to investigate if the emission behavior in argon would be similar to that in nitrogen. Since argon is transparent to any wavelength longer than 78.4 nm (CXRO), a dramatic signal enhancement is expected when the argon pressure is significantly increased. However in the experiments, the line intensity reached a plateau and had very little signal gain beyond 8 mbar as shown in figure 5.6a. Although the intensity had a fast increase during the first few mbars, it represented a saturation at higher pressures. Thus the idea of correcting the recorded signal by the absorption coefficients to increase the intensity numerically was not practical in the current case.

5.4.2 VUV light transmission in ambient gases

It is not difficult to see that the absorption is not the only factor affecting the line intensity. There are a few other factors that must be considered for gas-plasma interaction. For example, the chemical properties of different gases. Nitrogen is a diatomic molecule with more chemical activity than argon and helium which are both single-atom rare gases. It may affect the collision between gas particles and plasma particles. Argon (Z = 18) and nitrogen (Z = 7) are relatively heavier gases than helium (Z = 2). This may affect the energy distribution between particles during collision. Also the thermal conductivity of helium (151.3×10^{-3} $Wm^{-1}K^{-1}$) is nearly 6 times that of nitrogen (25.83×10^{-3} $Wm^{-1}K^{-1}$), and about 8.5 times that of argon (17.72×10^{-3} $Wm^{-1}K^{-1}$). High thermal conductivity means that heat transfers to the gas rather well and so the expanding plasma can be expected to cool

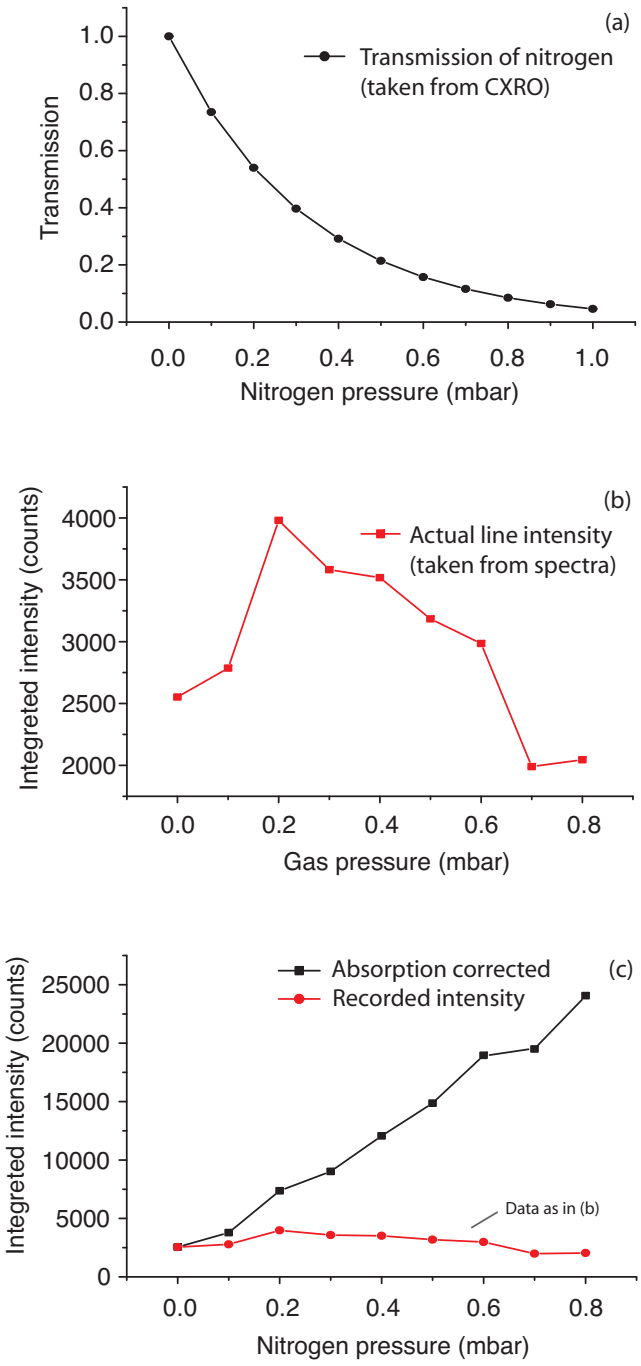

Figure 5.8: Influence of the nitrogen absorption on VUV emission. (a) Calculated nitrogen transmission curve for VUV radiation. (b) Recorded C^{2+} 97.7 nm line intensity from the spectrum. (c) Absorption corrected intensity compared to the recorded intensity. Spectron laser (1064 nm, 15 ns, 200 mJ) and Surelite laser (1064 nm, 6 ns, 665 mJ) in dual-pulse collinear reheating mode with inter-pulse delay 100ns.

rather rapidly. Since helium has the highest thermal conductivity among these three gases, the relatively low intensity in helium may be partly due to a lower plasma temperature.

For example, in the current time-integrated space-resolved LIBS scheme, one of the factors that is relevant to the recorded intensity at the 4 mm observing position (Figure 4.3) is the expansion velocity of the plasma plume. The position-time plots of an aluminum plasma front in ambient gas at several pressures from 2×10^{-2} Torr to 100 Torr were measured by Harilal et al. [76] using gated ICCD plume images. The results indicated that the plume expansion in the early stage ($\approx$ 40 ns) is almost linear irrespective of the background gas pressure and the estimated expansion velocity is $\approx 10^7$ cm/s. Based on these estimates, it takes about 40 ns for our plasma to reach the 4 mm observing position (0.4 cm/10^7 cm s^{-1}). Thus in the initial 40 ns, it takes about the same time in each ambient gas for the plasma plume to reach the observing position, the recorded intensity is then mostly affected by the plume expansion and evolution after that. The plume expansion is represented by a shock model given by [77]:

$$R = \xi_0 (E_0/\rho_0)^{1/5} t^{2/5} \tag{5.1}$$

where E_0 is the initial energy, ρ_0 is the density of the background gas. ξ_0 is a constant which depends on γ, the specific heat capacity:

$$\xi_0 = \left(\frac{5}{2}\right)^{2/5} \left(\frac{3}{4\pi}\right)^{1/5} \left(\frac{\gamma+1}{2}\right)^{2/5} \tag{5.2}$$

The above expressions related the plume front position R to the specific heat capacity ratio $(\gamma+1)^{2/5}$ and the background gas density $(\rho_0)^{-1/5}$. A simple conclusion can be drawn as that the plasma plume expands further in gases with a higher heat capacity ratio but lower density. The optimal expansion dynamics for spectroscopy analysis should be a balance between the background heat capacity and the density.

To fully understand the VUV emission behaviors in gases requires a comprehensive study of the physical and chemical properties of these gases first. It is, unfortunately, beyond the scope of the current work which is to investigate the dual-pulse LIBS VUV spectroscopy. So the discussion on ambient gases will not continue from here. The next step is to choose the optimum ambient conditions for the VUV spectroscopic analysis, mainly based on experimental observations.

As discussed above, ambient gases increase both the line intensity and the background continuum. However the background continuum is not desirable for

spectral analysis and often eliminated by the data handling process. High background continuum makes the elimination process more difficult. Thus signal to background ratio (SBR) is often used as a factor indicating the reliability of the processed line intensity. The line intensity and the signal to background (SBR) ratio of the C^{2+} 97.7 nm line in several ambient gases was examined and are shown in figure 5.9. For each gas the intensity was plotted under the SBR curve as a comparison.

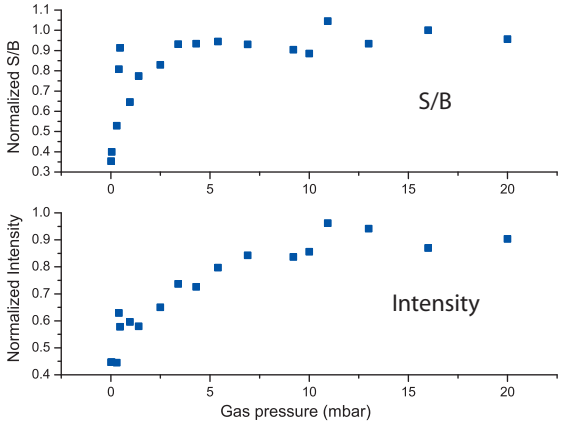

(a) Helium

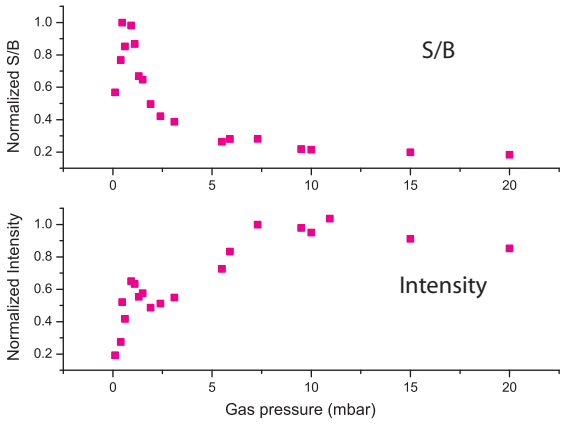

(b) Argon

The SBR in helium increases with gas pressure in the first few mbars and stabilizes after 5 mbar. The background level is saturated before the intensity growth, thus the optimal helium pressure is 30 mbar $\pm$ 5 mbar where both the highest intensity signal and SBR value can be achieved.

In argon the SBR dropped soon after the pressure reaches 2 - 3 mbar range while

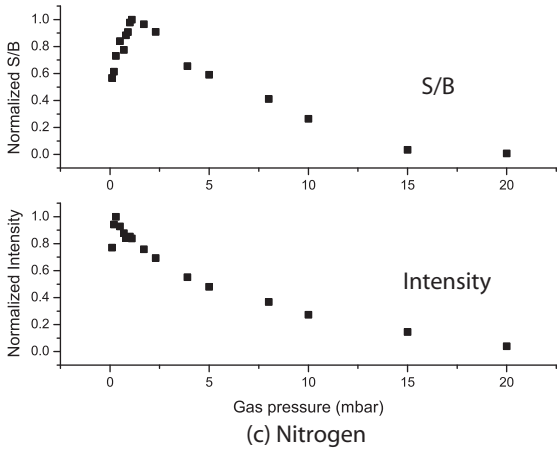

Figure 5.9: Signal to background ratio (SBR) and line intensity plot in three types of gases: (a) Helium, (b) Argon and (c) Nitrogen. Spectron laser (1064 nm, 15 ns, 200 mJ) and Surelite laser (1064 nm, 6 ns, 665 mJ) in dual-pulse collinear reheating mode with inter-pulse delay 100 ns.

the raw line intensity is still increasing right up to pressures in the 6 - 7 mbar range. As discussed earlier, this is due to the highly increased background level and is shown on the spectra (figure 5.7). The maximum SBR value is located between 1 - 2 mbar range indicating the optimal argon pressure for spectroscopic analysis.

For nitrogen, the SBR drops with intensity due to the strong absorption since the background emission is part of the VUV emission. The SBR curve peaks between 1 - 2 mbar and the intensity peaks between 0.1 - 0.5 mbar. For spectroscopic analysis, any nitrogen pressure under 2 mbar would be good as long as the recorded intensity is adequate. For the LOD calculation, lower nitrogen pressure is preferred as a high intensity signal is desired, especially for the trace elements with extremely low concentrations.

The above observations demonstrate that the VUV emission behavior of a metal plasma in a background gas is sensitive to both the gas type and pressure. Although the emission signal level may be dramatically enhanced (e.g., in argon at ca. 10 mBar), that does not mean that the signal-to-background or SBR is concomitantly enhanced. Therefore the optimal gas pressure for each gas should be determined individually. The signal intensity and the SBR should both be considered when choosing the optimal gas pressure.

5.5 Summary

So far, we have introduced two important techniques for LIBS enhancement which were dual-pulse excitation and ambient gases. In the above discussions, the laser beams were focused slightly under the sample surface and the inter-pulse delay time in the dual-pulse mode was set to 100 ns. These two factors, i.e. the laser beam defocusing and the inter-pulse separation are closely related to the laser ablation/reheating mechanism and can thus significantly affect the emission intensity and signal to background ratio (SBR). The optimization process for these two factors and quantitative investigations will be provided in the next chapter.

Chapter 6

Effects of Laser Beam Defocusing

In the course of parameter optimization, some of the parameters were found to significantly impact VUV emission in LIBS. One of them is the lens-to-sample distance. The lens-to-sample distance defines the focusing conditions of the laser beam: before focus (when focal point is under the target surface), on focus (focal point on the target) and beyond focus (focal point above the target). The power density on the target surface, the ablation efficiency and the spectral profile of the emitted radiation of the plasma are different for each focusing condition. In dual-pulse LIBS mode, the defocus effect refers to the defocusing of the second/reheating laser beam. The interaction between the second laser beam and the existing plasma is also affected by the focusing conditions. The effects of laser beam defocusing on VUV emission in single- and in dual-pulse mode are demonstrated in this chapter.

6.1 Defocusing effect in single-pulse mode

6.1.1 Observations of the laser beam defocusing effect

The effect of laser defocusing was studied by varying the lens-to-sample distance. In single-pulse mode, the Surelite laser, operating at the fundamental 1064 nm wavelength with a 6 ns pulse width (FWHM) and at its maximum output energy of 665 mJ was employed. By moving the focusing lens, the lens-to-sample distance was altered while the observing position (slit-to-sample distance) remained fixed. Figure 6.1 gives the details of the intensity dependence on the lens focusing condition. Three spectral lines, two from trace elements in steel (C^{2+} 97.7 nm, S^{4+} 78.65 nm) and one from the matrix element (Fe^{2+}98.4nm) were tested in the experiment and the intensities were normalized to unity.

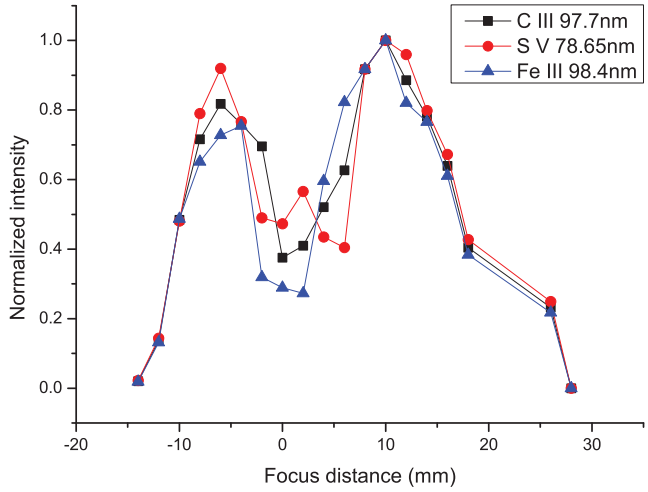

Figure 6.1: Effect of single-pulse laser beam defocusing. Intensities of C^{2+} 97.7 nm (■), S^{4+} 78.65 nm (●) and Fe^{2+}98.4 nm (▲) spectral lines are included. Plasma was generated by the Surelite laser (1064 nm, 6 ns, 665 mJ). The steel sample contains 0.041% carbon and 0.009% sulphur. The intensity of each line was normalized to unity for comparison reasons. Positive focus distance denotes that the laser beam was focused under the sample surface and negative position corresponds to the focus distance above the sample surface.

The variations in emission intensity for all three spectral lines are very similar. The highest intensities are achieved on either side of the tightest focus position (designated 0 mm on the x-axis). In one case, the laser beam was focused about 10 mm to 15 mm under the sample surface (positive x-values in figure 6.1). In the other case, the laser beam was focused 5 mm to 10 mm above the sample surface. In between there is a dramatic fall-off in the intensity which indicates that the tightest

focusing condition (from 5 mm above to 10 mm under the sample surface) is not the optimal condition to achieve the best emission signal. The intensity decrease at greater defocus, corresponding to large positive or negative x-values, is expected because the power density on the target surface is reduced due to the large spot size, which leads to less ablation of the sample and a lower temperature plume.

6.1.2 Discussion of defocusing effect in single-pulse mode

Similar behavior as a result of defocusing was observed by Harilal et al. [78] where the influence of spot size on the EUV conversion efficiency (CE) of CO_2 laser produced Sn plasmas. The best CE values were obtained at either side of the tightest focal position. It is indicated in their work that the most suitable CO_2 laser intensity for the optimum production of EUV radiation is a few mms away from the tightest focal position, where the CE is nearly 25% higher than at the smallest spot size. Harilal's work showed that the tightest focusing is not the optimal condition for laser-sample coupling which is in good agreement with our results. To further investigate the plasma emission behaviors with laser defocusing, a collisional-radiative model by Colombant and Tonon [79] is applied to the laser produced plasma.

For the emission element carbon in the current work, the relationship between the ratio of the number density of a given charge Z (n_z) to the total ion number density ($n_T = \sum_{k=1}^{Z} n_k$) and the electron temperature (T_e) is given in figure 6.2.

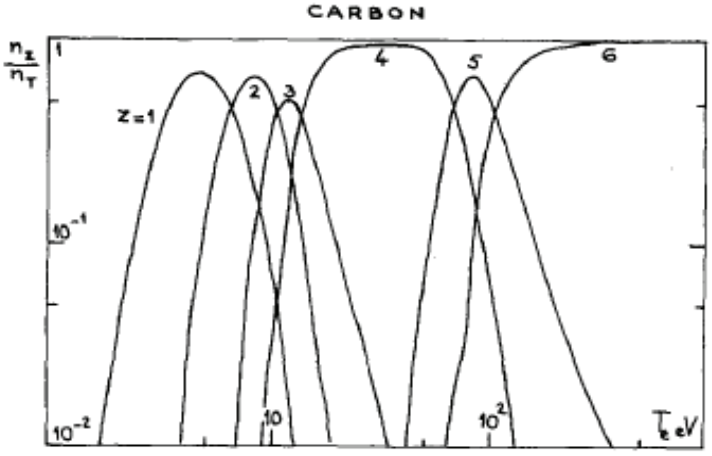

Figure 6.2: State of charge as a function of temperature for carbon, after Colombant and Tonon [79].

From the distribution one can see that when T_e lies below 10 eV and above 5 eV,

the dominant ion stages in the plasma are C^{2+} and C^{+}. When T_e lies between 10 eV to 100 eV, the plasma is predominantly composed of C^{2+}, C^{3+} and C^{4+}. When T_e is above 100 eV, the dominant ion stages in the plasma are C^{5+} and C^{6+}. To relate the laser irradiance to T_e, Colombant and Tonon also gave an equation to compute the initial plasma temperature in eV:

$$T_e(eV) \approx 5.2 \times 10^{-6} A^{1/5} [\lambda^2 \phi(W/cm^2)]^{3/5} \tag{6.1}$$

where the wavelength is in microns and A is in atomic mass units or amu.

In the current work, a Nd:YAG laser (1.064 μm, 6 ns) at the maximum output energy of 665 mJ was focused on a solid steel sample. The spot diameter in the tightest focusing condition was estimated to be about 200 μm (D = 2r), and so from equation 6.1 the initial plasma temperature was calculated to be about 112 eV. According to the ionization distribution in figure 6.2, in the tightest focus condition the dominant ions are C^{5+} and C^{6+}. It is clear from figure 6.2 that the C^{2+} is the dominant ion stage for plasma temperatures in the range of 5 - 10 eV. However what we require is C^{2+} in the excited state which can be produced either by collisional excitation of C^{2+} or recombination (radiative or 3-body capture of an electron) from higher ion stages, e.g., C^{3+} leaving the C^{2+} ion an excited state from which it decays, radiating a VUV photon. Hence we suggest that the optimal plasma temperature is one in which the electrons have sufficient energy to excite the C^{2+} ions and also to allow C^{3+} and C^{4+} to exist in substantial number densities. It is implied in figure 6.2 that a plasma temperature in the range of 10 - 20 eV is optimal.

The power density ϕ varies with the spot size (2r). For the spot size range from 200 μm to 4 mm (estimated results based on observation in our experiments), the power density varies from ca. 8.3 to 0.02 GW/cm^2 and the corresponding initial electron temperatures can be computed. If we assume that the focusing lens is an ideal thin lens with focal length f, the unfocused laser beam size is R, then the focusing spot size (2r) on the sample surface can be related to the lens-to-sample distance (d) as:

$$r = \frac{d}{f} R \tag{6.2}$$

The initial electron temperature as a function of focal distance can also be achieved. The dependence of T_e on power density ϕ and on the lens-to-sample distance d are plotted in figure 6.3. To simplify the model we first consider the focal point under sample surface condition.

From the second plot we can see that defocus range 5 - 12 mm corresponds to

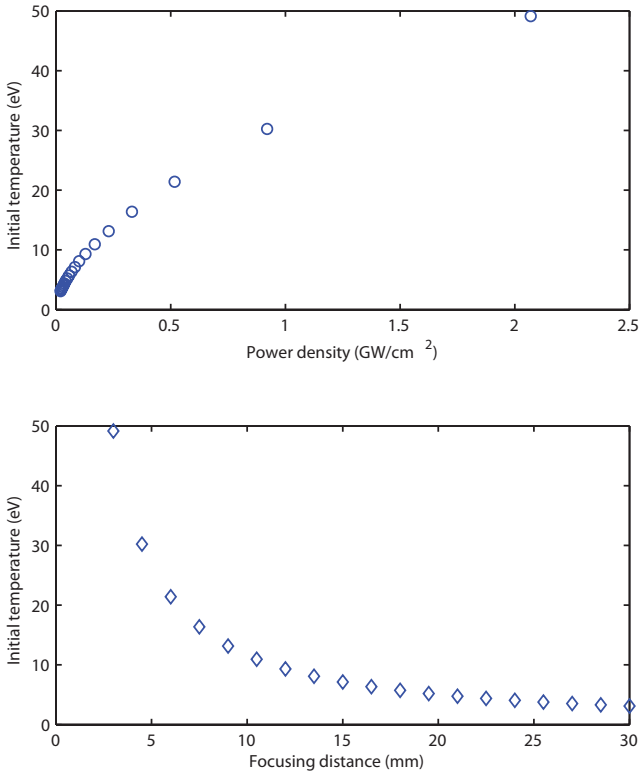

Figure 6.3: Calculated dependence of electron temperature on laser power density and on focusing distance for carbon.

the estimated optimal electron temperature 10 eV $\leq T_e \leq$ 20 eV. This is in agreement with the experimental observation in figure 6.1 that the maximum emission intensity was obtained at focus distances between 5 - 10 mm.

When the focal point is above the sample surface, the plasma temperature is expected to be higher because the plasma plume is expanding into the more tightly focused laser beam region where the laser beam power density is correspondingly higher than in the opposite case.

6.1.3 Summary of on-focus, before- and beyond-focus defocusing conditions

Based on the above discussion, the defocusing effect can be summarized as follows:

On-focus (focal point very close to sample surface).

At the tightest focus, the power density on the sample surface is the highest and the plasma temperature is the highest. The dominant ion stages could be significantly higher than 2+ (the ion stage of interest for the selected C^{2+} 97.7 nm line). Hence the 97.7 nm VUV emission is expected to be much reduced in the higher power density regimes. The highly ionized/high density plasma formed in this case tends to reflect a large portion of the laser radiation away from the plasma. The optical emission volume is also smaller due to the small spot size.

Before-focus (focal point under sample surface).

When the laser beam is focused under the sample surface, the signal intensity is increased due to the increased number of doubly charged ions in the plasma. The intensity is increased as the focus is pushed deeper and deeper under the surface until the enlarged spot size reduces the power density. The corresponding plasma temperature is reduced to under 10 eV which is not sufficient to maintain the 2+ ions radiation.

Beyond-focus (focal point above sample surface).

In this case the tightest focus point is above the sample surface. The focal point with the highest power density is hence in front of the expanding plasma. When the plasma expands into the tightly focused laser beam region, part of the pulse energy can interact with the plasma particles, causing a higher plasma temperature. In fact, the plasma is formed almost instantaneously when the laser pulse reaches and ablates the sample. The pulse duration of a typical Nd:YAG laser is usually 6 - 10 ns, thus it is possible for the above-surface focusing pulse to couple with and heat the plasma for a period of about 1 - 5 ns. The increased plasma temperature results in an increased emission intensity and the intensity will decline with further enlarged

spot size when the power density is below the level to maintain the 2+ ionization, similar to the mechanics in the 'before focusing' condition.

6.2 Defocusing effect in dual-pulse mode

6.2.1 Observations of the reheating pulse defocusing effect

The defocusing effect of the reheating pulse in dual-pulse mode is also investigated. The emission intensity dependence on focus distance in vacuum and in gas is shown in figure 6.4. Similar to the case of single-pulse in vacuum, the optimal focusing distance for C^{2+} 97.7 nm line intensity in dual-pulse mode is not the tightest focus position. In the defocusing range of -15 mm to 15 mm, the lowest intensity is obtained at -5 mm defocus position. The highest intensity is achieved at the defocus positions between 5 and 10 mm. Another intensity peak is observed at -10 mm defocusing. Different from that in single-pulse mode, the intensity peak at positive focus positions is wider and higher than the peak at negative focus positions. The optimal defocus condition for the second pulse in dual-pulse mode is considered to be 5 - 10 mm under the target surface.

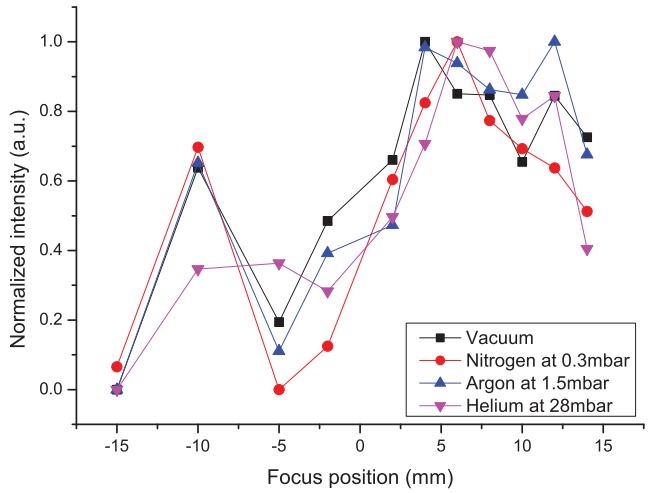

Figure 6.4: Effect of reheating laser beam defocusing in dual-pulse mode. Intensity of C^{2+} 97.7 nm line was recorded in vacuum (■) and three types of ambient gases: nitrogen at 0.3 mbar (●), argon at 1.5 mbar (▲) and helium at 28 mbar (▼). Intensities were normalized to (0,1) for easy comparison. Dual-pulse experiment was performed by the Spectron laser (1064 nm,15 ns,200 mJ) and the Surelite laser (1064 nm,6 ns,665 mJ) in collinear reheating mode with 100 ns inter-pulse delay. Positive focus distance indicates that the second laser beam was focused under the sample surface, negative distance corresponds to the above-surface defocusing.

6.2.2 Discussions of the reheating pulse defocusing effect

The reason for the lowest intensity is similar to that in vacuum. The over-heated plasma is dominated by highly charged species which are in the ion stages higher than 2+, thus the signal intensity we have recorded for C^{2+} line is actually the lowest.

In dual-pulse mode, the lowest intensity is achieved with -5 mm defocusing rather than the tightest focus condition (0 mm on-focus condition). This is due to the re-heating role played by the second pulse. As discussed in section 4.3, the initial plasma is dense and dominated by continuum emission in the first tens of ns (usually 40 ns) and so it would reflect most of the second pulse. Only when it expands beyond approximately 4 mm does it start to absorb the second pulse efficiently. Thus in the on-focus condition, most of the second pulse is reflected by the plasma and the C^{2+} line intensity recorded at the 4 mm observing position (section 4.3) is almost exclusively from the initial plasma which is not re-heated by the second laser beam. At the -5 mm focusing condition, the second pulse is focused in the "emitting zone" (4 - 5 mm) of the plasma. In this case the first plasma expanded beyond 4 mm and is just about to emit the characteristic spectral lines when it is re-heated by the second pulse to drive the average ionization state higher than 2+ and hence the bound-bound transition rate of $1s^2 2s^2$ - $1s^2 2s 2p$ corresponding to the 97.7 nm C^{2+} line is significantly reduced. Thus the intensity of this line is the lowest.

When the second laser pulse is focused under the sample surface between 5 mm to 10 mm, the second pulse not only re-heated the existing plasma but also ablated more material from the target since the tightest focused point with highest power density is inside the target. When the reheating laser beam is focused deeper below or further above the surface, the power density is reduced significantly by the larger spot size and hence signal intensity is no longer enhanced by the second pulse.

6.3 Summary

This chapter provided a study of the laser beam defocusing effect of LIBS in single-pulse mode and reheating laser beam defocusing effect in dual-pulse mode. In single-pulse mode, the lens-to-sample distance was optimized in vacuum. High emission signals were obtained at focusing positions a few mms (within 10 mms) above or under the sample surface. The observations were followed by a short

discussion of the emission behavior with focusing distance. The VUV emission intensity was also examined in dual-pulse mode with three different types of ambient gases. The intensity variations suggest an optimal defocusing distance of 5 - 10 mm under the target surface for all types of ambient gas. The emission behavior in dual-pulse mode is slightly different from that in single-pulse mode. An explanation and discussions are provided based on the comparison of defocusing in dual- and in single-pulse.

Chapter 7

The Effect of Inter-Pulse Delay

As can be seen from the optimization results of the inter-pulse delay in vacuum in chapter 5, the emission intensity varies dramatically with the inter-pulse delay time. In this chapter, the investigation of the inter-pulse delay effect is extended to ambient gases at different pressures and the inter-pulse delay range is extended to longer than 10 μs.

7.1 The inter-pulse delay effect in vacuum and in ambient gas

In section 5.3.3, the optimal inter-pulse delay time was measured to be 100 $\pm$ 20 ns for LIBS in vacuum. As shown in figure 5.4 of emission intensity vs. inter-pulse delay in vacuum in the earlier chapter, the maximum emission signal was about 2 - 3 times higher than the minimum signal. This is a significant influence of inter-pulse delay on the emission signal. We combined the dual-pulse technique with the use of ambient gases in section 5.4. The different emission behaviors in each ambient gas was considered to be a complex plasma evolution process related to the physical and chemical characteristics of gas and ambient pressure as well as the influence of gas (including absorption) on VUV emission in this particular case. These observations have raised the question of the inter-pulse delay effect in ambient gas, how would the inter-pulse delay effect be affected by the ambient gas? This section will provide a detailed investigation on the inter-pulse delay effect in ambient gas.

7.2 The 100 ns peak

Figure 7.1 shows the intensity dependence on the inter-pulse delay of the C^{2+} 97.7 nm line in three different ambient gases: nitrogen, argon and helium. To aid comparison, the intensity dependence on the inter-pulse delay in vacuum is also shown with plots.

In all the ambient gases examined in figure 7.1, a steep increase is observed during the first few tens of nanoseconds with a peak at Δt = 100 $\pm$ 20 ns. A sharp fall follows and the intensity gradually declines to the simultaneous-pulses intensity level (Δt = 0). Although there are some intensity variations from 1 - 10 μs on the curves in nitrogen and argon, the maximum intensity is achieved at an inter-pulse delay of 100 ns. Hence it is concluded that the optimal inter-pulse delay is 100 $\pm$ 20 ns for all three gases, very similar to that in vacuum.

Similar to that in vacuum, to verify the optimal inter-pulse delay time in ambient gases, we have closely examined the intensity variation and the corresponding uncertainty in the range of 0 - 600 ns. A polynomial fit was applied to each curve as shown in figure 5.5. The intensity vs. inter-pulse delay peak and fitting are shown in figure 7.2. Although the polynomial fit does not represent the intensity peak value, it does represent the optimum Δt position. From the curve fits one can see that, the highest 97.7 nm intensity is achieved at 100 ns while the intensities at Δt

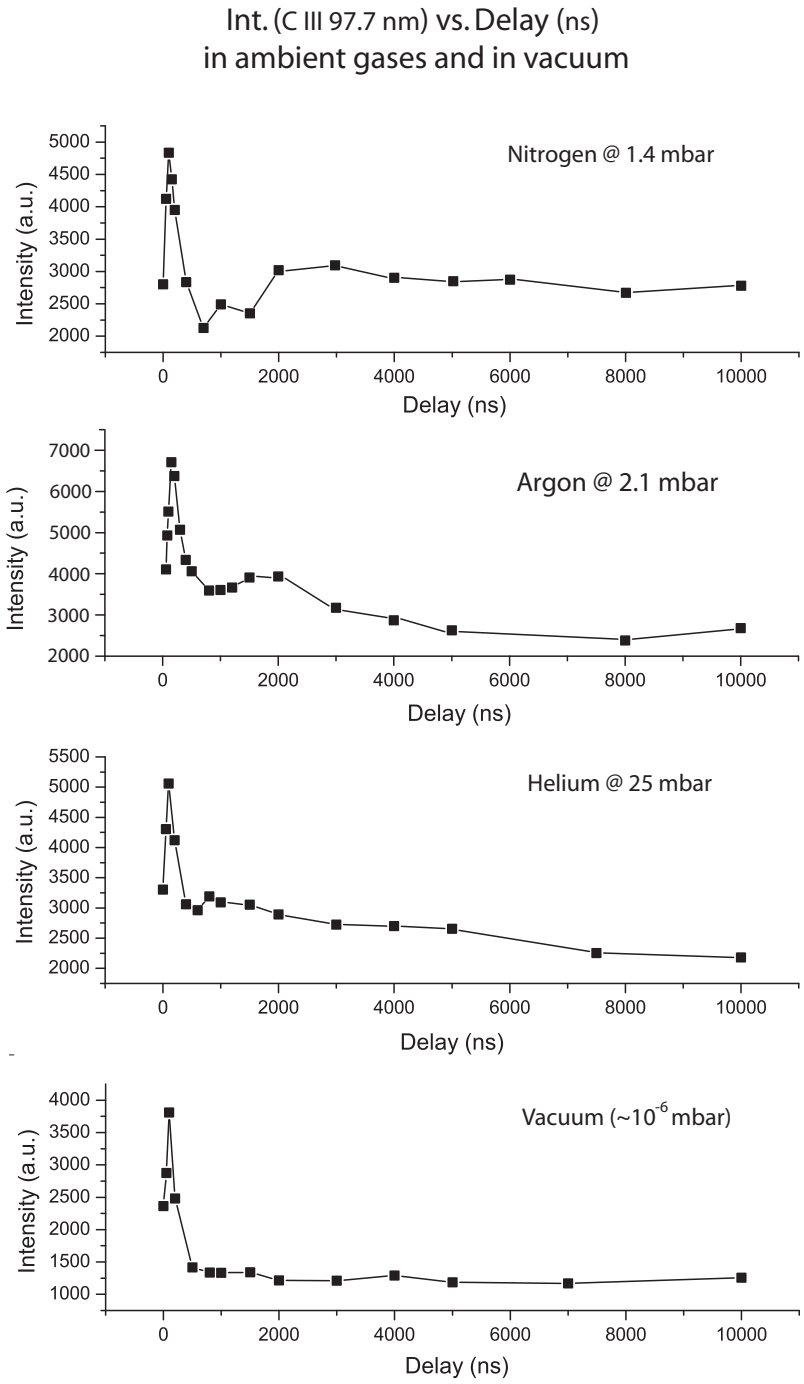

Figure 7.1: Variation of C^{2+} 97.7 nm line intensity with inter-pulse delay time in nitrogen at 1.0 mbar, in argon at 2.1 mbar, in helium at 25 mbar and in vacuum (10^{-6} mbar). Spectron laser (1064 nm, 15 ns, 200 mJ) and Surelite laser (1064 nm, 6 ns, 665 mJ) in dual-pulse collinear reheating mode.

= 80 ns or 120 ns are about 10% less than the peak value at Δt = 100 ns. The intensities obtained at these inter-pulse delays are significantly higher than the adjacent intensity values. Thus within the uncertainty range of 10% for maximum intensity, the estimated optimal inter-pulse delay time is 100 $\pm$ 20 ns.

7.3 The plateau and three questions about it

In figure 7.1, the intensity variation between 1 - 10 μs is worth noting. In the nitrogen and argon cases, the intensity peak at 100 ns is followed by a plateau area ranging from 1 μs out to 5 - 6 μs. The intensity plateau, implying a second intensity gain, declined either slowly in nitrogen or quickly in argon and remained stable in the time delay range of 8 - 10 μs. To examine the stability of the intensity after 10 μs, the intensity scan was extended up to 100 μs where no further intensity revival was observed. The plateau area in the 1 -5 μs delay range is much wider than the gain profile around the 100 ns peak, however the plateau intensity level is only roughly 1/3 of the peak intensity value achieved at 100 ns delay.

The plateau area on the curve is certainly of great interest but it is not as clear as the intensity peak at 100 ns delay and it is not unequivocal in all cases shown in figure 7.1. So a number of questions arise, namely:

1) Is the plateau an actual intensity revival?

2) What makes the plateau appear?

3) Could the enhancement of the plateau be more significant than the rather narrow peak at shorter delay times?

The following sections attempt to answer these above three questions in turn.

7.4 Is the plateau an actual intensity revival?

We have observed the plateaus on the intensity vs. inter-pulse delay curves in nitrogen and argon at one particular pressure in figure 7.1. However this plateau was not clearly represent on the curves in helium or vacuum. To verify the existence of the "plateau", the inter-pulse delay effect in each ambient gas will be discussed individually in the following few sub-sections.

7.4.1 Inter-pulse delay in nitrogen

The inter-pulse delay experiment was carried out at four different nitrogen pressures from 0.36 mbar to 5 mbar, as shown in figure 7.3.

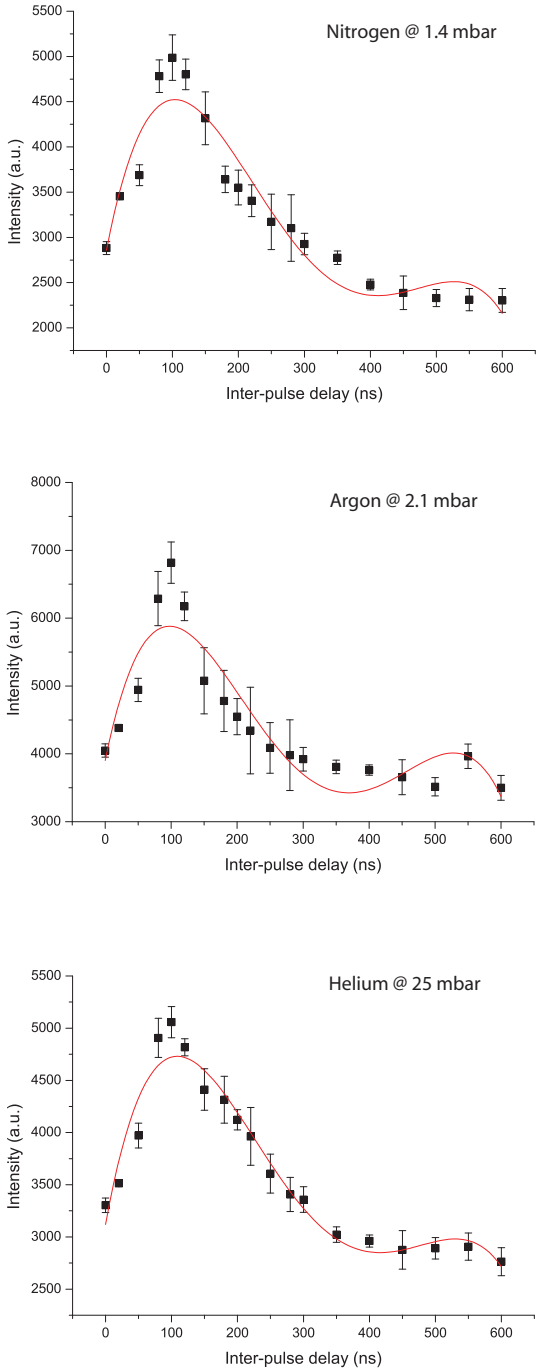

Figure 7.2: Trends in the C^{2+} 97.7 nm line intensity dependence on the inter-pulse delay time in the range of 0 - 600 ns. 4th polynomial fits were applied to the profiles for nitrogen at 1.0 mbar, argon at 2.1 mbar and helium at 25 mbar, corresponding to figure 7.1.

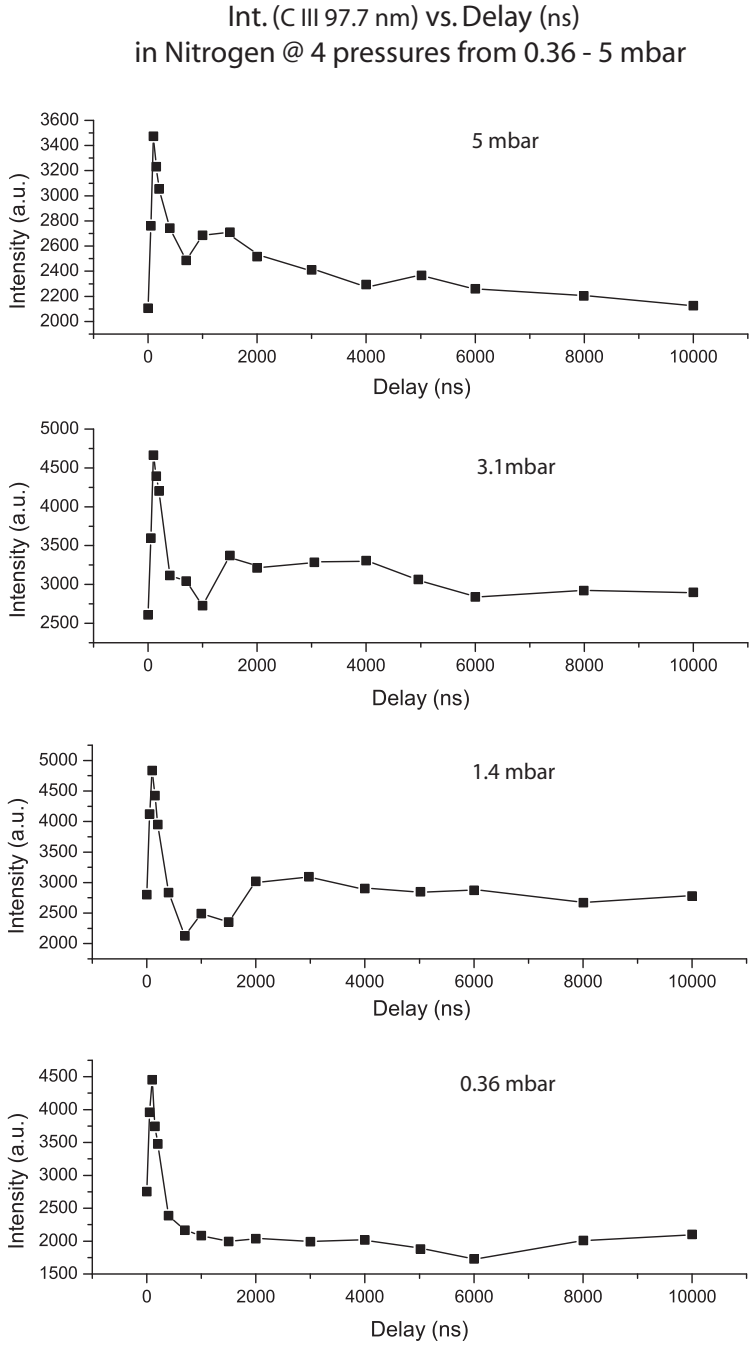

Figure 7.3: C^{2+} 97.7 nm line intensity dependence on inter-pulse delay time in nitrogen at several pressures. Spectron laser (1064 nm, 15 ns, 200 mJ) and Surelite laser (1064 nm, 6 ns, 665 mJ) in dual-pulse collinear reheating mode.

From top to bottom, the four curves range from higher pressures to lower pressures. Starting from the lowest pressure 0.36 mbar, the first intensity peak is clearly shown on the curve but there is no sign of any further intensity revival. The next one is the intensity dependence on the inter-pulse delay at 1.4 mbar. The first intensity peak is again clearly shown at 100 ns delay. Compared to the case at 0.36 mbar, there is a clear intensity increase from 1 to 2 μs. Thereafter the intensity remains quite stable with a slight decline. At the higher pressure of 3.1 mbar, the plateau becomes a little higher than the one at 1.4 mbar, with a clearer decline after 6 μs. The top graph in figure 7.3 is the intensity vs. delay plot at 5 mbar in nitrogen where absorption of VUV emission may now apply (section 5.4). The plateau is even more evident and the intensity decline is faster than the lower pressure cases. These four graphs of intensity vs. delay plots indicate that the higher the nitrogen pressure, the more evident the plateau area.

Next we have examined the effect of inter-pulse delay in argon and in helium where absorption is not a factor. The intensity vs. delay plots in helium from 2 - 150 mbar are shown in figure 7.4 and the plots in argon from 0.2 - 9.5 mbar are shown in figure 7.5. The pressure range selected for each gas was different for the same reasons as given in the section 5.4.1, i.e., VUV absorption in nitrogen, the heightened level of VUV background continuum emission observed in argon while a relatively low heat capacity ratio of helium resulting in a low signal gain. The reason for the pressure range selected for each gas was to ensure the resolution of the spectrum and to limit the background to within a reasonable level.

7.4.2 Inter-pulse delay in helium

Figure 7.4 shows the inter-pulse delay effect in helium at four different pressures. The "plateau after peak" phenomenon is less obvious compared to that in nitrogen. Although not a dramatic feature, one can still see the second plateau at 50 mbar and 150 mbar (top two graphs in figure 7.4). The intensity revival is completely invisible at 2 mbar, it begins to appear at 25 mbar, becomes clearer at 50 mbar and is clearly present at 150 mbar. This again indicates that the "plateau" is more likely to be associated with an intensity revival at higher gas pressures.

7.4.3 Inter-pulse delay in argon

Figure 7.5 shows the intensity vs. delay plots in argon at four different pressures. The 100 ns peak is again evident at all four pressures in argon. The plateau is found at all pressures above 1.1 mbar. Again it is shown that the higher the argon

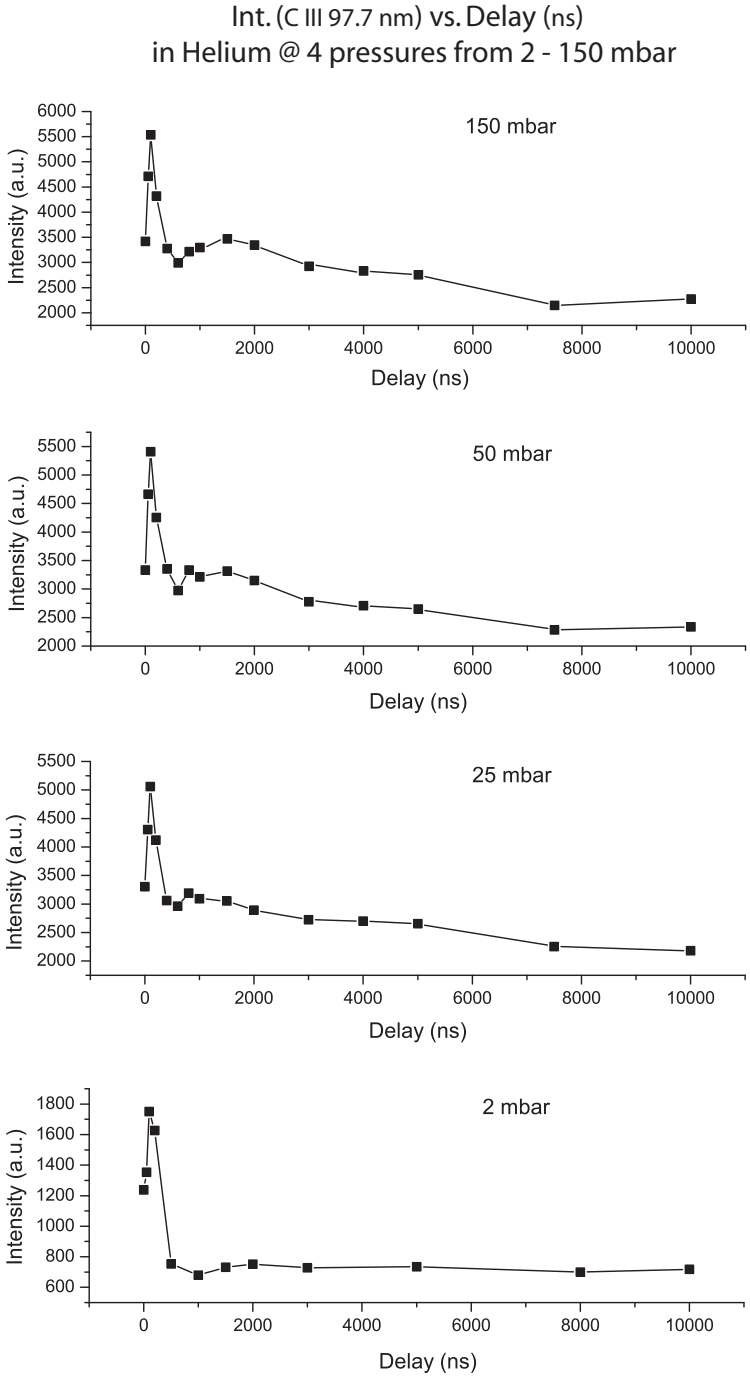

Figure 7.4: C^{2+} 97.7 nm line intensity dependence on inter-pulse delay time in helium at several pressures. Spectron laser (1064 nm, 15 ns, 200 mJ) and Surelite laser (1064 nm, 6 ns, 665 mJ) in dual-pulse collinear reheating mode.

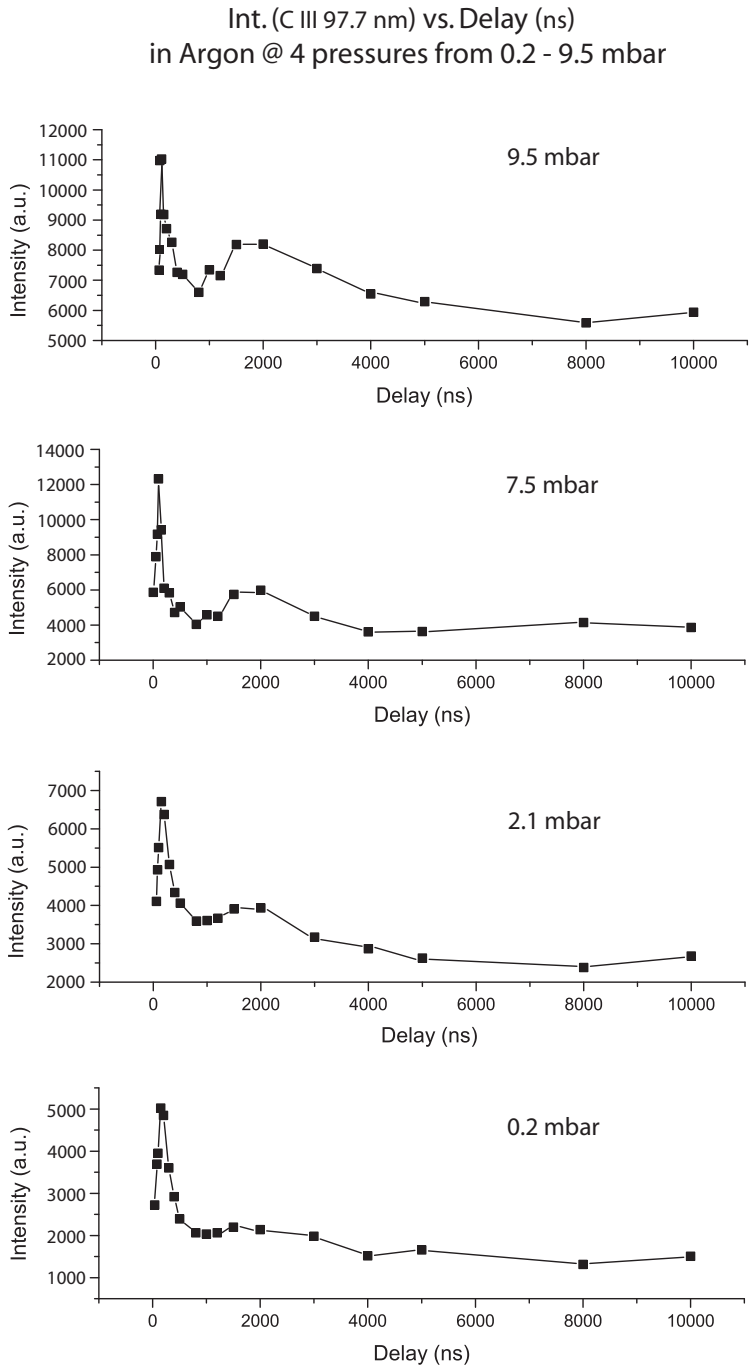

Figure 7.5: C^{2+} 97.7 nm line intensity dependence on inter-pulse delay time in argon at several pressures. Spectron laser (1064 nm, 15 ns, 200 mJ) and Surelite laser (1064 nm, 6 ns, 665 mJ) in dual-pulse collinear reheating mode.

pressure, the clearer the plateau is shown on the curve. The intensity of the first point on each curve represents the case of overlapping pulses with 0 time delay. The intensity value of the first point increases with the pressure, which agrees with the emission intensity trend in argon (section 5.4).

To examine the variation in the 100 ns peak and the plateau, the ratio of the 100 ns peak intensity to the 0 ns intensity peak given by $R_{peak} = I_{100ns}/I_{0ns}$, and the ratio of the plateau (taking the intensity value at Δt = 2 μs) to the 0 ns intensity $R_{plateau} = I_{2\mu s}/I_{0ns}$ were extracted from the data and plotted in figure 7.6.

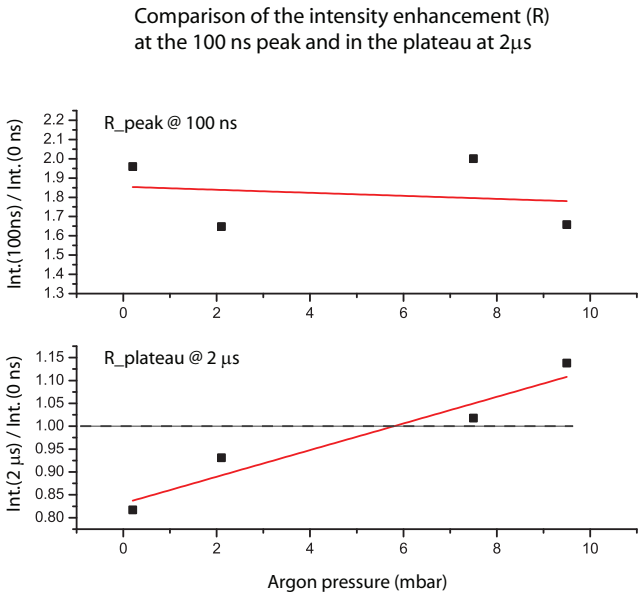

Figure 7.6: Comparison of the intensity enhancement vs. pressure at the 100 ns peak and at the 2 μs plateau. The intensity enhancement is indicated by the relative intensity of 100 ns peak to 0 ns starting point ($R_{peak} = I_{100ns}/I_{0ns}$) and the relative intensity of the plateau to the starting point ($R_{plateau} = I_{2\mu s}/I_{0ns}$), corresponding to the intensities recorded in figure 7.5. Spectron laser (1064 nm, 15 ns, 200 mJ) and Surelite laser (1064 nm, 6 ns, 665 mJ) in dual-pulse collinear reheating mode.

Four data points were included in each plot corresponding to the intensity curves at the four different argon pressures shown in figure 7.5. The general trend of each ratio is indicated by a linear fit to the four data points. In the top panel of figure 7.6, R_{peak} stays flat and the data points are evenly distributed around the average level, only a slight decline is shown in the general trend. The stable R_{peak} suggests that the 100 ns peak intensity variation is synchronized with the intensity at 0 time delay. This variation corresponds to the emission behavior we have investigated in section 5.4. However the $R_{plateau}$ in the bottom panel of figure 7.6

shows an increase with argon pressure. The $R_{plateau}$ values start at about 0.8, then becomes greater than 1 when the argon pressure is above a certain level (estimated to be between 3 and 5 mbar from the plot). It is implied that the higher the pressure, the faster the plateau intensity increases. When the pressure goes above a certain level, the plateau intensity becomes higher than the starting point level and becomes an intensity enhancement. Comparing the two intensity ratios, we have seen that the gas pressure does not affect the 100 ns peak greatly but has a noticeable influence on the plateau. These observations show that the "plateau" on the curve is genuinely an intensity revival and it is related to the gas pressure.

The next question is how does the gas pressure affect the intensity enhancement in the plateau area and are there any other factors involved in the enhancement of the plateau area? The next section: *What made the plateau appear?* will provide more detailed discussion on the potential factors.

7.5 What made the plateau appear?

So far, we are certain that there is an intensity revival which corresponds to the plateau observed at higher gas pressures. So we have come to the second question raised at the beginning of this section, what made the plateau appear? In other words, what are the underlying causes for the intensity revival at long time delays? Gas pressure is one factor which was directly observed on the intensity vs. delay curves. The gas absorption of VUV light could not be neglected in some cases either (e.g., nitrogen). Another possible factor is the breakdown in each gas which may result in an intense interaction between charged gas particles and the plasma particles. Also we would like to examine if the inter-pulse delay effect applies to one or two particular trace elements in the matrix or does it apply to all the emitting elements in the plasma.

7.5.1 Gas pressure vs. plateau: a case study in argon

We have noticed that the plateau appeared in ambient gases at higher pressure and we have briefly determined the "pressure threshold" above which the plateau became noticable in argon (section 7.4). Here we will give an insight into how the plateau is related to the ambient gas pressure by a case study in argon. As introduced in the discussion of the inter-pulse delay effect in argon in section 7.4.3,

the intensity ratio R is defined as:

$$R = \frac{I_{plateau}}{I_{initial}} = \frac{I_{\Delta t=2\mu s}}{I_{\Delta t=0}} \tag{7.1}$$

The intensity ratio of the plateau to the initial point in argon is then denoted as R_{argon}. The plot of intensity ratio R_{argon} vs. argon pressure is shown in figure 7.7. It corresponds to the raw plot (only 4 data points) of R_{argon} vs. argon pressure in figure 7.6 but with a more detailed scan from 0.1 mbar to 10 mbar. It is seen that after about 5 mbar, R_{argon} becomes greater than unity, i.e., the plateau is a second intensity enhancement compared to the initial point (the first one was at the 100 ns peak). As the pressure increases, the increase in the value of R_{argon} continues but slows down slightly. The trend of R_{argon} within the first 10 mbar could be described by a quadratic fit indicated by the solid red curve on the graph. It is implied that R_{argon} can be increased further by increasing argon pressure, however the spectra recorded at high pressures are dominated by continuum emission (section 5.4.1) and so the recorded intensity would no longer be beneficial to our study as that would reduce the effective signal to background ratio (SBR).

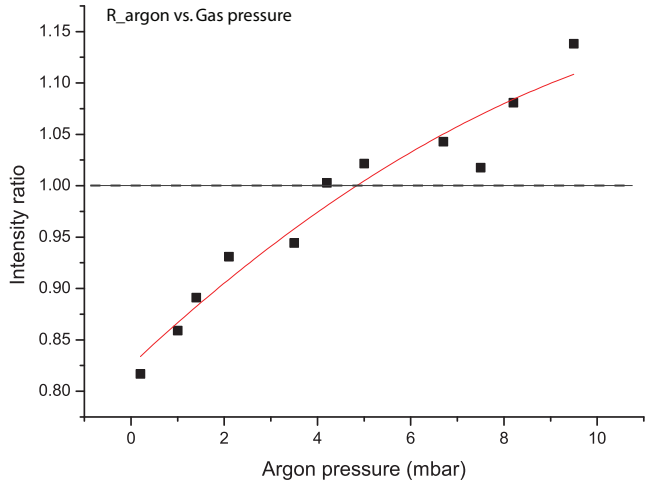

Figure 7.7: The intensity ratio of the plateau to the initial point (simultaneous pulses) vs. argon pressure. Spectron laser (1064 nm, 15 ns, 200 mJ) and Surelite laser (1064 nm, 6 ns, 665 mJ) in dual-pulse collinear reheating mode. Other settings were the same as in figure 7.5.

At higher pressures the plasma expansion is buffered more effectively and so the chances of the plasma interacting with another collisional source is increased. This collisional source could be the second laser pulse, the ambient gas particles or a second plasma produced by the second laser pulse. The interaction between the

plasma and the second laser pulse was already considered in the first enhancement (at 100 ns delay), hence the new collisional source could be the ambient gas breaking down caused by the second pulse or a second plasma produced by the second pulse. These potential factors will be discussed later in this section.

7.5.2 Gas pressure vs. plateau: nitrogen and helium

Because of the strong VUV light absorption by nitrogen, the inter-pulse delay effect was not as clearly present in nitrogen as in argon (figure 7.3). Helium as a light gas did not provide a favorable environment for inter-pulse delay effect either (figure 7.4). Nevertheless, we still undertook an investigation of the inter-pulse delay vs. gas pressure in the case of nitrogen and helium in the following.

The intensity ratio of the plateau at about 2 μs delay to the initial point at 0 delay is shown in figure 7.8. The curve of intensity ratio vs. nitrogen pressure is seemingly broken into two parts. From 0.36 mbar to about 3 mbar, $R_{nitrogen}$ increases to the unity at about 1.2 mbar, the increase continues till 3 mbar. When the nitrogen pressure is above 3 mbar, the increase in the value of $R_{nitrogen}$ increases again and shows a linear increase with the pressure. However this was mostly due to the strong absorption of VUV light by nitrogen resulting in a reduction of the intensity at the initial point (figure 7.3). The actual height of the plateau did not increase as suggested by $R_{nitrogen}$.

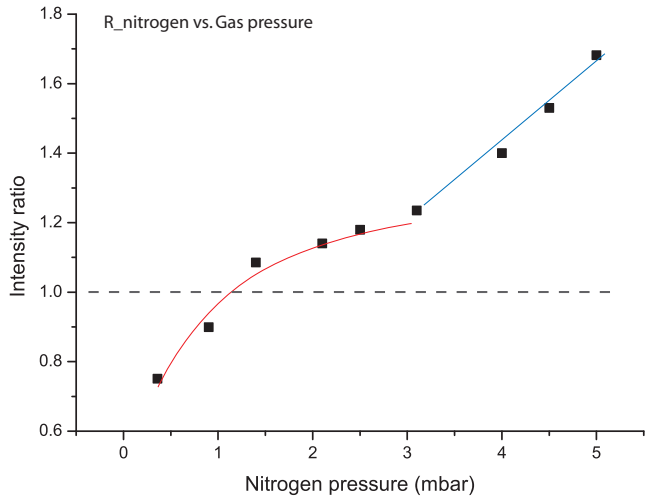

Figure 7.8: The intensity ratio of the plateau to the initial point (simultaneous pulses) vs. nitrogen pressure. Spectron laser (1064 nm, 15 ns, 200 mJ) and Surelite laser (1064 nm, 6 ns, 665 mJ) in dual-pulse collinear reheating mode. Other settings were the same as in figure 7.3.

The R_{helium} vs. helium pressure is presented in figure 7.9. There is a fast increase in R_{helium} with pressure in the first 50 mbar but the gain flattens once R_{helium} is above unity. It is implied that helium is not as good a buffer gas as nitrogen or argon in the current work.

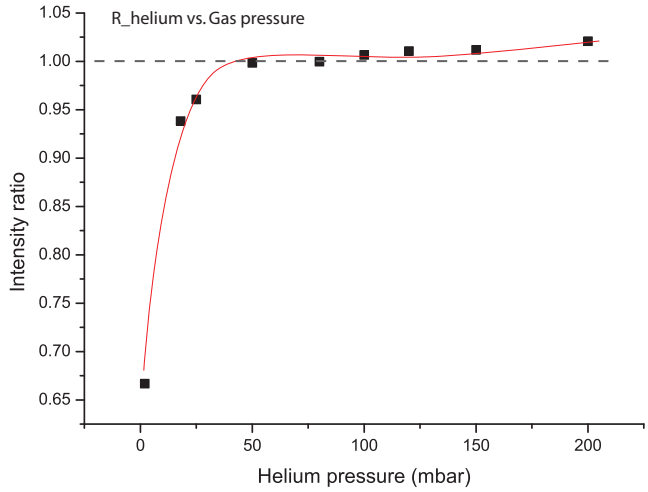

Figure 7.9: The intensity ratio of the plateau to the initial point (simultaneous pulses) vs. helium pressure. Spectron laser (1064 nm, 15 ns, 200 mJ) and Surelite laser (1064 nm, 6 ns, 665 mJ) in dual-pulse collinear reheating mode. Other settings were the same as in figure 7.4.

7.5.3 Ambient gas only experiments

In the case study of argon (section 7.5.1), the ambient gas breakdown was raised as a potential factor for the inter-pulse delay effect. To examine the possibility of gas breakdown, an additional experiment was carried out to test the source of gas emission lines (N, Ar) in the spectra. The experimental setting was the same as the dual-pulse set-up except the sample and sample holder were removed from the sample chamber. When the laser was fired into the chamber it was therefore actually fired into a chamber of gas. The spectrum was recorded the same way as the other experiments. A pressure range of 0.1 mbar to 10 mbar was scanned for nitrogen and argon, pressures from 1 mbar to 50 mbar were tested for helium. None of the recordings showed a clear spectrum nor was a breakdown spark observed in the chamber. The results indicated that the ambient gas is not ionized by the laser pulses. Of course the gas breakdown could be seeded by the plasma formed on the surface of the metal target. However, we were not able to observe any emission lines from ions of the ambient gas with the metal target present. We believe that

this is the result of the low number density of emitting gas ions and not due to their absence. Hence we were not able to disentangle the effects of any gaseous plasma on the expansion dynamics of the metal plasma via this experiment.

7.5.4 Inter-pulse delay effect is independent of emitting elements

The relationship between the inter-pulse delay effect and the emitting elements was examined by recording the intensity dependence on the inter-pulse delay time for four different spectral lines. The results in nitrogen at 0.91 mbar are shown in figure 7.10. As one can see, the four intensity curves are fairly similar and there is an "intensity revival" between 500 ns and 2000 ns observed on each line intensity trend. The same four lines were examined also in argon at 1.3 mbar and helium at 200 mbar, the details are provided in appendix D. The intensity dependence on the inter-pulse delay exhibited for the four different lines in three types of gases shows that the universal existence of the "plateau after peak" among emitting elements. Thus the "plateau after peak" phenomenon is independent of the emitting elements.

The observations so far in ambient gases and in vacuum can be summarized as follows:

The peak intensity was achieved between 100 to 200 ns in all cases, while the "intensity revival" from 1 - 6 μs was only found at relatively higher gas pressures. Thus we have limited the causes of the "plateau after peak" phenomenon to those directly related to the pulse-plasma or plasma-plasma interactions such as gas pressure and second pulse re-ablating the sample. Thus the reason of "plateau after peak" may lie in the plasma expanding mechanism, specifically the collisions between plasma and a second plasma. The increased collision rate may be triggered by the coupling of the buffered first plasma and the fast expanding second plasma.

7.6 Could the plateau be enhanced more significantly than the first peak?

In our observations, the first peak, corresponding to the reheating pulse-sample coupling, was narrow, while the second plateau was relatively wider and stable. So we approach the third question, could the enhancement in the second phase be greater than in the first phase? If so, there would be a wider range of inter-pulse delay separations at which a more stable signal enhancement may be achieved.

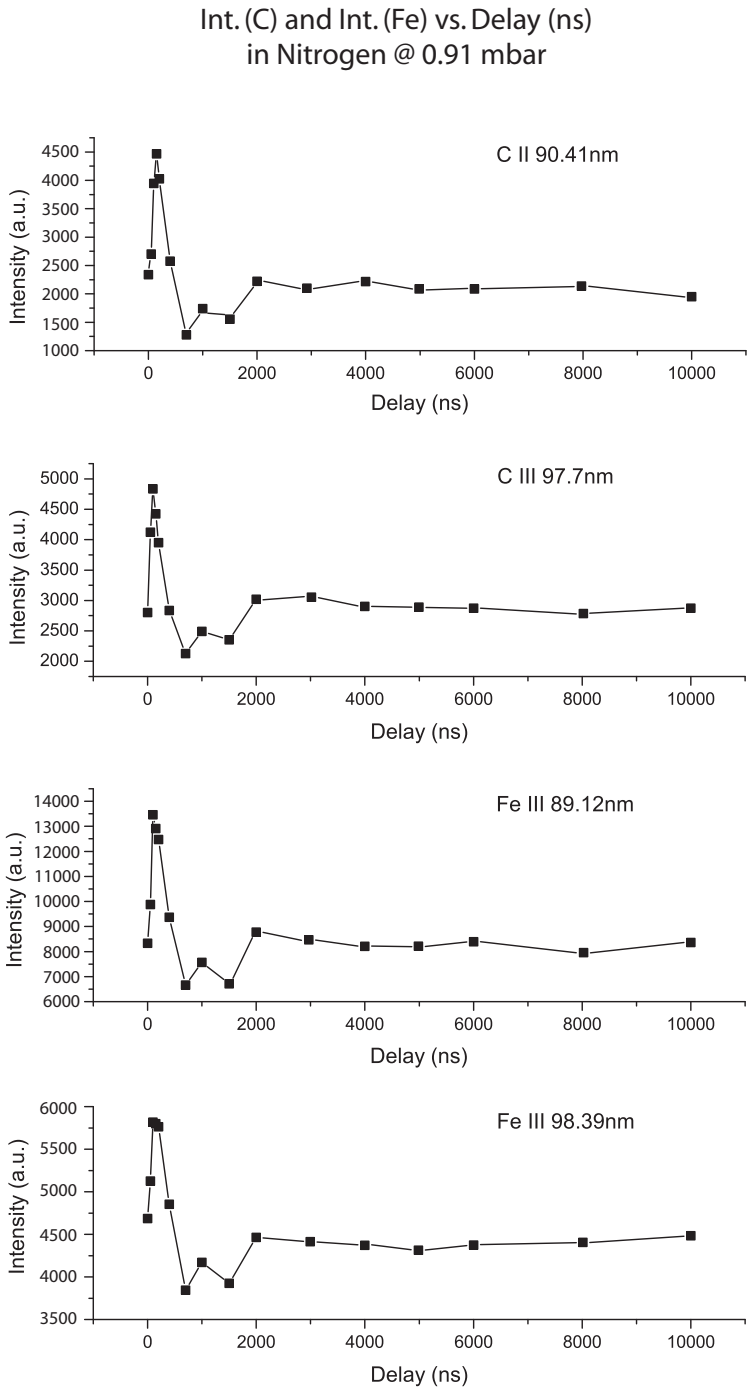

Figure 7.10: Intensity dependence on inter-pulse delay time in nitrogen at 0.91 mbar. Spectron laser (1064 nm, 15 ns, 200 mJ) and Surelite laser (1064 nm, 6 ns, 665 mJ) in dual-pulse collinear reheating mode.

Our results have shown that the second plateau becomes more evident when the pressure of ambient gas is increased. However the VUV emission is sensitive to ambient gases because of absorption, it was therefore difficult, in our case, to examine the VUV emission in a good buffering gas (such as nitrogen) at a high pressure. So the possibility of enhancing the plateau more significantly than the 100 ns peak was very low in our case. It would be difficult to record the VUV emission signal at high pressures so the inter-pulse delay effect study in the current work was limited to low pressure ambient gases.

7.7 Summary

The inter-pulse delay time was optimized in several ambient gases after the optimization in vacuum (section 5.3.3). There is a common intensity peak at 100 ns in vacuum and in gases at all pressures below 10 mbar. When the inter-pulse delay time span is extended to over 10 μs, an intensity revival between 1 to 6 μs in ambient gases above certain pressures (1 mbar for nitrogen, 2 mbar for argon, 25 mbar for helium) is observed. Compared to the 100 ns intensity peak, the second intensity revival is rather flat and wide and so it is referred to an intensity plateau. This chapter was mainly focused on the interesting observations of the intensity plateau. Three basic questions were raised about the plateau and the discussions can be summarized as: (a) it is a genuine intensity revival, i.e., the emission is enhanced for a second time; (b) the second intensity enhancement is observable when the condition of a proper ambient gas at an appropriate pressure is achieved; (c) the second intensity enhancement is not as significant as the first one and it is difficult in the current work to enhance it to be better than the first intensity peak.

Chapter 8

Emission Enhancement Mechanisms in Dual-Pulse LIBS

The inter-pulse delay effect discussed in chapter 7 has revealed two emission enhancements. One is a sharp intensity peak at 100 ns delay and the other is a wider plateau region of intensity revival in the μs range between 1 to 6 μs. These enhancements at different inter-pulse delays suggest two different enhancement mechanisms, the second pulse interacts with the existing laser induced plasma (LIP) system in its different phases. This chapter provides an insight into the mechanisms of the emission enhancement in dual-pulse LIBS in our observations. Some suggestions regarding the dual-pulse laser ablation mechanisms in general are also provided.

8.1 Introduction to the expansion mechanics of laser induced plasma

The previous chapter focused on the effect of the inter-pulse delay on dual-pulse LIBS and provided a preliminary discussion of the two clearly defined signal enhancement in the delay range of 0 to 10 μs in ambient gases. Three questions about the second signal enhancement have been asked and addressed. A series of examinations led us to believe that there was a genuine second intensity revival in the μs delay range leading to a broad plateau region on the intensity vs. inter-pulse delay curves. This second intensity revival (i.e., the plateau) only occurred in ambient gases and its magnitude was proportional to gas pressure within an appropriate range (0 - 10 mbar) for VUV emission.

While the first intensity peak corresponding to laser-plasma coupling is essentially independent of the ambient gas type or pressure, the second intensity revival suggests a different enhancement mechanism. The mechanics of the interaction between the second pulse and the existing (first) "single-pulse-like" laser induced plasma (LIP) system is highly dependent on two factors. One is the expansion dynamics of the first LIP, the other is the inter-pulse delay time, which means at what stage of the first LIP expansion does the second pulse arrive at the plasma-target system?

In section 4.3, which focused on the time integrated space resolved emission behavior of the LIP, the VUV intensity decreased with the distance from the target surface while the signal-to-background ratio (SBR) increased at first and subsequently saturated at further distance. The intensity and SBR distributions indicate the plasma evolution in a space-resolved (SR) but time-integrated (TI) way. Figure 4.2 (section 4.2) showed schematically the method of detection. At the beginning there is a small dense plasma dominated by continuum emission, as it expands to 4 mm (usually takes about 40 ns) it starts to emit a characteristic spectrum. The line intensity is maximized while the background continuum level diminishes as the plasma cools down. At greater distances the plasma will be on average more dilute and the emission intensity will consequently be weaker.

Moreover, with time-resolved (TR) systems, there are many imaging works in the LIBS literature providing direct pictures of the expansion mechanisms of single-pulse LIP in vacuum and in gases. Harilal et al. provided an imaging study of single-pulse laser produced plasma expansion in vacuum and in ambient gas [76]. The time evolution of an aluminum plasma expanding into vacuum (1×10^{-6} Torr) is shown in figure 8.1. Over a time span of 300 ns, 8 typical ICCD images were

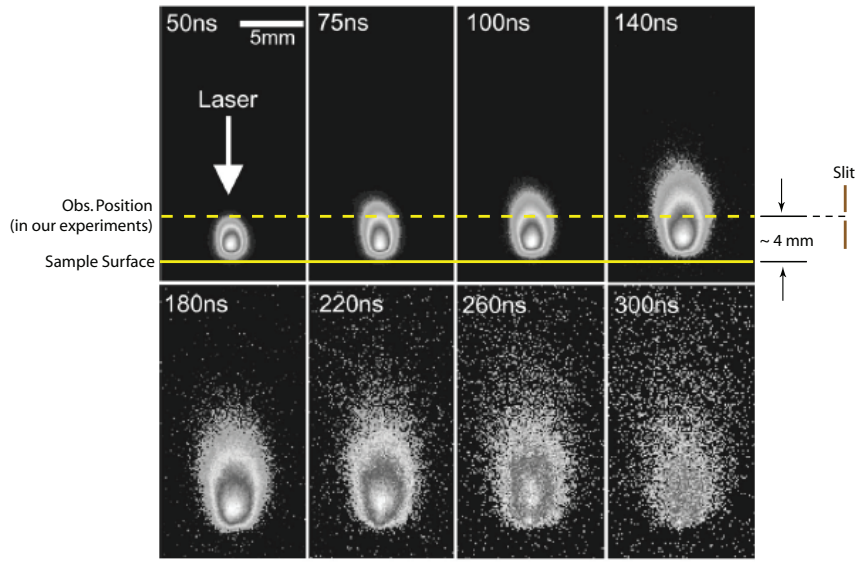

Figure 8.1: Imaging study of single-pulse produced aluminum plasma expanding in a background of the pressure of 1×10^{-6} Torr, by Harilal et al. [76].

taken and arranged in the time sequence from top left to bottom right. Each image represents the spectrally integrated plume emission in the region 350 - 900 nm that is due to the emission from the excited states of various species. In each image, the laser is incident from the top in the direction indicated by the arrow in the first image. The aluminum sample is at the bottom perpendicular to the laser beam direction, indicated by the solid line in figure 8.1). The bright area against the dark background is the recorded visible emission from the plasma.

As can be seen from these images, the development of a plasma in vacuum is quite straight forward. In the initial stage, the laser beam interacts with the sample and forms a dense plasma. Following this, the plasma expands into a vacuum environment with little or no interaction with ultra-low density residual background at the base pressure of 10^{-6} Torr. At later stages (260 ns, 300 ns) the plasma cools down and eventually decays. This is a typical free expansion.

It is worth noting that it takes 40 ns or so for the plasma to expand to 4 mm where the observing position (section 4.3) is (indicated by the dash line in figure 8.1). The slit is aligned to record the emission from the plasma at 4 mm above the sample surface as shown previously in figure 4.2.

The same aluminum plasma expanding in air at 1.3 Torr ($\approx$ 1.73 mbar) is shown in figure 8.2. Eight images of the plasma plume are shown with time delay increasing from top left to bottom right. As one can see, the plasma is dense and the plume

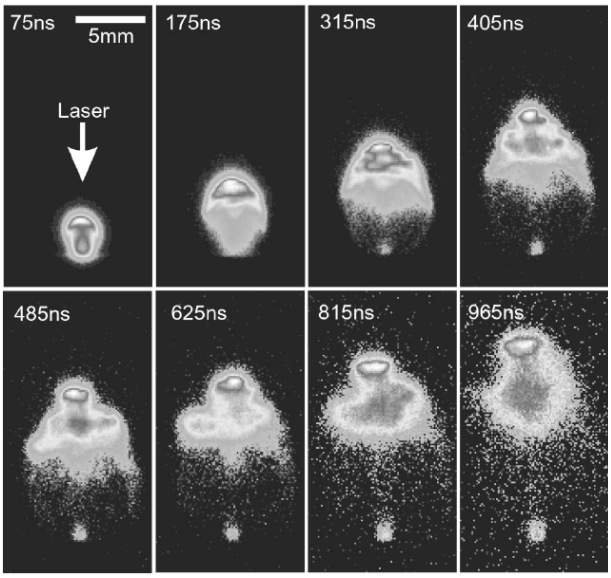

Figure 8.2: Imaging study of single-pulse produced aluminum plasma expanding in air at 1.3 Torr by Harilal et al. [76].

is again small in volume in the early stages (75 ns in the first image) which is very similar to the case in vacuum. However when the plasma expands further into the ambient gas, it is buffered by the gas. The plasma front, which is in direct contact with the ambient gas, interacts intensely with the ambient gas. The increased collision rate between plasma particles and the gas particles results in an increase in the intensity of radiation as plasma expansion or kinetic energy is converted into excitation energy. This interaction zone moves forward as the plasma expands. Also, the time evolution of the plasma plume in an ambient gas at 1.3 Torr in figure 8.2 (more than 1 μs) is much longer than that in vacuum (just over 300 ns).

Different from the free expansion in a vacuum or low background pressures, the plume behavior is characterized by strong interpenetration of the laser plasma and the ambient low-density gas when the ambient gas pressure increases. In general, an increase in the background pressure results in several effects including (a) an increase in fluorescence from all species due to enhanced collisions on the expansion front and subsequent inter-plume collisions, (b) slowing of the plume propagation resulting in the spatial confinement of the plasma, and (c) the formation of the shock front.

8.2 The phased enhancement

On the inter-pulse delay time scale, we can roughly divide the entire plasma evolution process into three phases:

From 0 time delay to 1 μs, within which range the 100 ns peak was shown, is designated as the first phase, *Phase One*. From 1 μs to 10 μs, which range contains the second broad peak or the plateau in some cases with ambient gases, is designated as the second phase, *Phase Two*. From a delay of 10 μs up to potentially 100 ms when the laser are triggered again to produce the next pair of pulses, where no significant intensity variation in intensity and/or SBR is observed is termed as the third phase, *Phase Three*.

While the line emission at 97.7 nm was enhanced in the first and in the second phase respectively, each gain or enhancement had its own corresponding mechanism. We use the term "phased enhancement" in this context. Based on the above observations and discussions, the process of the phased enhancement is proposed to be as follows:

1. Phase One (0 - 1 μs).
   When the second pulse arrives at the very early stage (0 - 50 ns) of the initial plasma, the plasma density is very high and although some of the laser energy is absorbed much is scattered out of the plasma and so the degree of reheating by the second pulse is not very high. When the second pulse arrives between 50 and 100 ns, the reheating process is clearly more effective as witnessed by the increase in line emission. In this case we propose the that plasma density at the 4 mm observing position is optimal for inverse bremsstrahlung absorption and so the greatest degree of reheating and plasma emission occurs consistent with attaining a plasma temperature of a few to 10 eV or so, yielding optimal excited C^{2+} ions in the plasma. The signal enhancement lasts a few tens of nanoseconds and the intensity reaches a peak at 100 ns. Subsequently, the plasma expands so that the density drops below the optimum value for IB absorption in the region of 4 mm from the target surface and so the VUV emission intensity wanes.

2. Phase Two (1 μs - 10 μs).
   In the next stage of the plasma i.e., after 1 μs, as the time delay increases, more and more of the delayed second laser beam can pass through the dilute plasma to reach the target where it can ablate material and form a second plasma. Initially the second plasma expands rapidly, while the preformed

plasma is buffered by the surrounding relatively heavy gas (i.e. nitrogen or argon compare to helium or vacuum). The fast expanding second plasma soon catches up and collides with the buffered initial plasma resulting in a second intensity enhancement. According to a time-resolved study of overall plume emission in ambience by Harilal et al. [76], for air at 1.3 Torr (1.73 mbar), the plasma plume expands rapidly at the early stage from 0 to ca. 150 ns, slows down from 200 ns to 1 μs, and thereafter remains stable where there is no more reheating pulse or other source of post-excitation. It matches our theory that the fast expanding second plasma in its early phase can interact with the initial plasma in its stable phase (i.e., after 1 μs).

3. Phase Three (after 10 μs).
   In this phase, the first plasma decays before the second plasma is able to interact with it. It is equivalent to two distinct laser plasmas and thus no intensity enhancement is expected in this phase.

An illustration of these processes based on the above discussion is presented schematically in figure 8.3. As can be seen, the laser-plasma interaction is the dominant process in the first phase. With longer inter-pulse delay times, the second plasma is already formed and so the plasma-plasma interaction is the dominant driver in the second phase. When the second pulse is well delayed, the first plasma decays before the second plasma expands to interact with it. It is equivalent to the formation of distinct plasmas by two separated pulses.

As also shown in figure 8.3, the signal gains arising out of the first and second phases are due to different enhancement mechanisms. The first enhancement during the reheating by the second pulse, cf. panel (ii) in figure 8.3. The second enhancement occurs when the second plasma expanded rapidly and interacts with the first plasma which was buffered by the ambient gas. It is effectively a plasma-plasma coupling process, cf. panel (iv) in figure 8.3.

Based on the theory of "phased enhancement", the process of dual-pulse excitation in ambient gas can be summarized as:

The dual-pulse laser induced plasma process can be described in three phases. Although at very short time delays much the second laser pulse is reflected by the initial dense plasma, as the inter-pulse delay is increased, more and more of the reheating pulse is absorbed by the expanding plasma leading to a distinct and measurable signal enhancement. Later on the second laser pulse can penetrate the dilute plasma, ablate material from the target and form a second plasma. At certain inter-pulse delays, the second plasma expands and collides with the first plasma

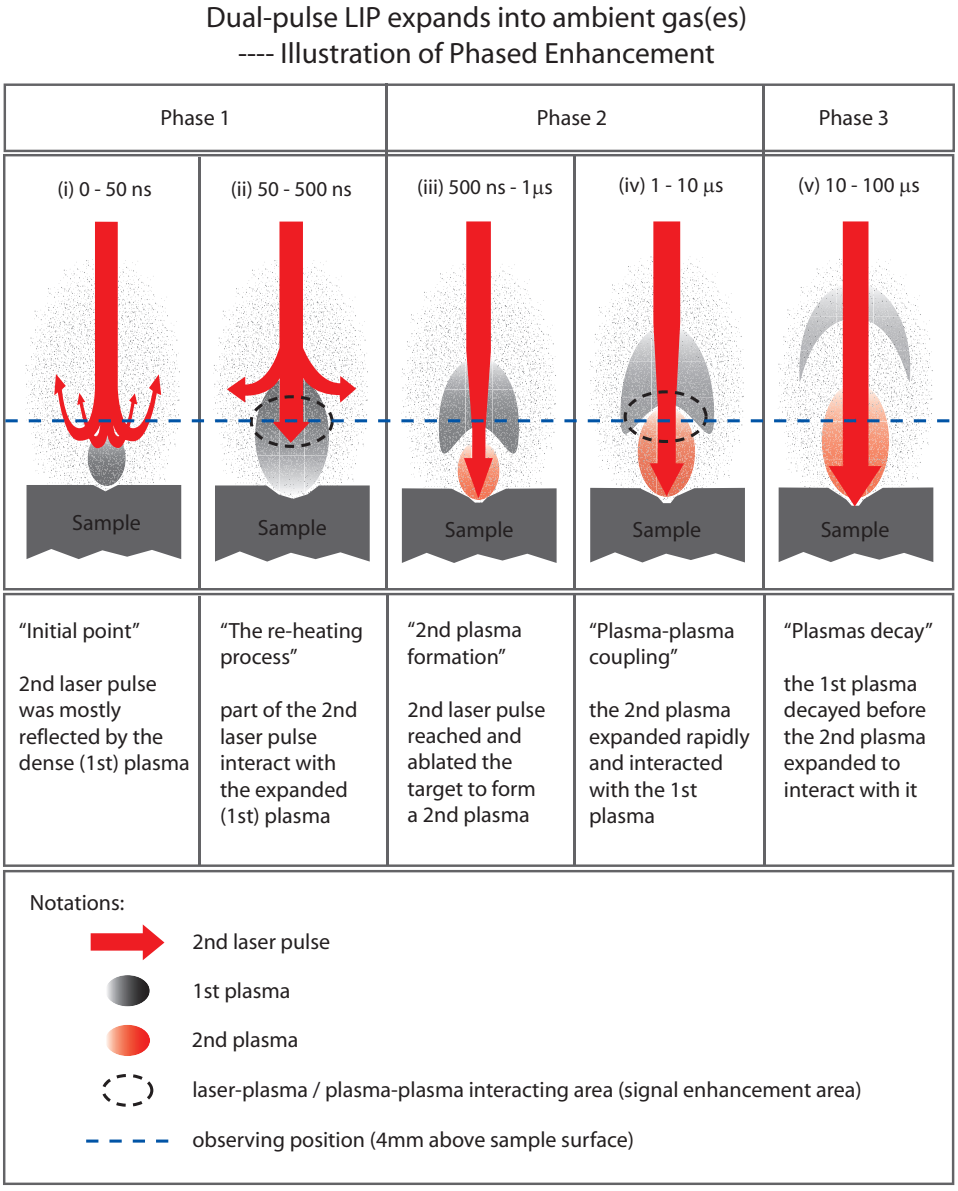

Figure 8.3: Schematic illustration of the phased enhancement during the dual-pulse excitation process.

surrounding it, providing another signal enhancement by the plasma-plasma coupling. Finally at even longer delay times, the two pulses act as two separated pulses yielding two individual plasma plumes and no more enhancement is expected.

8.3 A survey of inter-pulse delay effect on DP-LIBS in the UV/IR compared with DP-LIBS in the VUV

Table 8.1 lists a number of studies on the inter-pulse delay effect and dual-pulse LIBS. Most of these works were carried out at atmospheric pressure (1 atm) and the optimal inter-pulse delay times were usually between 10μs and 30μs. A small number of these works reported an optimal inter-pulse time below 1μs under certain experimental conditions. Some of the works have observed a hint of two intensity enhancement regions but few of them have reported or discussed this phenomenon. The works in the top part of table 8.1 observed one intensity peak while the works listed in the bottom part (separated by the double line) of the table have some evidence for the multi-phased enhancement observed on the C^{2+} 97.7 nm line in VUV DP-LIBS.

It is important to note that in these previous works, the method of detection was different. In those cases time-resolved detection was used and the emission was recorded with various gate time and gate width as indicated in table 8.1. Furthermore, as remarked earlier, many of the experiments were carried out in air at atmospheric pressure while the current work was carried out at much lower pressures. These factors make it difficult to compare our work to that reported in the literature, nevertheless these studies of inter-pulse delay effect are instructive.

In Gautier's work in 2005 [71], a rather steady signal enhancement was observed as the time delay to the second or the reheating laser pulse was swept from 5 μs to 12.5 μs, although a small "first phase enhancement" was shown on the Mg^{+} intensity curve in the range of 0 - 0.5 μs. The first intensity increase was not as significant as the enhancement in the later period (5 μs - 12.5 μs) thus it was not discussed in the overall enhancement process. This may be due to the fact that Gautier's work was carried out in air at atmospheric pressure which was a much higher pressure gaseous environment (1 atm $\approx$ 1000 mbar) than the ambient gas used in the present VUV work ($\leq$ 10 mbar). The plasma expansion was strongly buffered by the air and so for the first couple of μs one may speculate that the electron density in the plasma was kept high and the second pulse would be mostly screened out, hence any enhancement would be limited.

Publication Author,ref.	Element	λ range	Environment	Pulse cfg[*1]	t_d gate time	t_w gate width	Optimal Δt
Ahmed,[80]	Al	UV	air	C	3ms	2ms	25μs
Cristoforetti,[75]	Cu	UV-VIS	air[*2]	C	0.1,0.3μs	0.7,2μs	1-2μs
Gautier,[81]	multi-metal	UV	air	C	1μs	30μs	0.5-2μs
St-Onge,[82]	Al,Si	UV-NIR	air	C	2μs	0.5μs	100ns
Gautier,[83]	multi-metal	UV	air	O	2μs	30μs	15-30μs
Santagata,[84]	Cu,Zn	UV	air	O[*4]	0.5μs	5μs	10μs
Stratis,[85]	Fe	UV-VIS	air	O	2μs	0.5μs	2.5-25μs
Hohreiter,[72]	Mg,Si	UV	air	O	2μs	2μs	1-5,20μs
Sattmann,[70]	Fe	UV-VIS	air	C[*3]	-	1s	1,20μs
Gautier,[71]	Mg	UV	air	C	4μs	3μs,500ns	0-0.5,5-12.5μs
Cristoforetti,[86]	Zn,Cu,O	VIS	air[*2]	C	0.7μs	0.4μs	0-2,2-10μs
Cremers,[87]	O	VIS	water	C	60ns-5μs	$<$1μs	multi

Table 8.1: Summary of recent studies on inter-pulse delay time. [*1] C - collinear; O - orthogonal; [*2] air pressure vary from 0 to 1atm; [*3] dual-pulse is performed by one nanosecond laser, other cases are two lasers [*4] femtosecond laser is employed as pre-spark pulse with nanosecond laser as ablation pulse, other conditions are all with nanosecond lasers, other conditions are nanosecond lasers

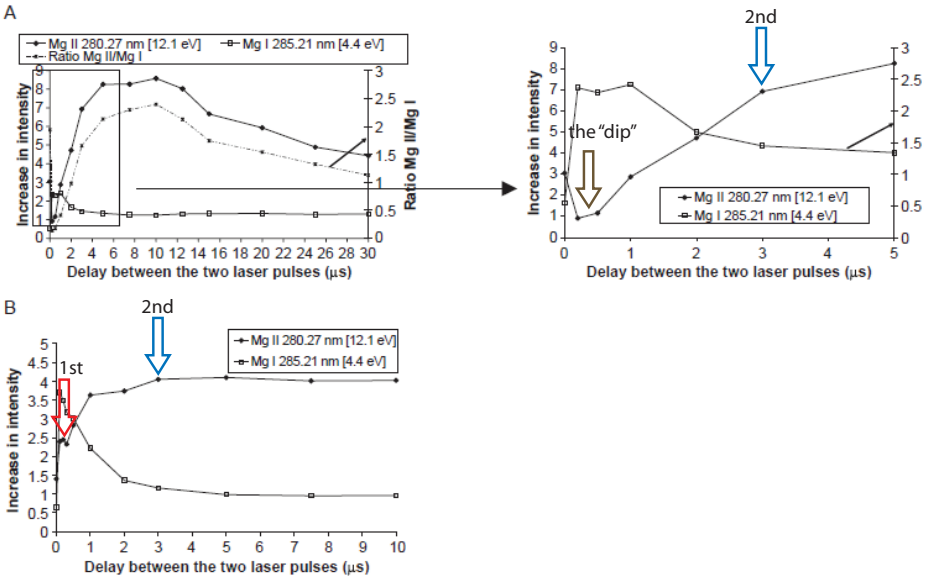

Figure 8.4: Gautier's work in 2005 [71]. Inter-pulse delay effect on Mg neutral line and Mg II line. The reported optimal Δt for Mg I was 0.2 μs and 5 - 12.5 μs for Mg II. However a small "peak" within 1 μs was shown on the Mg II intensity curve.

It was also indicated that due to the higher pressure ambient gas, the plasma lifetime was lengthened and the time scale of plasma interaction with the second pulse was also extended (i.e. from a few μs in our case to 30 μs in Gautier's work). Time scale differences were also found in other works using different experimental settings. Thus the time range for phase one or phase two as we proposed previously should be adjusted to a new time scale in each specific instance. But it doesn't affect the fact that these experiments have all indicated a "two-phase enhancement" process in the dual-pulse excitation. It is the two different mechanisms of the enhancement in each phase that is of the most interest, rather than the time scales of the two phases in each individual experiment.

Later in Gautier's work in 2006 [81] the peak in the 'first phase enhancement' was also shown on neutral Ni and Cr lines with a similar experimental setting of solid metal sample in air. Our results also evidenced that the C^+ line and C^{2+} line had very similar emission behavior (see figure 5.6 and figure 5.4). As in the case of the similarity between C line and Fe line VUV emission behaviors observed in gases (section 5.4.1), the "phased enhancement" was independent of the emission species or the ionization stage of the corresponding charged particles. In the literature, plasma temperature and electron density have been considered to be two main

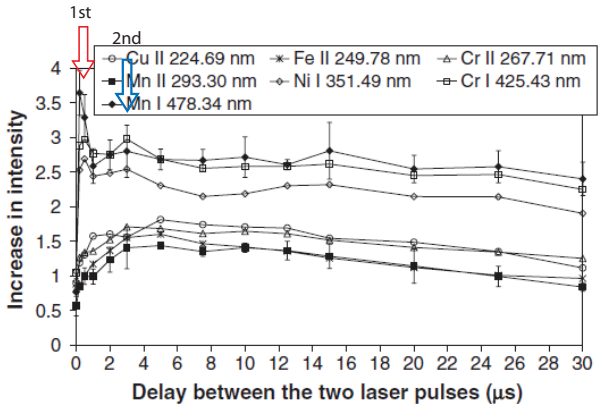

Figure 8.5: Gautier's work in 2006 [81]. Inter-pulse delay effect on several lines from steel sample.

factors related to the dual-pulse enhancement.

Sattmann et al. [70] examined the emission from laser produced plasma formed on a solid steel sample in air. In the collinear DP mode, the intensity of an iron visible line ($I_{Fe532.42nm}$), electron temperature (T_e) and electron density (n_e) were plotted as functions of the inter-pulse separation from 0 to 80 μs. Sattmann showed that the electron temperature T_e increased rapidly from 0 to 5 μs, reached a plateau from 10 μs to 20 μs, and remained steady thereafter. The electron density n_e showed a significant fall between 0 and 5 μs, followed by a sharp increase in the time delay range from 10 μs to 20 μs. It reached a peak which was about 10% higher than the starting point (simultaneous pulses, 0 delay) and stayed at roughly the same level after 20 μs with very little fluctuation. The intensity trend for the iron line ($I_{Fe532.42nm}$) increased rapidly from 0 to 5 μs, decreased a little from 5 μs to 10 μs, grew again from 10 μs to 20 μs and remained steady thereafter so that two distinct intensity peaks at 5 μs and 20 μs could be discerned. The authors pointed out that the line intensity behavior was similar to that of the electron density. This can be briefly explained when we apply the two-phase enhancement proposal to this case. In the early phase (from 0 to 5 μs in Sattmann's case), the hot dense plasma produced by the first pulse had a very high electron density (n_e), and so one can expect that a significant fraction of the second pulse energy was reflected. As time progressed, n_e dropped to a lower level, the re-heating process by the second pulse became more effective as the collision rate over the electron-ion recombination rate increased and so n_e was then significantly increased. When the second pulse came in a later phase, the re-heating process continued until the two pulses were eventu-

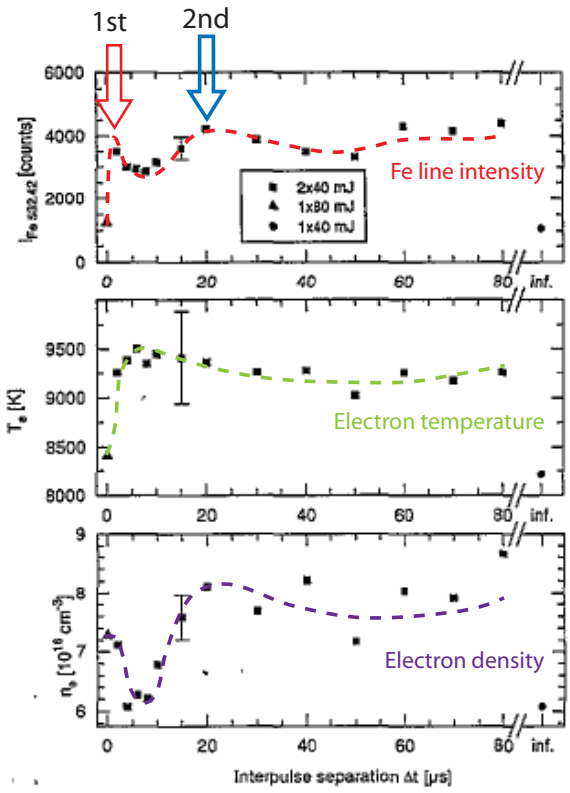

Figure 8.6: Sattmann's work in 1995 [70]. Two peaks are clearly shown on the intensity curve with a comparison of the electron temperature and density. Coloured dashed lines and the arrows were drawn as guide lines for viewing.

ally separated completely.

Hohreiter et al. [72] gave another example of a dual-pulse two-phase process but with an orthogonal arrangement. The SNR of Mg I and Si I emission line intensities vs. inter-pulse delay at 5 μs and a "second phase enhancement" at 20μs are plotted. The author also noticed that the SNR fell somewhat between the 2 μs and 20 μs. However the line intensity and peak-to-base (P/B) measurements vs. delay plot did not show any clear evidence of the "phased enhancement" 8.7(b). They concluded that the optimal inter-pulse delay was 20 μs for line intensity and 2 - 20 μs for SNR.

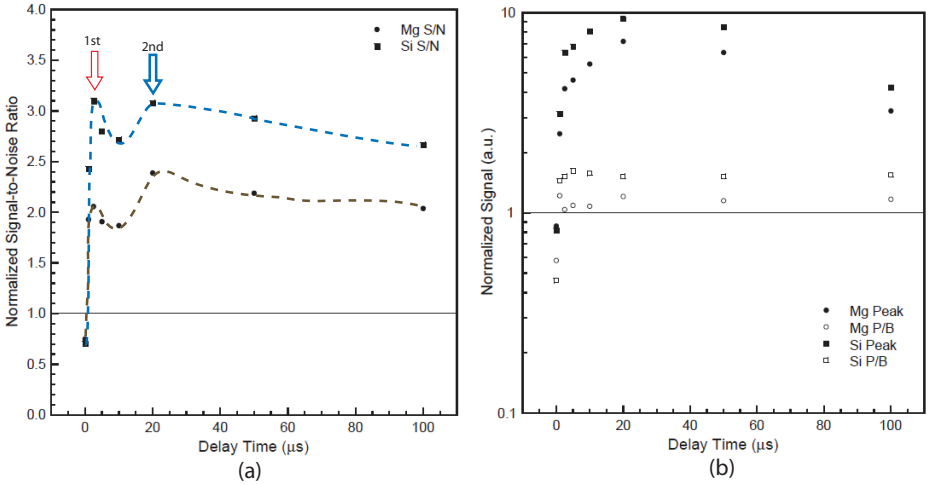

Figure 8.7: Hohreiter's work in 2005 [72]. Two peaks were clearly shown on the signal-to-noise ratio (SNR) of Mg I and Si I lines. The author reported two optimal inter-pulse delays of 5 μs and 20 μs.

Ahmed et al. [80] had a similar observation for the spectral line intensity. The authors performed an inter-pulse delay study using the fundamental (1064 nm) and the second harmonics (532 nm) of Nd:YAG lasers. Their result, as in figure 8.8, shows two peaks on the intensity curves of several Al and Mg lines. The first peak was at 5 μs and the second one was at 25 μs. The two peaks were at the same high on the Mg I line but the first peak was weaker than the second one on the other lines. So the author concluded that the optimal inter-pulse delay was 25 μs without any remarks on the first peak.

As Scaffidi et al. [88] pointed out, on the time scale of a plasma evolution, laser pulse-plasma coupling comes first and lives shortest, followed by the influence of atmospheric number density and later the sample heating effect which could persist for hundreds of μs. In our case with time-integrated or TI-LIBS in the VUV

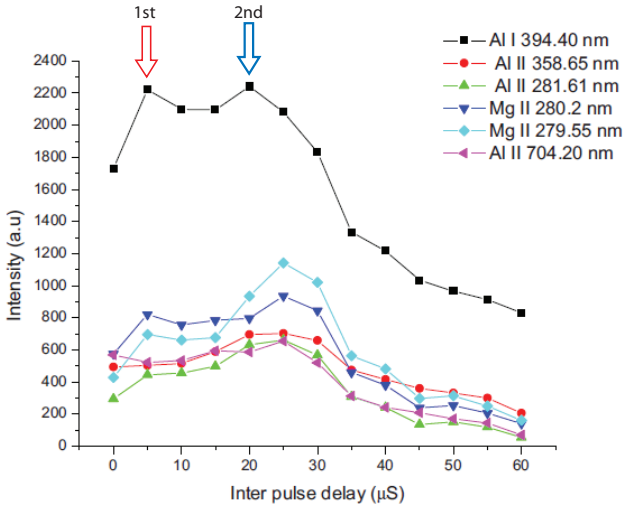

Figure 8.8: Ahmed's work in 2009 [80]. Two peaks were clearly shown on the intensity curve of several spectral lines, but the optimal inter-pulse delay was reported to be 25 μs and no discussion on the 1st peak.

at low pressure, the influence of atmospheric number density is limited since the ambient gas pressures are all below 10mbar. Sample heating effect (more significant with pre-spark orthogonal scheme) is considered to become the "second ablation" effect.

It is challenging to provide a comprehensive understanding of the entire process as none of the factors are considered to be a sole cause. Hopefully the above results and discussion will make a further step forward towards achieving a more concrete fundamental knowledge of dual-pulse laser induced plasma expansion process.

8.4 Summary

As two emission enhancements were clearly observed in the previous chapter of the inter-pulse delay effect in ambient gases, the mechanisms of the emission enhancement in the dual-pulse LIBS is studied in this chapter. Firstly the single-pulse laser induced plasma (LIP) expansion mechanism was discussed by introducing some of the plasma imaging works in the LIBS literature. Based on the knowledge of single-pulse LIP system, the investigation of intensity and signal-to-background ratio (SBR) was performed in dual-pulse mode and was followed by a discussion on the phased enhancement mechanisms. The two-phase enhancement mechanisms

can be briefly summarized as follows: the first 100 ns peak is due to the second laser re-heating the existing plasma while the μs range (1 - 4 μs) intensity revival is due to the second plasma induced by the second laser pulse interacting with the first plasma which has been buffered by the ambient gas. A literature survey on this particular inter-pulse delay topic is provided where previous studies on optical dual-pulse plasma studies have shown that the phased enhancement exists but its appearance varies in observations due to different experimental conditions. The current results are unique as they demonstrate a ubiquitous sharp intensity maximum at 100 ns time delay and a second, less intense but much wider maximum (referred as a plateau) at larger time delays of several microseconds. The latter is clearly shown to scale with the gas pressure.

Chapter 9

Limit of Detection

In the previous chapters, a number of essential parameters including hardware settings, dual-pulse defocusing, inter-pulse delay as well as ambient gas type and pressure were optimized for laser induced plasma (LIP) emission. These efforts were made to improve the limit of detection (LOD) of trace elements in steel using the LIBS technique. In the present chapter the LOD calibration of carbon (C) and sulfur (S) in steel are performed. The calculated LOD values under different conditions are compared and the optimal LOD values achieved in the current work are summarized and compared to the results in the literature.

9.1 LOD Calibration Curves for Carbon and Sulphur

The optimized parameters for LIP emission and eventually the LOD calibration for C and S in steel are summarized in table 9.1.

Parameters	Optimized Values
Spectra recording mode	Time-Integrated Space-Resolved (TISR)
Observing position	4 mm above target surface
Detector and exposure time	CCD, 2 seconds
Laser repetition rate and No. of shots	10 Hz, 20 shots
Excitation mode	Dual-pulse, Collinear
1st laser	Spectron, 1064 nm, 15 ns, 200 mJ
2nd laser	Surelite, 1064 nm, 6 ns, 665 mJ
Laser beam defocusing	5 - 10 mm under target surface
Inter-pulse delay	100 ns
Ambient gases and optimal pressures	Nitrogen (0.2 - 1.0 mbar), Argon (1 - 2 mbar), Helium (25 - 30 mbar)

Table 9.1: Parameters as optimized in the current work for LOD calibration for C and S in steel using LIBS technique.

In the next few sections, the LOD calibrations for C and S are performed systematically in single-pulse and in dual-pulse mode, in vacuum and in ambient gases, so that one can measure the LOD values before and after parameter optimization.

9.1.1 LOD calibration on the C^{2+}97.7 nm line in single- and dual-pulse mode

Figure 9.1 and Figure 9.2 present the LOD calibration curves of the C^{2+} 97.7 nm line in single- and in dual-pulse mode, respectively. Calibration in each mode was performed in vacuum and in various ambient gases at the optimal pressures (section 5.4.1). Data handling procedures including background elimination and internal referencing have been applied to the data in these two figures. In single-pulse mode (figure 9.1), the Surelite laser was set with the maximum output pulse energy of 665 mJ. In dual-pulse mode (figure 9.2), the Spectron laser and the Surelite laser, both with maximum output, were arranged in collinear dual-pulse geometry with an inter-pulse separation of the optimal 100 ns. The parameters for either single-pulse mode or dual-pulse mode were optimized to the extent allowed by the current experimental conditions, the differences between figure 9.2 and figure 9.1 then indicate the differences that dual-pulse excitation makes. As one can see, no

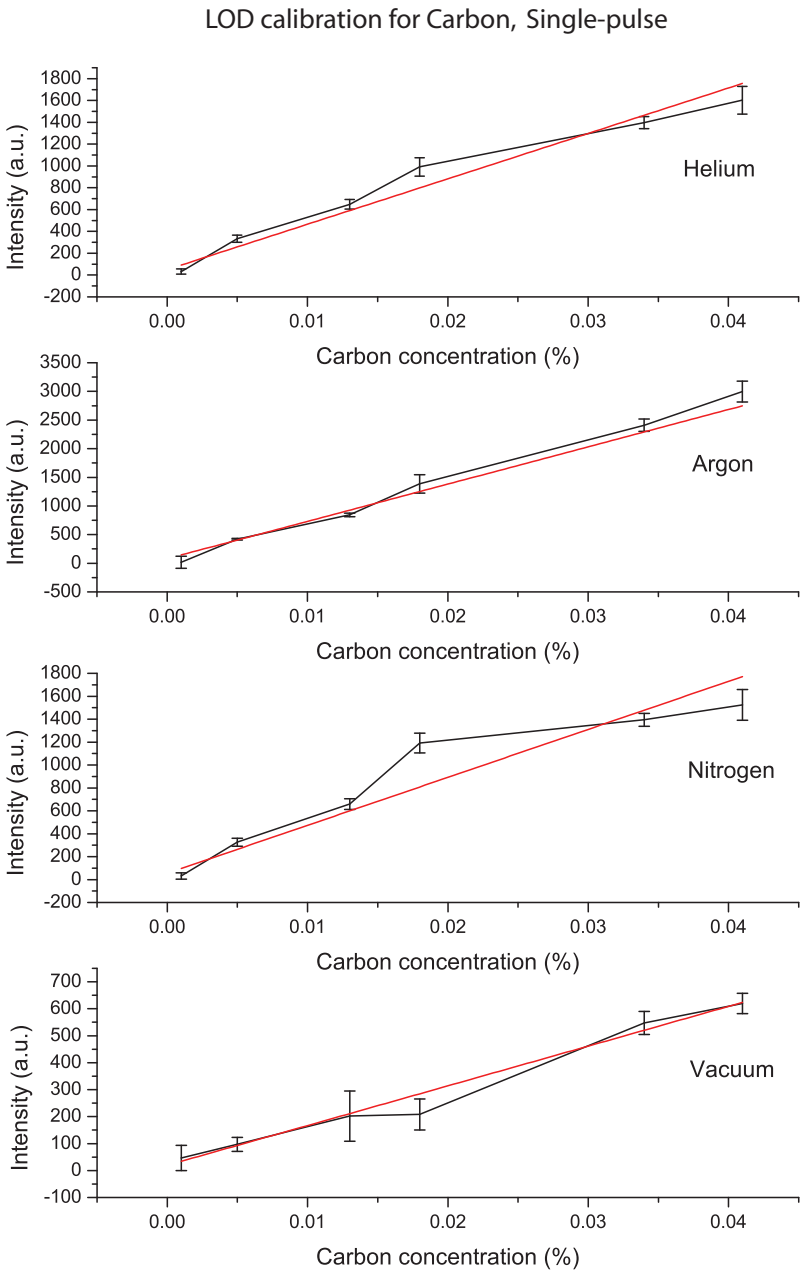

Figure 9.1: Calibration curves of limit of detection (LOD) using C^{2+} 97.7 nm. Surelite laser (1064 nm, 6 ns, 665 mJ) in single pulse mode. The straight red line is a linear fit to the experimental intensity values.

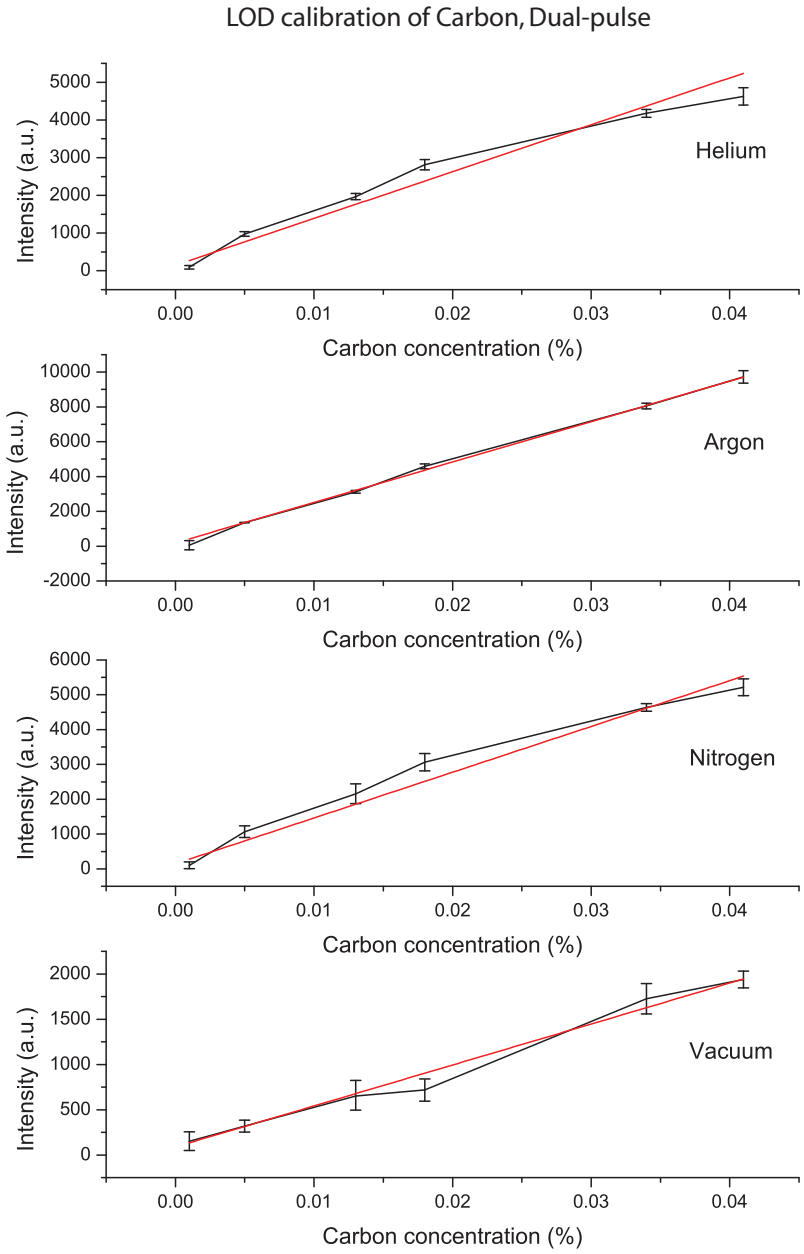

Figure 9.2: Calibration curves of limit of detection (LOD) using C^{2+} 97.7 nm. Spectron laser (1064 nm, 15 ns, 200 mJ) as ablation laser and Surelite laser (1064 nm, 6 ns, 665 mJ) as reheating laser in collinear dual-pulse geometry. Inter-pulse separation was 100 ns. The straight red line is a linear fit to the experimental intensity values.

matter in which ambient environment, the data set achieved in dual-pulse mode is more linear and has smaller error bars than that in single-pulse mode. The statistics of the linear fitting and LOD calibration results for carbon are summarized in table 9.2.

9.1.2 LOD calibration on the S^{4+}78.65 nm line in single- and dual-pulse mode

The LOD calibration curves of the S^{4+} 78.65 nm line in single-pulse mode are shown in figure 9.3 and the results in dual-pulse mode are shown in figure 9.4. In each configuration, the LOD was calibrated in vacuum, nitrogen, argon and helium. Similar to carbon, each ambient gas was set to the corresponding optimal pressure for VUV emission. In both single-pulse and dual-pulse mode, the statistical fits in ambient gases are better than that in vacuum judging from the error bars on the calibration curves indicating greater measurement uncertainty vacuum. Thus the ambient gas conditions are better for LOD calibration. Even in vacuum, the LOD curve with dual-pulse configuration (figure 9.4) had less uncertainty and a better linear fit than that with single-pulse configuration (figure 9.3). This improvement on LOD calibration curves by dual-pulse operation can also be observed in other ambient conditions with background gases present. Hence it can be concluded that dual-pulse operation offers more stable and reliable LOD calibration results.

9.2 Calculated LOD Values Under Different Conditions

In table 9.2, R^2 is a coefficient indicating the goodness of the linear fit of the LOD calibration. The definition of R^2 and the method to calculate it in a data evaluation process are provided in detail in appendix E. Generally speaking, R^2 is a coefficient which takes a value between (0, 1). The closer the R^2 value to 1, the better the fit. In the case of a linear fit for LOD calibration, R^2 is often required to be at least 0.97, R^2 values above 0.99 indicate a good linear fit and the result calculated from this data set is considered to be more reliable. For example, in single-pulse mode in table 9.2, the LOD result in nitrogen was 9.7 ppm which was better (lower) than that in argon (12.6 ppm). However, the linear fit coefficient R^2 in nitrogen was 0.875 which indicated that this data was not sufficiently good for a linear calibration (LOD). The R^2 value in argon was 0.995 implying a more reliable data set, thus the result in argon was considered better even though the LOD value was slightly

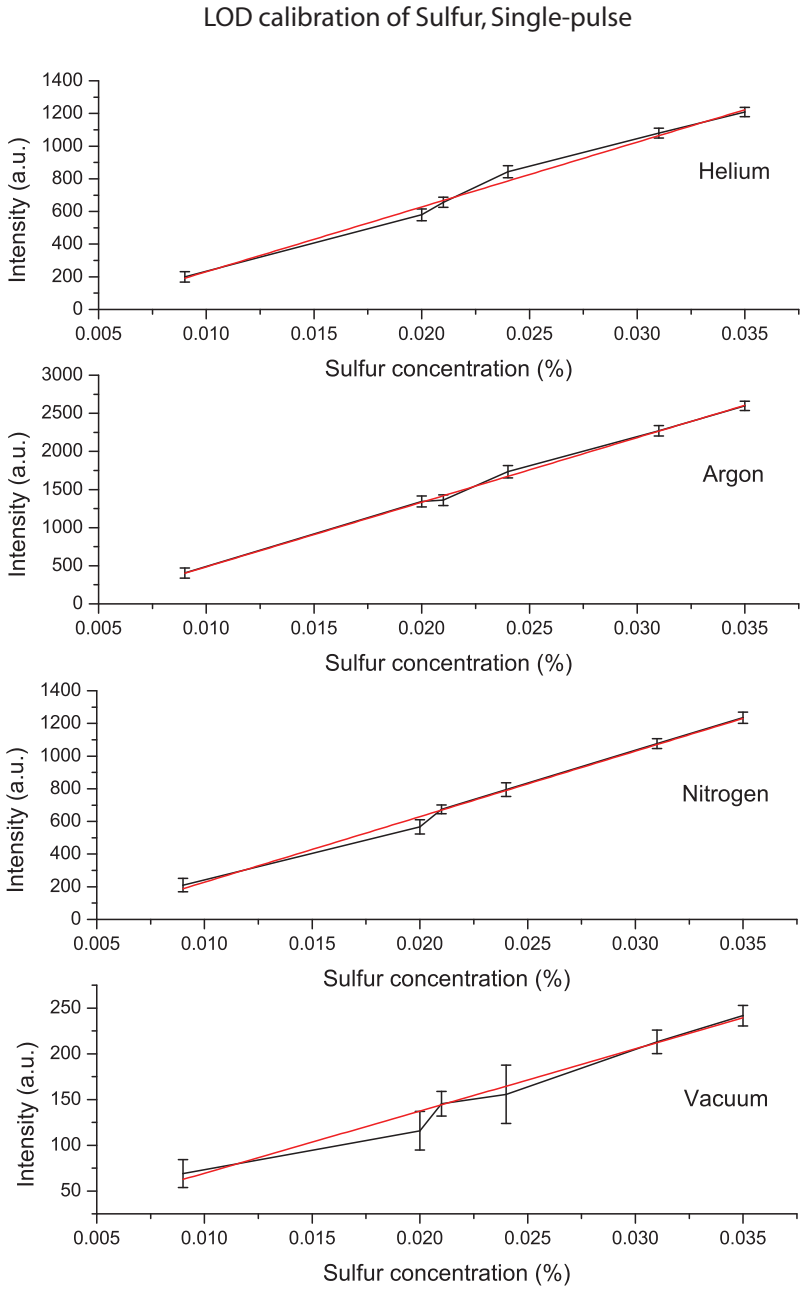

Figure 9.3: Calibration curves of limit of detection (LOD) using S^{4+} 78.65 nm. Surelite laser (1064 nm, 6 ns, 665 mJ) in single pulse mode.

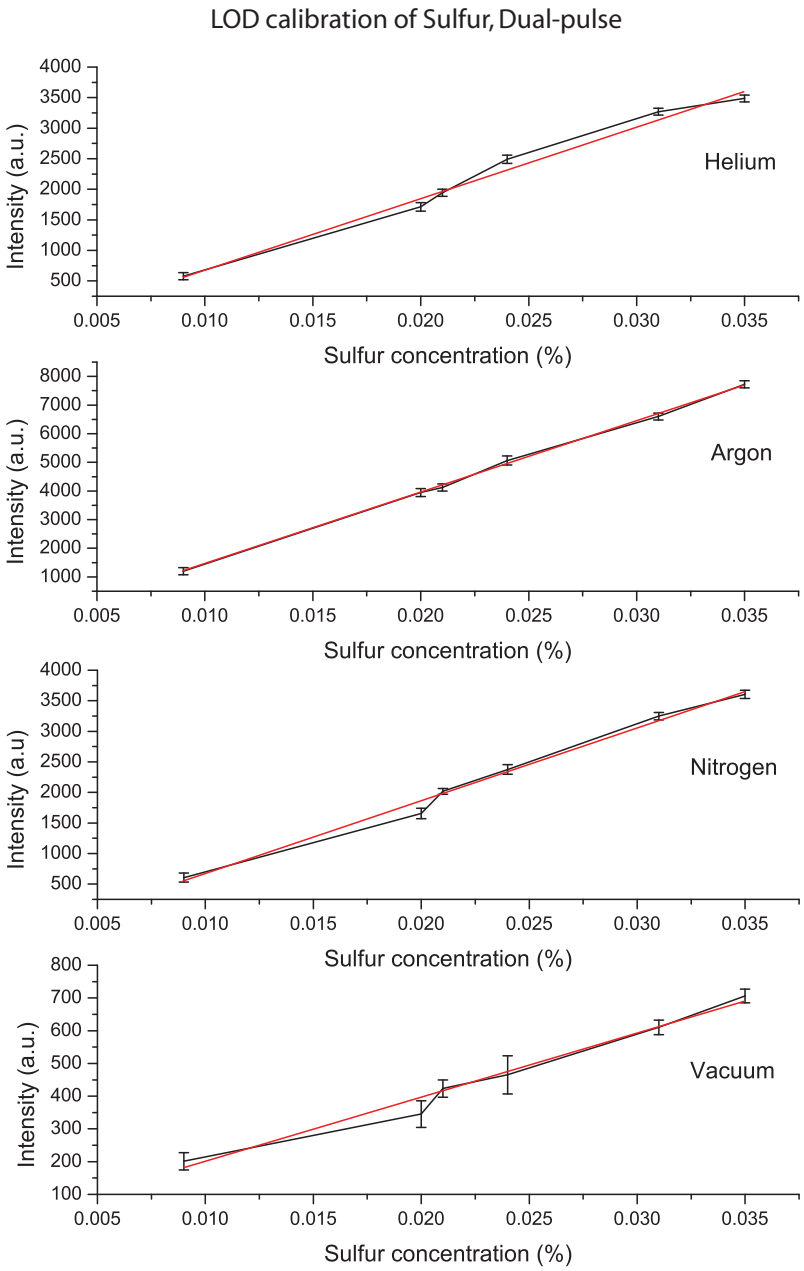

Figure 9.4: Calibration curves of limit of detection (LOD) using S^{4+} 78.65 nm. Spectron laser (1064 nm, 15 ns, 200 mJ) as ablation laser and Surelite laser (1064 nm, 6 ns, 665 mJ) as reheating laser in collinear dual-pulse geometry. Inter-pulse separation was 100 ns.

Excitation mode	Measurement condition	Linear fit parameters		Calibration LOD (ppm)	Improvement α
		R^2 σ	Slope S		
Single-pulse	Vacuum	0.97149	14855.38	54.0	
	Nitrogen	0.87491	36255.74	9.7	
	Argon	0.99531	72861.57	12.6	
	Helium	0.96073	37737.58	17.2	
Dual-pulse	Vacuum	0.98826	47291.87	13.6	3.97
	Nitrogen	0.97863	175014.95	2.9	3.34
	Argon	0.99767	232171.83	3.6	3.5
	Helium	0.98795	83048.78	5.7	3.0

Table 9.2: Statistics of LOD calibration of C in steel in various environments.

Single-pulse compared to Single-pulse

α	SP Nitrogen	SP Argon	SP Helium
SP Vacuum	5.57	4.29	3.14

Dual-pulse compared to Single-pulse

α	DP Vacuum	DP Nitrogen	DP Argon	DP Helium
SP Vacuum	3.97	18.62	15.0	9.47

Dual-pulse compared to Dual-pulse

α	DP Nitrogen	DP Argon	DP Helium
DP Vacuum	4.69	3.78	2.39

Table 9.3: Improvement on LOD values, result comparison based on improvement of LOD gain coefficient α. Data for C in steel derived from table 9.2.

higher for nitrogen.

The LOD values in dual-pulse mode were much lower than those in single-pulse mode. Lower LOD value means a lower limit of detection of the particular element and it is what we are aiming for. To measure the improvement of LOD by using dual-pulse mode, an improvement coefficient α is introduced as:

$$\alpha = \frac{LOD_{sp}}{LOD_{dp}} \tag{9.1}$$

where sp denotes 'single-pulse' and dp denotes 'double-pulse'. Higher α values indicate reductions in LOD values, thus greater improvement. The improvement coefficient α in each ambient gas are listed in the last column of table 9.2 For more comparisons, the definition of improvement coefficient α can be extended to the ratio of the original LOD value over the improved LOD value. The LOD improvement compared in different ways is shown in table 9.3.

In table 9.3, the first group of comparisons shows the improvement by ambient gases in single-pulse mode. Compared to the LOD achieved with single-pulse mode in vacuum, the greatest improvement in single-pulse mode is achieved in nitrogen. The average value of the improvement coefficient in single-pulse mode is about 4.3. The second group of comparisons is between dual-pulse in different ambient gases and single-pulse in vacuum. It is the most important comparison in the current work as it demonstrates the improvement in LOD by combining dual-pulse and ambient gases. As can be read from the values of improvement coefficient α, the greatest improvement is achieved with dual-pulse excitation in nitrogen, the second greatest improvement is achieved in argon, the α value in each case is above

15 which means the limit of detection is reduced by more than an order of magnitude. The last group of comparisons represent the improvement obtained by using ambient gases in dual-pulse mode. The average α value in dual-pulse mode is 3.62 and the greatest improvement is achieved in nitrogen.

9.3 Optimized LOD Values for C and S

The above comparisons presented the improvement by employing dual-pulse mode and ambient gases, greater improvements were achieved when combining these two factors. Although table 9.3 provided several comprehensive comparisons on the improvement of LOD values, to decide the optimal LOD with a precise and reliable calibration, calibration curves in figure 9.2 and curve fitting details in table 9.2 must be also included in the consideration. In our case, the calibration in argon has higher precision and an LOD value that matches nitrogen. Thus argon is considered the optimal gaseous environment for LOD calibration of carbon in steel, and nitrogen would be the second best choice. The calibration curves of C with dual-pulse excitation in argon and in vacuum are shown in figure 9.5. The calibration curve in argon not only has a better linear fit but also produced a much lower LOD value.

The same procedure was repeated for the S^{4+} 78.65 nm line and the calibration curves with single- and dual-pulse excitation in different ambient environments are provided in figure 9.6. Similar improvements by dual-pulse mode over single-pulse mode are exhibited by those curves and the calibration curve with dual-pulse in nitrogen and in vacuum are shown in figure 9.6. The lowest LOD value of 1.5 ppm is achieved with dual-pulse excitation in nitrogen which is over 10 times better than the LOD value in vacuum.

The above results are in agreement with the previous discussions on dual-pulse LIBS and ambient gases. Combining these two modes of operation brings an improvement to the traditional LIBS technique but the enhancements are not simply additive. There are a number of parameters to be considered in the process. Although further understanding is needed, this work provides the experimental evidence that dual-pulse excitation with ambient gas improves LIBS for VUV emission in terms of the detection limit.

The optimized LOD values achieved in our experiments are also compared to some of the existing results in the literature. Table 9.4 lists a number of LOD calibrated values in the literature. These LOD values of C and S are all based on steel matrices, the wavelength of each specific line used for LOD calibration is given in

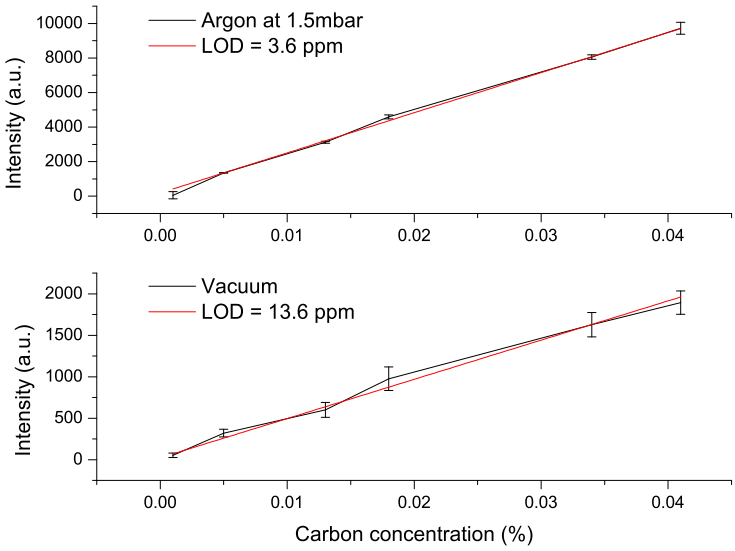

Figure 9.5: Calibration curve and derived limit of detection (LOD) using C^{2+} 97.7 nm. Spectron laser (1064 nm, 15 ns, 200 mJ) as ablation laser and Surelite laser (1064 nm, 6 ns, 665 mJ) as reheating laser were in collinear dual-pulse geometry with argon environment at 1.5 mbar. Inter-pulse separation was 100 ns. The straight red line is a linear fit to the experimental intensity values.

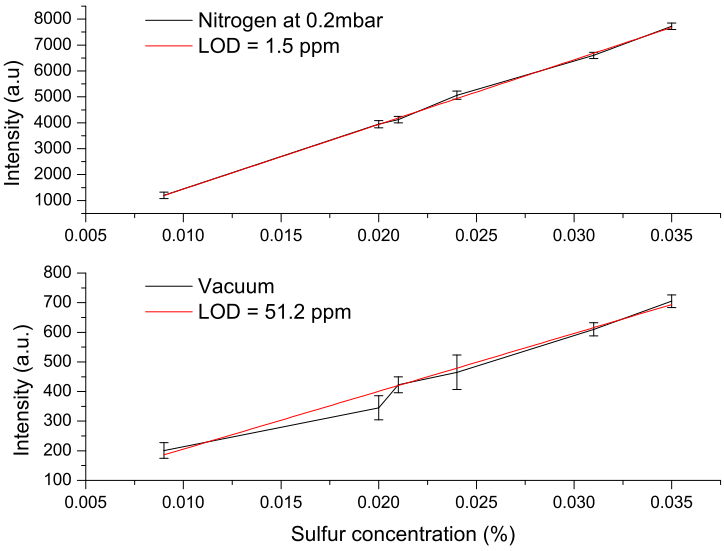

Figure 9.6: Calibration curve of limit of detection (LOD) using S^{4+} 78.65 nm. Spectron laser (1064 nm, 15 ns, 200 mJ) as ablation laser and Surelite laser (1064 nm, 6 ns, 665 mJ) as reheating laser were in collinear dual-pulse geometry with nitrogen environment at 0.2 mbar. Inter-pulse separation was 100 ns. The straight red line is a linear fit to the experimental intensity values.

the right hand column. The original sources of these works are listed next to the LOD values. Other measurement parameters such as the pulse energy and environment should also be considered as the LOD results can be significantly different when measured in different laboratories.

Element	LOD (ppm)	Reference	λ (nm)
C	65	Aguilera et al., 1992	193.09
	80	Aragon et al., 1999	193.09
	7	Sturm et al., 2000	193.09
	3	Noll et al., 2001	193.1
	5	Hemmerlin et al., 2001	133.571
	1.2	Khater et al., 2002	97.7
	3.6	*Jiang et al. (current)*	*97.7*
S	70	Gonzalez et al., 1995	180.7/182.0
	8	Sturm et al., 2000	180.73
	11	Noll et al., 2001	180.7
	4.5	Hemmerlin et al., 2001	180.731
	1.7	O'Leary, 2007	78.65
	1.5	*Jiang et al. (current)*	*78.65*

Table 9.4: LOD values in the literature compared to our results

The absolute value of 3.6 ppm for the LOD of carbon in steel using DP VUV LIBS compares well with the existing literature and is significantly better than single pulse VUV LIBS in argon where the LOD is 12.6 or as high as 54 in vacuum. It would appear from table 9.4, that DP VUV LIBS at a LOD of 3.6 ppm is perhaps only as good as the best SP LIBS values in the literature. However, absolute LOD values depend on the optical system and the optical performance of the VUV LIBS system has degraded over time. Hence the absolute LOD values cannot be directly compared and we can only look for improvements in LOD. However, when new the system was able to attain a LOD for carbon in steel of 1.2 ppm using SP VUV LIBS and so we would expect that the LOD improvement provided by DP excitation would easily translate into an achievable LOD below 1ppm .

9.4 Summary

The ultimate goal of the current work is to optimize the limit of detection (LOD) for light elements in steel. In the last result chapter, we have calibrated the LOD under different circumstances. Better LOD results were achieved under the optimized experimental conditions and data handling process. The improved LOD results

in the current work were also compared to the LOD results in the literature. Our results have shown a further improvement to the results achieved under similar conditions in the literature.

Chapter 10

Conclusions and Future Work

The final chapter of this thesis provides a general summary of the experiments performed in this work and the conclusions which can be drawn from them. During the course of the LIBS study in the VUV region, some concerns related to either lasers/optics or analysis methods have been raised. These interesting topics lead to an insight into the future of LIBS VUV development as both a fundamental study of laser-matter interactions and as an industrially important diagnostic assay tool.

10.1 General Conclusion of Dual-Pulse LIBS in Ambient Gas Condition

The main aim of this work was to further improve the ability of quantitative LIBS analysis in terms of limit of detection (LOD) for light elements (C, S) in steel. In the current work, we brought in two important improvements to the conventional LIBS system which are dual-pulse excitation and the use of ambient gases. For the first time dual-pulse LIP VUV spectroscopy is combined with low pressure ambient gases which increase the signal intensity by buffering the plasma expansion.

Firstly we introduced the basic procedure of the conventional LIBS system with one laser in single-pulse mode in vacuum. An initial survey of the VUV spectrum from 30 - 130 nm was carried out to calibrate the raw spectrum data from pixel point to wavelength. By reference to results from the National Institute of Standards and Technology (NIST), we managed to identify a number of the spectral lines of interest and to ascertain which light element emission lines were most suitable for the present work. These lines were: C^{+} 90.41 nm, C^{2+} 97.7 nm, S^{3+} 75.03 nm and S^{4+} 78.65 nm. Among these lines, C^{2+} 97.7 nm and S^{4+} nm had the highest integrated intensities and signal-to-background ratios, thus these two lines were chosen as the

main lines with which to conduct the optimization studies.

Secondly, we carried out a feasibility study of the unique combination of dual-pulse LIP VUV emission in gas. Apart from the main light element emission lines chosen previously, a few lines belonging to the matrix element (Fe^{2+} 89.12 nm, Fe^{2+} 98.4 nm) and the ambient gases (N^{2+} 91.6 nm, Ar^{+} 91.98 nm) were also included to perform a systematic investigation of the VUV emission. The first series of experiments involved the comparison between single-pulse ablation and double-pulse excitation. The peak intensity of the C^{2+} 97.7 nm line showed that dual-pulse excitation could bring up to a 3.2 fold signal gain. As the laser pulse energy was varied within the range of 300 mJ to 665 mJ, we found that the higher the reheating pulse energy is, the greater the signal gain achieved. Thus the optimal pulse(es) configuration for our work was: Spectrum laser (1064 nm, 15 ns, 200 mJ) serving as the ablation laser, Surelite (1064 nm, 6 ns, 665 mJ) used as the second laser, producing a reheating pulse with a certain pulse interval after the plasma was initiated by the ablation pulse.

Following the dual-pulse energy testing results, the influence of the ambient gas type and pressure was examined. Three types of gases (Nitrogen, Argon and Helium) within the pressure range of 0.01 - 700 mbar were examined. The optimal pressures for VUV emission in each gas were: nitrogen 0.3 mbar, argon 1.5 mbar and helium 28 mbar. The line intensity and signal-to-background ratios were all found to be superior to those in vacuum. In this study we also discovered that the main concerns for deep VUV emission (70 nm -100 nm) were the absorption in nitrogen, the intensity saturation in argon and the inefficient buffering in helium.

With the success of combining the dual-pulse scheme and the use of ambient gas, we extended our study into the optimization of some of the core parameters. One of them was the defocusing effect of the laser beam in single-pulse mode or of the reheating beam in dual-pulse mode. The focus condition was varied by moving the lens into and out of focus on the target surface with the result that the power density on the surface changed. This set of experiments was carried out in both vacuum and gas environments. The emission trends upon different lens-to-sample distances were quite similar. In single-pulse mode, two peaks were found on the intensity curve implying that the emission signal was improved when the laser beam was focused either 10 mm under or 5 mm above the sample surface. In dual-pulse mode, the optimal reheating focal point was found to be 10 mm under the target surface.

Another crucial factors for optimizing dual-pulse excitation was the inter-pulse delay time. With our time-integrated space-resolved LIBS system the optimal inter-

pulse separation was found to be 100 ns for nearly all the conditions (vacuum or gas at different pressure). This interesting discovery led us to explore the mechanism of plasma expansion. The behavior of the signal-to-background ratio along with the emission intensity trend helped us propose a "two-phase enhancement" theory to explain the effect of the inter-pulse delay.

Parameters of the LIBS system, some improvements in data handling were also considered. Finally, with the analysis of optimum conditions completed, calibration curves of the data were plotted using a set of targets with low concentrations of carbon and sulphur present in them. The best limit of detection (LOD) value for C^{2+} 97.7 nm line was 3.6 ppm in argon and the best LOD value for S^{4+} 78.65 nm line was 1.5 ppm in nitrogen. Both of these LOD results were far better than those produced with the single-pulse technique in vacuum and they are close to or even better than the best available LIBS limit of detection published in the literature to date (C: 1.2 ppm by Khater [31], S: 1.8 ppm by O'Leary [4]).

10.2 Future Work on LIBS

10.2.1 The understanding of the LIBS process

Understanding the process of LIP formation and its further evolution improves the ability to control, reproduce, and increase the analytical capability and acceptance. Efforts towards establishing a solid LIBS foundation are made in both experimental and modeling ways. These aspects include:

- *Laser/Optical and technique related*
  These factors are usually considered in terms of the choice of experimental apparatus. Besides our current experimental conditions (two ns Nd:YAG lasers, vacuum normal incident grating spectrometer, and CCD camera), there are some other interesting options such as:
  Lasers: fs lasers to provide shorter pulses with higher power density; a combination of different laser beam harmonics (e.g. [82]);
  Optics: using fiber optics to carry the laser beam closer to the sample and retrieve the emitted light; development of compact echelle spectrographs to provide complete spectral coverage in a relatively small package;

- *Modeling the plasma process*
  The Taylor-Sedov model [77] has been widely used to describe the expansion of a blast wave (plasma). Recent works extend the model into vacuum

or controlled ambient gases (e.g. [76]). More sophisticated models are desirable in advancing the understanding of the interaction of the plasma with the ambient environment and even the process of dual-pulse excitations in ambient gas which includes plasma-plasma and plasma-ambience interactions. Models of the effects of the ambient atmosphere on VUV emission can also provide theoretical support for space exploration experiments (e.g. Mars type atmosphere [89]).

- *Chemometrics and other analytical methods*
  As a chemical analysis based science, chemometrics has recently become a powerful analytical tool in LIBS research. At the international LIBS conference in 2008, there were only a handful of talks that included a substantial portion of chemometrics in the analysis. Two years later, at the most recent LIBS conference in 2010, over half of the presentations were related to multivariate calibration or multivariate curve resolution. The growth of chemometrics underlines the LIBS potential for multi-element analysis.

In order to gain further insight into the process of the phased-enhancement proposed in the current work and the LIP evolution process in general, it would be interesting to use a fast framing camera to capture the temporal evolution of the plasma in single- and dual-pulse mode for various time delays under different ambient conditions. An example of such an approach has been demonstrated for an atmospheric pressure LIBS experiment by Mao et al. [90].

10.2.2 The development of the dual-pulse LIBS technique

As indicated earlier, a great deal of research has been performed over the past number of years in the use of more than one laser pulse for the generation of laser plasmas for the LIBS technique. A comprehensive review of dual-pulse excitation has been published by Babushok et al. [91]. The geometrical configurations of the dual-pulse scheme for LIBS can be summarized as follows:

- Collinear dual-pulse within the same flashlamp pulse.
- Collinear beams from two lasers focused on the same spot on the target.
- Orthogonal beams with one beam perpendicular and one parallel to the target surface:
  a) the beam parallel to the target surface is first in time forming an air spark (pre-spark/pre-ablation mode, at high gas pressure);

b) the beam parallel to the target surface is second in time, it reheats the material ablated by the first pulse (reheating mode).

Our work has focused on the collinear reheating dual-pulse excitation mode. It would be interesting to apply other geometrical arrangements in future dual-pulse applications, using the spatially resolved VUV detection mode.

Summary

The main goal of the present work has been the low-level quantitative determination of carbon and sulfur in steel. Carbon was chosen as one of the primary test elements because it plays an important role in determining some of the mechanical and physical properties such as stiffness and ductility of almost all steel products. Sulfur was another light element tested in this work because it has a large and mostly undesirable effect on the material characteristics of steel, with most steel-making processes designed to remove it completely from the end product.

To achieve the goal of precisely determining the content of carbon and sulfur in steel, a number of optical emission spectroscopy (OES) experiments were carried out designed to optimize the emission from carbon and sulfur ions using the laser-induced breakdown spectroscopy (LIBS) technique. This technique typically involves the use of a high power laser to generate a hot, dense and short-lived plasma on the surface of a solid target. Radiation from the plasma is then used for both quantitative and qualitative evaluation of both major and minor elements in the material. LIBS has been almost exclusively used in the visible and UV regions of the electromagnetic spectrum owing to the ease of use in this region. Recently, interest has extended to the VUV region due to the fact that most of the strongest emission lines of light elements (C, S, P, etc.) are from their ions in the vacuum ultraviolet.

The time-integrated space-resolved LIBS system employed in our work is particularly designed for the quantitative characterization of steel alloys. In order to improve the LIBS VUV technique aiming for better analytical figures of merit, i.e. intensity, sensitivity, precision, etc., two important techniques were introduced to the basic LIBS VUV system. In this work we evidenced the dual-pulse enhancement for LIBS in the VUV. Ambient atmosphere buffers the plasma expansion thus increasing the signal by extending the plasma life-time. These two approaches turned out to be a successful combination for LIBS VUV emissions. The emission intensity and the signal-to-background ratio were both found to increase and the

calibration results of the LOD for carbon and sulfur were improved compared to previous works in the literature.

Our results not only show an ubiquitous dramatic intensity enhancement at 100 ns in vacuum and in ambient gases but also clearly demonstrate a second intensity revival in the μs delay range in ambient gases.

Although the mechanisms underlying the signal gain as a function of the inter-pulse time delay, have not been fully elucidated in this work, a number of questions have been raised and some insights have been gained. Specific questions addressed the role of the inter-pulse time delay and the ambient gas type and pressure. A "phased enhancement" theory was proposed based on our unique observations. Hopefully it will provide one more step towards a better understanding of the dual-pulse ambient gas enhancement mechanisms.

Publications and Conference Presentations

- *X. Jiang*, P. Hayden, J. Costello and E. Kennedy, Dual-Pulse Laser Induced Breakdown Spectroscopy with Ambient Gas in the Vacuum Ultraviolet: Optimization of Parameters and Detection of Light Elements in Steel, *Spectrochimica Acta Part B: Atomic Spectroscopy*, complete draft.
- *X. Jiang*, P. Hayden, R. Laasch, J. Costello and E. Kennedy, Effect of Inter-Pulse Delay and Emission Enhancement Mechanism in Dual-Pulse Laser Induced Breakdown Spectroscopy in the VUV with Ambient Gas, 2012, *Spectrochimica Acta Part B: Atomic Spectroscopy*, complete draft.
- International Symposium on Intense field, Short Wavelength Atomic and Molecular Processes, July 2011, Ireland.
- 6^{th} International Conference on LIBS, September 2010, USA.
- 10^{th} International Conference on Laser Ablation, November 2009, Singapore.
- 5^{th} Euro-Mediterranean Symposium on Laser-Induced Breakdown Spectroscopy, September 2009, Italy.
- 5^{th} International Conference on Laser-Induced Breakdown Spectroscopy, September 2008, Germany.

Appendix A

Criteria for Thermodynamic Equilibrium

Considering a plasma as an ideal thermodynamic enclosure at a temperature T, there are four principles must be satisfied in such a thermodynamic equilibrium state [6]:

(a) all particles, electrons, neutral species and ions obey the *Maxwell velocity distribution law*;

$$dn_v = 4\pi N \left(\frac{m}{2\pi k_B T_k}\right) exp\left(\frac{-mv^2}{2k_B T_k}\right) v^2 dv \tag{A.1}$$

where dn_v is the number of particles (of mass m) having velocities between v and $v + dv$; N is the total number density of particles at all velocities; k_B is Boltzmann's constant and T_k is the kinetic temperature.

(b) the population distributions over the states of any atom or ion are given by the *Boltzmann formula*;

$$\frac{N_i}{N_k} = \frac{g_i}{g_k} exp\left(-\frac{\chi(i,k)}{k_B T_{exc}}\right) \tag{A.2}$$

where i and k are lower and upper energy levels respectively; g is the statistical weight of the level, calculated as $g_l = 2J_l + l$, where J is the total angular momentum quantum number for the species under consideration; $\chi(i,k)$ is the energy difference between the two levels and T_{exc} is the excitation (population) temperature of the species under consideration. Another form of the Boltzmann distribution can be obtained by relating the number density of atoms/ions in the excited state k, N_k, to the total number density of the corresponding species (in the same state

of ionization), N_T:

$$\frac{N_k}{N_T} = \frac{g_k}{Q(T_{exc})} exp\left(-\frac{E_k}{k_B T_{exc}}\right) \tag{A.3}$$

where E_k is the excitation energy of the state k as measured in reference to the ground energy level of the species in the same state of ionization and $Q(T_{exc})$ is the partition function of the atoms/ions under consideration and is given by:

$$Q(T_{exc}) = \sum_k g_k exp\left(-\frac{E_k}{k_B T_{exc}}\right) \tag{A.4}$$

The sum is over all allowed electronic energy levels.

(c) the number of ions in stage z relative to the number in stage $(z-1)$ is given by the *Saha equation;*

$$\frac{N_z n_e}{N_{z-1}} = 2\left(\frac{2\pi m_e k_B T_{ion}}{h^2}\right)^{3/2} \frac{Q_z(T_{ion})}{Q_{z-1}(T_{ion})} exp\left(-\frac{E_{z-1}(\infty)}{k_B T_{ion}}\right) \tag{A.5}$$

where N_z and N_{z-1} are numbers of ions in two ionization stages z and $z-1$; $z = 1, 2, 3, ...$; n_e and T_{ion} are the electron number density and ionization temperature respectively; h is Planck's constant and $E_{z-a}(\infty)$ is the ionization energy of the $z-1$ ionization stage.

(d) the intensity distribution of the radiation in the cavity as a function of frequency and temperature is given by the *Planck formula*:

$$I(v,T) = \frac{2hv^3}{c^2}\left[exp\left(\frac{hv}{k_B T}\right) - 1\right]^{-1} \tag{A.6}$$

$I(v,T)$ is the energy per unit time (or the power) radiated per unit area of emitting surface in the normal direction per unit solid angle per unit frequency by a black body at temperature T; h is the Planck constant; c is the speed of light in a vacuum; k is the Boltzmann constant; v is the frequency of the electromagnetic radiation; and T is the temperature of the body in Kelvins.

The corresponding expression for the wavelength λ is:

$$I(\lambda,T) = \frac{2h^2}{\lambda^5}\left[exp\left(\frac{hc}{\lambda k_B T}\right) - 1\right]^{-1} \tag{A.7}$$

In terms of the specific radiation energy densities u_v, the above expressions will be:

$$u_v = \frac{8\pi hv^3}{c^3}\left[exp\left(\frac{hv}{k_B T}\right) - 1\right]^{-1} \tag{A.8}$$

and

$$u_v = \frac{8\pi hc}{\lambda^5}\left[exp\left(\frac{hc}{\lambda k_B T}\right) - 1\right]^{-1} \tag{A.9}$$

At short wavelengths ($\frac{hc}{\lambda k_B T} >> 1$), Wien's approximation may be applied:

$$B_\lambda(T) \approx \frac{2hc^2}{\lambda^5} exp\left(-\frac{hc}{\lambda k_B T}\right) \tag{A.10}$$

For long wavelengths ($\frac{hc}{\lambda k_B T} << 1$), we have the Rayleigh-Jeans radiation law:

$$B_\lambda(T) \approx \frac{2k_B c}{\lambda^4} T \tag{A.11}$$

Appendix B

Kirchhoff's Law of Radiation

Kirchhoffs law states that given thermal equilibrium within an enclosure, the radiation inside is independent of the nature of the walls, or the objects they contain. This is known as the concept of universality. That is, that the radiation within an enclosure can always be described by a universal function dependent only on temperature and frequency [7]. For plasma in a thermodynamic equilibrium state, Kirchhoff's law of radiation is stated as:

$$\varepsilon_v = k(v)B_v(T) \tag{B.1}$$

and

$$\varepsilon_\lambda = k(\lambda)B_\lambda(T) \tag{B.2}$$

where ε and k are the coefficients for emission and absorption respectively. For LTE plasmas, the energy emitted from a unit volume, per second and per unit solid angle can be expressed by the emission coefficient ϵ of the spectral line, integration over the spectral line profile:

$$\epsilon_L = \sum_{line} \epsilon_{v,L} dv = \frac{h v_{pq}}{4\pi} A_{qp} N_q \tag{B.3}$$

A_{qp} is the Einstein coefficient to describe the spontaneous transition from a higher level q to a lower level p. N_q is the population of the excited state. This equation B.3 is known as the fundamental relation of emission spectroscopy. From

Appendix A, we can substitute N_q with the Boltzmann expression:

$$I = \frac{hv}{4\pi} A_{qp} \frac{N_T g_q}{Q(T_{exc})} exp\left(-\frac{E_q}{k_B T_{exc}}\right) \tag{B.4}$$

This equation can be used to determine the excitation temperature T_{exc} in LTE plasmas. The absorption coefficient of a spectral line $k_L(v)$ can be described by the atomic cross section of the line, $\sigma_L(v)$, as:

$$k_l(v) = \sigma_L(v) N_p l \tag{B.5}$$

where N_p is the number density of atoms/ions in the lower energy level p. l is the length of the plasma over which the absorption takes place. Both $k_L(v)$ and $\sigma_L(v)$ depend on the frequency v and thus can be described by the spectral line profile $I(v)$ as $\sum I(v)dv = 1$. In the case where the upper energy level q is not populated, the absolute value of $k_L(v)$, from Ladenburg's formula [92], is:

$$\sum k_L(v)dv = \frac{hv}{c} N_p B_{pq} \tag{B.6}$$

where B_{pq} is the Einstein coefficient for absorption. Combining it with the line profile, we have:

$$k_L(v) = \frac{hv}{c} N_p B_{pq} I(v) \tag{B.7}$$

When more atoms/ions are promoted to the upper energy level q, the effect of stimulated emission must be considered in equation B.7. This modification is based on the fact that the frequencies of the incident radiation and the stimulated transition are the same. The absorption coefficient of the spectral line can be written as:

$$K_L(v) = \frac{hv}{c} P(v)(N_p B_{pq} - N_q B_{qp}) = k_L(v)\left(1 - \frac{N_q B_{qp}}{N_p B_{pq}}\right) \tag{B.8}$$

For collision dominated LTE plasmas, the ratio of particle densities can be replaced by Boltzmann's factor, $e^{-hv/k_B T_{exc}}$, then:

$$K_L(v) = k_L(v)\left(1 - exp(-\frac{hv}{k_B T_e})\right) \tag{B.9}$$

Appendix C

A Quick Note on Atomic Spectral Lines

There are two types of atomic spectral lines corresponding to two types of transitions:

Emission line: formed when an electron makes a transition from a higher energy level of an atom to a lower energy state, emitting a photon of a particular energy and wavelength, and

Absorption line: formed when an electron makes a transition from a lower to a higher energy level, with a photon being absorbed in the process.

The two states must be bound states in which the electron is bound to the atom, so the transition is sometimes referred to as a "bound-bound" transition, as opposed to a transition in which the electron is ejected out of the atom completely ("bound-free" transition) into a continuum state, leaving an ionized atom. An illustration of the transitions between the two states is shown in figure C.1. The rate at which transitions take place between the levels k and i is given for atoms interacting with radiation whose energy density per unit bandwidth is $\rho(v)$.

In 1916, Albert Einstein proposed that there are three processes occurring in the formation of an atomic spectral line. The three processes are referred to as *spontaneous emission*, *stimulated emission* and *photon absorption*. Each process is associated with an ***Einstein coefficient*** which is a measure of the probability of that particular process occurring.

Spontaneous emission

In a spontaneous emission process, an electron "spontaneously" (i.e. without any outside influence) decays from a higher energy level (state 2 with energy E_i) to a lower one (state i with energy E_k). The associated Einstein coefficient is $A_{ki}(s^{-1})$,

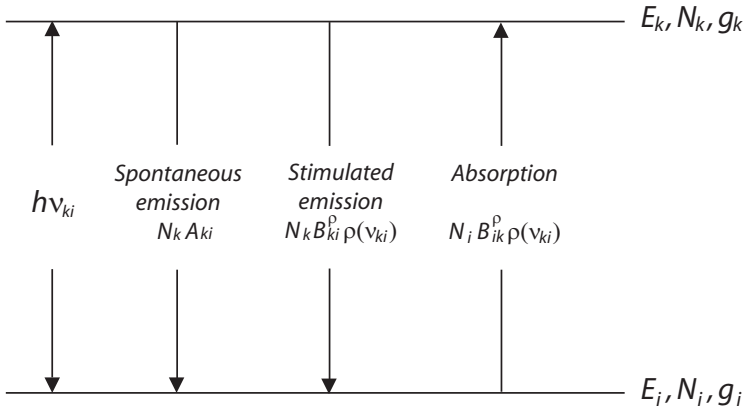

Figure C.1: Spontaneous and stimulated emission and absorption of radiation.

and the emitted photon energy is $hv = E_k - E_i$. Due to the uncertainty principle ($\Delta E \Delta t \geq h$), the transition actually produces photons within a narrow range of frequencies called the spectral line width. If n_i is the number density of atoms in state i then the change in the number density of atoms in state i per unit time due to spontaneous emission is given by:

$$\left(\frac{dn_i}{dt}\right)_{A_{ki}} = A_{ki} n_k \tag{C.1}$$

Stimulated emission

Stimulated emission is a process in which an electron is "stimulated" by the presence of an electromagnetic radiation (in the form of an electromagnetic field or photons) and undergoes a transition from a higher level (state k) to a lower level (state i). The stimulation source in this case has the same frequency as the transition ($E_k - E_i = hv$). The corresponding Einstein coefficient is B_{ki} which describes the probability of the process per unit time per unit spectral radiance. The change in the number density of atoms in state i per unit time due to stimulated emission is:

$$\left(\frac{dn_i}{dt}\right)_{B_{ki}} = B_{ki} n_k \rho(v) = B_{ki} n_k \frac{hv^3}{c^2(e^{hv/kT} - 1)} \tag{C.2}$$

where $\rho(v)$ is the radiation density of the radiation field at the frequency of the transition.

Photon absorption

In a photon absorption process, a photon is absorbed by an atom causing an electron to undertake the transition from a lower level (state i) to a higher one (state

k). This process is associated with Einstein coefficient B_{ik} and the change of the number of atoms in state i due to absorption is described as:

$$\left(\frac{dn_i}{dt}\right)_{B_{ik}} = -B_{ik} n_i \rho v \tag{C.3}$$

Appendix D

More Details on Inter-pulse Delay Time Investigations

During the investigations in this work, many spectra, under a wide range of experimental conditions, were recorded. Some further examples of results for argon and helium are included in this appendix.

Figure D.1 shows the intensity dependence on inter-pulse delay time in argon and figure D.2 shows that in helium, both exhibit four different spectral lines. Although there were differences on the intensities, the 'second plateau' was found on all the curves.

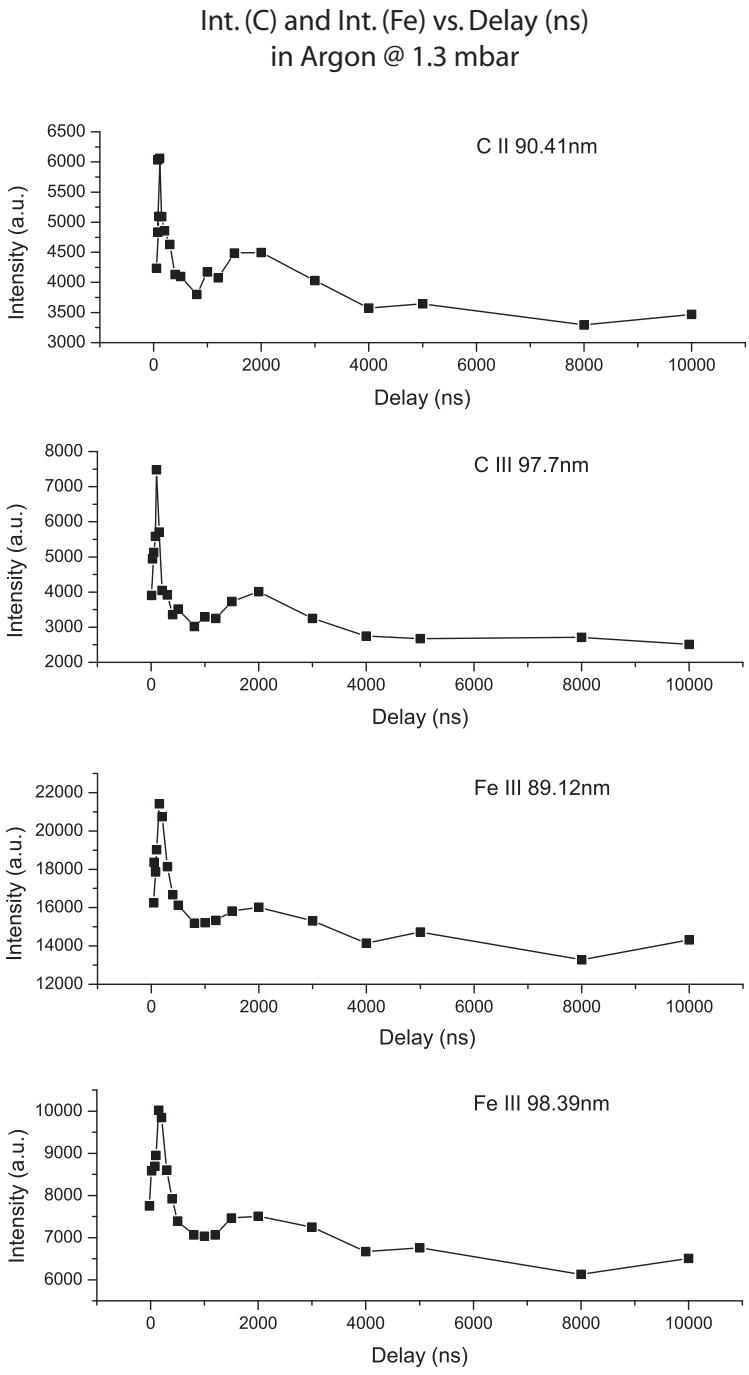

Figure D.1: Intensity dependence on inter-pulse delay time in argon at 1.3 mbar.

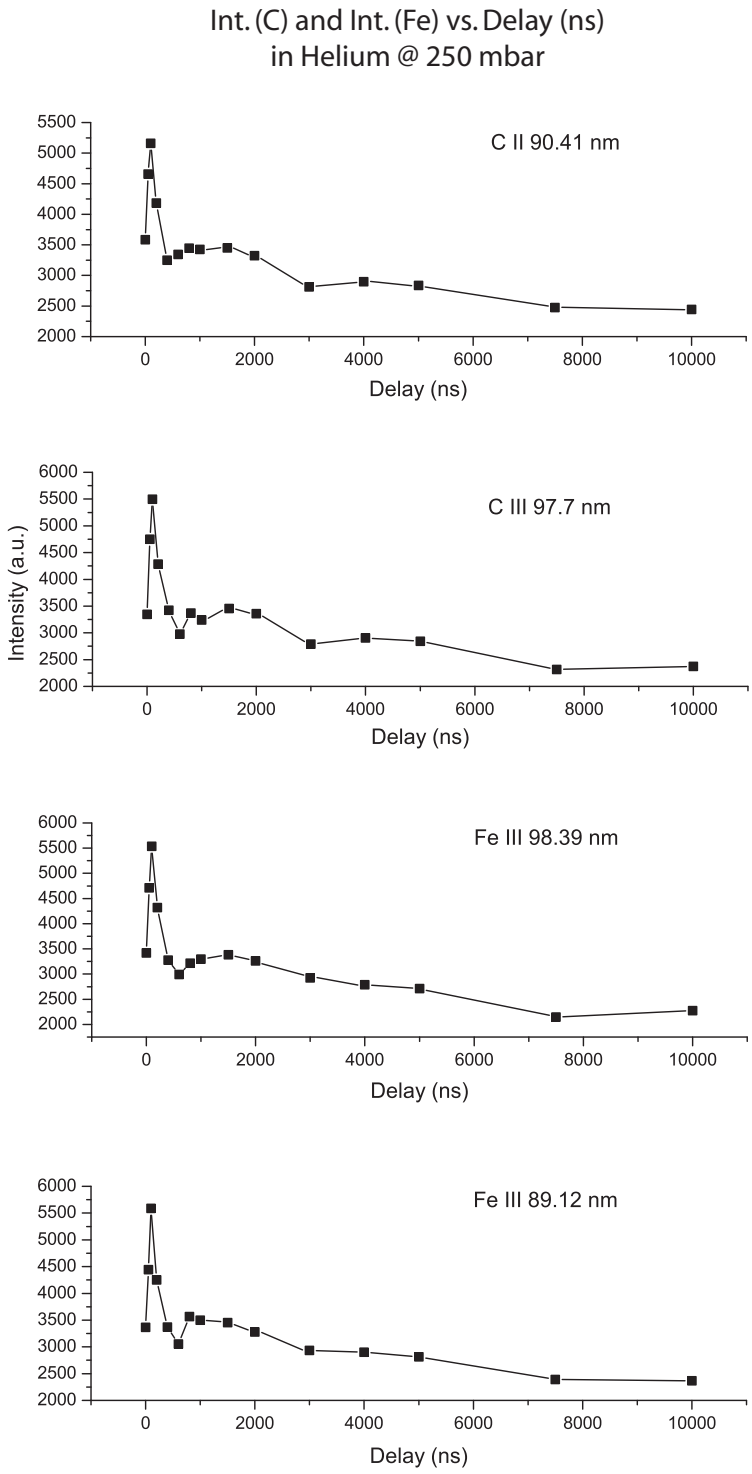

Figure D.2: Intensity dependence on inter-pulse delay time in helium at 250 mbar.

Appendix E

Goodness-of-Fit Statistics

To examine the goodness-of-fit statistics after using graphical methods to evaluate the trend of a group of data (i.e. linear fit to LOD in our case), We used the Matlab Curve Fitting Toolbox which supports some of the important statistics for goodness-of-fit including the sum of squares due to error (SSE) and the R-square.

Sum of Squares Due to Error

This statistic measures the total deviation of the response values from the fit to the response values. It is also called the summed square of residuals and is usually labeled as SSE. In a fitting $y = f(x)$ for a data set of n data points, the SSE is defined as:

$$SSE = \sum_{i=1}^{n} w_i (y_i - \hat{y}_i)^2 \tag{E.1}$$

A value closer to 0 indicates that the model has a smaller random error component, and that the fit will be more useful for prediction.

R-square

This statistic measures how successful the fit is in explaining the variation of the data. Put another way, R-square is the square of the correlation between the response values and the predicted response values. It is also called the square of the multiple correlation coefficient and the coefficient of multiple determination. R-square is defined as the ratio of the sum of squares of the regression (SSR) and the total sum of squares (SST). SSR is defined as:

$$SSR = \sum_{i=1}^{n} w_i (\hat{y}_i - \bar{y}_i)^2 \tag{E.2}$$

SST is also called the sum of squares about the mean, and is defined as:

$$SST = \sum_{i=1}^{n} w_i(y_i - \bar{y}_i)^2 \tag{E.3}$$

where SST = SSR + SSE. Given these definitions, R-square is expressed as:

$$R^2 = \frac{SSR}{SST} = 1 - \frac{SSE}{SST} \tag{E.4}$$

R-square can take on any value between 0 and 1, with a value closer to 1 indicating that a greater proportion of variance is accounted for by the model. For example, an R-square value of 0.8234 means that the fit explains 82.34% of the total variation in the data about the average. Note that it is possible to get a negative R-square for equations that do not contain a constant term. Because R-square is defined as the proportion of variance explained by the fit, if the fit is actually worse than just fitting a horizontal line then R-square is negative. In this case, R-square cannot be interpreted as the square of a correlation. Such situations indicate that a constant term should be added to the model.

Bibliography

[1] D.A. Cremers, L.J. Radziemski, and J. Wiley. *Handbook of laser-induced breakdown spectroscopy*. Wiley Online Library, 2006.

[2] H.R. Griem. Principles of plasma spectroscopy. *Proceedings of the Physical Society*, 1, 2005.

[3] T.P. Hughes. Plasmas and laser light. 1975.

[4] O'Leary E.P. *VUV laser-induced plasma spectroscopy for low level sulphur detection in steel*. PhD thesis, Dublin City University, Dublin, Ireland, 2007.

[5] H.R. Griem and R.H. Lovberg. *Plasma physics*, volume 9. Academic press, 1970.

[6] PK Carroll and ET Kennedy. Laser-produced plasmas. *Contemporary Physics*, 22(1):61–96, 1981.

[7] Khater M. *Spectroscopic investigations of laser-produced steel plasmas in the vacuum ultraviolet*. PhD thesis, Dublin City University, Dublin, Ireland, 2001.

[8] RWP McWhirter. Plasma diagnostic techniques. *Academic Press, New York*, page 201, 1965.

[9] H.R. Griem. *Principles of Plasma Spectroscopy*. Cambridge University Press, Cambridge, UK, 1997.

[10] A. Corney. *Atomic and laser spectroscopy*. Clarendon press, 1978.

[11] J.D. Winefordner, I.B. Gornushkin, T. Correll, E. Gibb, B.W. Smith, and N. Omenetto. Comparing several atomic spectrometric methods to the super stars: special emphasis on laser induced breakdown spectrometry, libs, a future super star. *J. Anal. At. Spectrom.*, 19(9):1061–1083, 2004.

[12] K. Song, Y.I. Lee, and J. Sneddon. Recent developments in instrumentation for laser induced breakdown spectroscopy. *Applied Spectroscopy Reviews*, 37(1):89–117, 2002.

[13] A.W. Miziolek, V. Palleschi, and I. Schechter. *Laser-induced breakdown spectroscopy (LIBS): fundamentals and applications*. Cambridge Univ Pr, 2006.

[14] J.P. Singh, J.R. Almirall, M. Sabsabi, and A.W. Miziolek. Laser-induced breakdown spectroscopy (libs). *Analytical and Bioanalytical Chemistry*, pages 1–2, 2007.

[15] DA Rusak, BC Castle, BW Smith, and JD Winefordner. Recent trends and the future of laser-induced plasma spectroscopy. *TrAC Trends in Analytical Chemistry*, 17(8-9):453–461, 1998.

[16] S. Amoruso, R. Bruzzese, N. Spinelli, and R. Velotta. Characterization of laser-ablation plasmas. *Journal of Physics B: Atomic, Molecular and Optical Physics*, 32:R131, 1999.

[17] C. Pasquini, J. Cortez, L.M.C. Silva, and F.B. Gonzaga. Laser induced breakdown spectroscopy. *JOURNAL-BRAZILIAN CHEMICAL SOCIETY*, 18(3):463, 2007.

[18] L.D.P.A.J. Amouroux. Time-resolved laser-induced breakdown spectroscopy: application for qualitative and quantitative detection of fluorine, chlorine, sulfur, and carbon in air. *Applied spectroscopy*, 52(10):1321–1327, 1998.

[19] G. Arca, A. Ciucci, V. Palleschi, S. Rastelli, and E. Tognoni. Trace element analysis in water by the laser-induced breakdown spectroscopy technique. *Applied spectroscopy*, 51(8):1102–1105, 1997.

[20] R. Barbini, F. Colao, R. Fantoni, A. Palucci, and F. Capitelli. Application of laser-induced breakdown spectroscopy to the analysis of metals in soils. *Applied Physics A: Materials Science & Processing*, 69(7):175–178, 1999.

[21] JA Aguilera, C. Aragon, and J. Campos. Determination of carbon content in steel using laser-induced breakdown spectroscopy. *Applied spectroscopy*, 46(9):1382–1387, 1992.

[22] R. Noll, H. Bette, A. Brysch, M. Kraushaar, I. M
"onch, L. Peter, and V. Sturm. Laser-induced breakdown spectrometry–

applications for production control and quality assurance in the steel industry* 1. *Spectrochimica Acta Part B: Atomic Spectroscopy*, 56(6):637–649, 2001.

[23] V. Sturm, L. Peter, and R. Noll. Steel analysis with laser-induced breakdown spectrometry in the vacuum ultraviolet. *Applied Spectroscopy*, 54(9):1275–1278, 2000.

[24] V. Sturm, J. Vrenegor, R. Noll, and M. Hemmerlin. Bulk analysis of steel samples with surface scale layers by enhanced laser ablation and libs analysis of c, p, s, al, cr, cu, mn and mo. *Journal of analytical atomic spectrometry*, 19(4):451–456, 2004.

[25] F. Colao, R. Fantoni, V. Lazic, and V. Spizzichino. Laser-induced breakdown spectroscopy for semi-quantitative and quantitative analyses of artworks–application on multi-layered ceramics and copper based alloys* 1. *Spectrochimica Acta Part B: Atomic Spectroscopy*, 57(7):1219–1234, 2002.

[26] O. Samek, D.C.S. Beddows, J. Kaiser, S.V. Kukhlevsky, M. Liška, H.H. Telle, and J. Young. Application of laser-induced breakdown spectroscopy to in situ analysis of liquid samples. *Optical Engineering*, 39:2248, 2000.

[27] E. Tognoni, V. Palleschi, M. Corsi, and G. Cristoforetti. Quantitative micro-analysis by laser-induced breakdown spectroscopy: a review of the experimental approaches* 1. *Spectrochimica Acta Part B: Atomic Spectroscopy*, 57(7):1115–1130, 2002.

[28] W.D. Callister and D.G. Rethwisch. *Fundamentals of materials science and engineering: an integrated approach*. Wiley, 2011.

[29] J. Vrenegor, R. Noll, and V. Sturm. Investigation of matrix effects in laser-induced breakdown spectroscopy plasmas of high-alloy steel for matrix and minor elements. *Spectrochimica Acta Part B: Atomic Spectroscopy*, 60(7):1083–1091, 2005.

[30] MA Khater, P. Kampen, JT Costello, JP Mosnier, and ET Kennedy. Time-integrated laser-induced plasma spectroscopy in the vacuum ultraviolet for the quantitative elemental characterization of steel alloys. *Journal of Physics D: Applied Physics*, 33:2252, 2000.

[31] M.A. Khater, J.T. Costello, and E.T. Kennedy. Optimization of the emission characteristics of laser-produced steel plasmas in the vacuum ultravio-

let: significant improvements in carbon detection limits. *Applied Spectroscopy*, 56(8):970–983, 2002.

[32] J. Debras-Guédon and N. Liodec. De l'utilisation du faisceau d'un amplificateur a ondes lumineuses par émission induite de rayonnement (laser à rubis), comme source énergétique pour l'excitation des spectres démission des éléments. *CR Acad. Sci*, 257:3336, 1963.

[33] L. Moenke-Blankenburg. *Laser microanalysis*, volume 105. Wiley-Interscience, 1989.

[34] WW Schroeder, JJ Van Niekerk, L. Dicks, A. Strasheim, and H. Piepen. A new electronic time resolution system for direct reading spectrometers and some applications in the diagnosis of spark and laser radiations. *Spectrochimica Acta Part B: Atomic Spectroscopy*, 26(6):331–336, 1971.

[35] H. van der Piepen and WW Schroeder. Recording of transient spectra. *Spectrochimica Acta Part B: Atomic Spectroscopy*, 26(8):471–475, 1971.

[36] R. Menzies. Laser heterodyne detection techniques. *Laser Monitoring of the Atmosphere*, pages 297–353, 1976.

[37] L.N. Koppel. Active-recording x-ray crystal spectrometer for laser-induced plasmas. *Review of Scientific Instruments*, 47(9):1109–1112, 1976.

[38] J. Brunol, R. Sauneuf, and JP Gex. Micro coded aperture imaging applied to laser plasma diagnosis. *Optics Communications*, 31(2):129–134, 1979.

[39] JG Fujimoto, WZ Lin, EP Ippen, CA Puliafito, and RF Steinert. Time-resolved studies of nd: Yag laser-induced breakdown. plasma formation, acoustic wave generation, and cavitation. *Investigative ophthalmology & visual science*, 26(12):1771, 1985.

[40] BKF Young, RE Stewart, CJ Cerjan, G. Charatis, and G.E. Busch. Time-resolved measurement of coronal temperature and line-intensity profiles in laser-produced plasmas. *Physical review letters*, 61(25):2851–2854, 1988.

[41] F. Docchio, P. Regondi, M.R.C. Capon, and J. Mellerio. Study of the temporal and spatial dynamics of plasmas induced in liquids by nanosecond nd: Yag laser pulses. 2: Plasma luminescence and shielding. *Applied Optics*, 27(17):3669–3674, 1988.

[42] K.W. Marich, P.W. Carr, W.J. Treytl, and D. Glick. Effect of matrix material on laser-induced elemental spectral emission. *Analytical Chemistry*, 42(14):1775–1779, 1970.

[43] W. Lauterborn. High-speed photography of laser-induced breakdown in liquids. *Applied Physics Letters*, 21(1):27–29, 1972.

[44] VS Teslenko. Investigation of photoacoustic and photohydrodynamic parameters of laser breakdown in liquids. *Soviet Journal of Quantum Electronics*, 7:981, 1977.

[45] DE Lencioni. The effect of dust on 10.6-μm laser-induced air breakdown. *Applied Physics Letters*, 23(1):12–14, 1973.

[46] L.J. Radziemski, T.R. Loree, D.A. Cremers, and N.M. Hoffman. Time-resolved laser-induced breakdown spectrometry of aerosols. *Analytical Chemistry*, 55(8):1246–1252, 1983.

[47] C. Girault, D. Damiani, J. Aubreton, and A. Catherinot. Time-resolved spectroscopic study of the krf laser-induced plasma plume created above an ybacuo superconducting target. *Applied physics letters*, 55(2):182–184, 1989.

[48] D.A. Cremers and L.J. Radziemski. Direct detection of beryllium on filters using the laser spark. *Applied spectroscopy*, 39(1):57–63, 1985.

[49] L.J. Radziemski, D.A. Cremers, and T.R. Loree. Detection of beryllium by laser-induced-breakdown spectroscopy. *Spectrochimica Acta Part B: Atomic Spectroscopy*, 38(1-2):349–355, 1983.

[50] D.A. Cremers and L.J. Radziemski. Detection of chlorine and fluorine in air by laser-induced breakdown spectrometry. *Analytical Chemistry*, 55(8):1252–1256, 1983.

[51] J.R. Wachter and D.A. Cremers. Determination of uranium in solution using laser-induced breakdown spectroscopy. *Applied spectroscopy*, 41(6):1042–1048, 1987.

[52] M. Essien, L.J. Radziemski, and J. Sneddon. Detection of cadmium, lead and zinc in aerosols by laser-induced breakdown spectrometry. *J. Anal. At. Spectrom.*, 3(7):985–988, 1988.

[53] K.J. Grant and G.L. Paul. Electron temperature and density profiles of excimer laser-induced plasmas. *Applied spectroscopy*, 44(8):1349–1354, 1990.

[54] M. Sabsabi and P. Cielo. Quantitative analysis of aluminum alloys by laser-induced breakdown spectroscopy and plasma characterization. *Applied spectroscopy*, 49(4):499–507, 1995.

[55] K.J. Mason and J.M. Goldberg. Characterization of a laser plasma in a pulsed magnetic field. part i: Spatially resolved emission studies. *Applied spectroscopy*, 45(3):370–379, 1991.

[56] CB Winstead, KX He, D. Grantier, T. Hammond, and JL Gole. Electric-field-enhanced laser-induced plasma spectroscopy of jet-cooled silicon trimer. *Chemical physics letters*, 181(2-3):222–231, 1991.

[57] J.E. Carranza and D.W. Hahn. Assessment of the upper particle size limit for quantitative analysis of aerosols using laser-induced breakdown spectroscopy. *Analytical chemistry*, 74(21):5450–5454, 2002.

[58] S. Rosenwasser, G. Asimellis, B. Bromley, R. Hazlett, J. Martin, T. Pearce, and A. Zigler. Development of a method for automated quantitative analysis of ores using libs* 1. *Spectrochimica Acta Part B: Atomic Spectroscopy*, 56(6):707–714, 2001.

[59] CM Davies, HH Telle, DJ Montgomery, and RE Corbett. Quantitative analysis using remote laser-induced breakdown spectroscopy (libs). *Spectrochimica Acta Part B: Atomic Spectroscopy*, 50(9):1059–1075, 1995.

[60] DA Cremers, JE Barefield, and AC Koskelo. Remote elemental analysis by laser-induced breakdown spectroscopy using a fiber-optic cable. *Applied spectroscopy*, 49(6):857–860, 1995.

[61] B.J. Marquardt, S.R. Goode, and S.M. Angel. In situ determination of lead in paint by laser-induced breakdown spectroscopy using a fiber-optic probe. *Analytical Chemistry*, 68(6):977–981, 1996.

[62] B.J. Marquardt, D.N. Stratis, D.A. Cremers, and S.M. Angel. Novel probe for laser-induced breakdown spectroscopy and raman measurements using an imaging optical fiber. *Applied spectroscopy*, 52(9):1148–1153, 1998.

[63] JD Blacic, DR Pettit, DA Cremers, and N. Roessler. Laser-induced breakdown spectroscopy for remote elemental analysis of planetary surfaces. Technical report, Los Alamos National Lab., NM (United States), 1992.

[64] KY Kane and DA Cremers. Remote elemental analysis of planetary surfaces using laser-induced breakdown spectroscopy. In *Lunar and Planetary Institute Science Conference Abstracts*, volume 23, page 651, 1992.

[65] A.K. Knight, N.L. Scherbarth, D.A. Cremers, and M.J. Ferris. Characterization of laser-induced breakdown spectroscopy (libs) for application to space exploration. *Applied Spectroscopy*, 54(3):331–340, 2000.

[66] R.C. Wiens, R.E. Arvidson, D.A. Cremers, M.J. Ferris, J.D. Blacic, F.P. Seelos IV, and K.S. Deal. Combined remote mineralogical and elemental identification from rovers: Field and laboratory tests using reflectance and laser-induced breakdown spectroscopy. *Journal of geophysical research*, 107(E11):8003, 2002.

[67] T. Namioka. Theory of the ellipsoidal concave grating. i. *JOSA*, 51(1):4–12, 1961.

[68] D. Vasileska. Pn junction lab @ONLINE, May 2011.

[69] Yeats P. *A spectroscopic and diagnostic study of laser plasma generation and evolution using multi-variable target conditioning*. PhD thesis, Dublin City University, Dublin, Ireland, 2004.

[70] R. Sattmann, V. Sturm, and R. Noll. Laser-induced breakdown spectroscopy of steel samples using multiple Q-switch Nd: YAG laser pulses. *Journal of Physics D: Applied Physics*, 28:2181, 1995.

[71] C. Gautier, P. Fichet, D. Menut, J.L. Lacour, D. L'Hermite, and J. Dubessy. Main parameters influencing the double-pulse laser-induced breakdown spectroscopy in the collinear beam geometry. *Spectrochimica Acta Part B: Atomic Spectroscopy*, 60(6):792–804, 2005.

[72] V. Hohreiter and DW Hahn. Dual-pulse laser induced breakdown spectroscopy: Time-resolved transmission and spectral measurements. *Spectrochimica Acta Part B: Atomic Spectroscopy*, 60(7-8):968–974, 2005.

[73] D.N. Stratis, K.L. Eland, and S.M. Angel. Dual-pulse LIBS using a pre-ablation spark for enhanced ablation and emission. *Applied Spectroscopy*, 54(9):1270–1274, 2000.

[74] R. Noll, R. Sattmann, V. Sturm, and S. Winkelmann. Space-and time-resolved dynamics of plasmas generated by laser double pulses interacting with metallic samples. *J. Anal. At. Spectrom.*, 19(4):419–428, 2004.

[75] G. Cristoforetti, S. Legnaioli, V. Palleschi, A. Salvetti, and E. Tognoni. Influence of ambient gas pressure on laser-induced breakdown spectroscopy technique in the parallel double-pulse configuration. *Spectrochimica Acta Part B: Atomic Spectroscopy*, 59(12):1907–1917, 2004.

[76] SS Harilal, CV Bindhu, MS Tillack, F. Najmabadi, and AC Gaeris. Internal structure and expansion dynamics of laser ablation plumes into ambient gases. *Journal of applied physics*, 93:2380, 2003.

[77] G. Taylor. The formation of a blast wave by a very intense explosion. I. Theoretical discussion. *Proceedings of the Royal Society of London. Series A, Mathematical and Physical Sciences*, pages 159–174, 1950.

[78] SS Harilal, RW Coons, P. Hough, and A. Hassanein. Influence of spot size on extreme ultraviolet efficiency of laser-produced sn plasmas. *Applied Physics Letters*, 95:221501, 2009.

[79] D. Colombant and GF Tonon. X-ray emission in laser-produced plasmas. *Journal of Applied Physics*, 44(8):3524–3537, 1973.

[80] R. Ahmed and M.A. Baig. A comparative study of single and double pulse laser induced breakdown spectroscopy. 2009.

[81] C. Gautier, P. Fichet, D. Menut, and J. Dubessy. Applications of the double-pulse laser-induced breakdown spectroscopy (LIBS) in the collinear beam geometry to the elemental analysis of different materials. *Spectrochimica Acta Part B: Atomic Spectroscopy*, 61(2):210–219, 2006.

[82] L. St-Onge, V. Detalle, and M. Sabsabi. Enhanced laser-induced breakdown spectroscopy using the combination of fourth-harmonic and fundamental Nd: YAG laser pulses. *Spectrochimica Acta Part B: Atomic Spectroscopy*, 57(1):121–135, 2002.

[83] C. Gautier, P. Fichet, D. Menut, J.L. Lacour, D. L'Hermite, and J. Dubessy. Quantification of the intensity enhancements for the double-pulse laser-induced breakdown spectroscopy in the orthogonal beam geometry. *Spectrochimica Acta Part B: Atomic Spectroscopy*, 60(2):265–276, 2005.

[84] A. Santagata, A. De Bonis, P. Villani, R. Teghil, and GP Parisi. Fs/ns-dual-pulse orthogonal geometry plasma plume reheating for copper-based-alloys analysis. *Applied Surface Science*, 252(13):4685–4690, 2006.

[85] D.N. Stratis, K.L. Eland, and S.M. Angel. Effect of pulse delay time on a pre-ablation dual-pulse LIBS plasma. *Applied Spectroscopy*, 55(10):1297–1303, 2001.

[86] G. Cristoforetti, S. Legnaioli, V. Palleschi, A. Salvetti, and E. Tognoni. Characterization of a collinear double pulse laser-induced plasma at several ambient gas pressures by spectrally-and time-resolved imaging. *Applied Physics B: Lasers and Optics*, 80(4):559–568, 2005.

[87] D.A. Cremers, L.J. Radziemski, and T.R. Loree. Spectrochemical analysis of liquids using the laser spark. *Applied spectroscopy*, 38(5):721–729, 1984.

[88] J. Scaffidi, S.M. Angel, and D.A. Cremers. Emission enhancement mechanisms in dual-pulse libs. *Analytical chemistry*, 78(1):24–32, 2006.

[89] L. Radziemski, D.A. Cremers, K. Benelli, C. Khoo, and R.D. Harris. Use of the vacuum ultraviolet spectral region for laser-induced breakdown spectroscopy-based martian geology and exploration. *Spectrochimica Acta Part B: Atomic Spectroscopy*, 60(2):237–248, 2005.

[90] X. Mao, X. Zeng, S.B. Wen, and R.E. Russo. Time-resolved plasma properties for double pulsed laser-induced breakdown spectroscopy of silicon. *Spectrochimica Acta Part B: Atomic Spectroscopy*, 60(7):960–967, 2005.

[91] VI Babushok, FC DeLucia, et al. Double pulse laser ablation and plasma: Laser induced breakdown spectroscopy signal enhancement. *Spectrochimica Acta Part B: Atomic Spectroscopy*, 61(9):999–1014, 2006.

[92] J. Richter. Radiation of hot gases, ch. 1 in plasma diagnostics, ed. w. lochte-holtgreven, 1968.

List of Figures

1 Outline of the thesis. vii

1.1 The geometric volume-element considered in the derivation of the equation of radiative transfer for a beam of light confined to the solid angle $d\Omega$ ([10]). 13

3.1 Basic LIBS experimental layout. 29
3.2 Surelite III-10 Laser Optical Layout. 30
3.3 Target chamber and associated vacuum and optical components. . . 33
3.4 Target XYZ Manipulater (at the backside of the target chamber). . . . 34
3.5 Target carousel loaded with six steel targets with varying carbon concentrations. 34
3.6 Microscope image of a typical GCA (from Burle Industries Inc.). . . . 36
3.7 ARC VM-521 Spectrometer. 37
3.8 Rowland Circle. 38
3.9 Off-Rowland mount configuration. 40
3.10 MOS capacitor structure. 43
3.11 Design of a CCD. 44

4.1 Top panel: Modulation of the 97.7 nm line intensity resulting from the laser pulse energy modulation shown in the panel below. Bottom panel: Modulation of the laser pulse energy obtained with the aid of a halfwave plate and a high power polariser combination. 46
4.2 Schematic diagram of the observing position and the TISR scheme. . 48
4.3 C^{2+} 97.7 nm line intensity (4.3a) and signal to background ratio (SBR) (4.3b) at different observing positions along the z-axis. 50
4.4 Effect of accumulated shots number on intensity (4.4a) and signal-to-background ratio (SBR) (4.4b) in vacuum (■) and nitrogen at 0.1 mbar (●), 0.5 mbar (▲) and 1.0 mbar (▼). 52

4.5 Series of carbon spectra from a graphite sample recorded with the LIBS system. 53
4.6 Wavelength calibration of carbon spectrum - step 1: composite carbon VUV spectrum (graphite sample). 54
4.7 Wavelength calibration of carbon spectrum - step 2: spectral line reference and identification according to NIST. 54
4.8 A typical VUV spectrum containing carbon and sulphur lines obtained from a steel plasma. 55
4.9 Interior referencing applied to calibration of C^{2+} 97.7 nm line intensity. 57
4.10 Basic LIBS analysis procedure. 60

5.1 Experimental settings for dual-pulse LIBS VUV emission in ambient gas environment. 63
5.2 Inter-pulse delay time generation system. 65
5.3 A spectra comparison of single- and double-pulse excitation with different energies. 67
5.4 Intensity dependence on inter-pulse delay time of several spectral lines in vacuum condition: C^{2+}97.7nm(■), C^{+}90.41nm(●), Fe^{2+}98.4nm(▲) and Fe^{2+}89.12nm(▼). Spectron laser (1064 nm, 15 ns, 200 mJ) and Surelite laser (1064 nm, 6 ns, 665 mJ) in dual-pulse collinear reheating mode. 70
5.5 The peak intensity as a function of inter-pulse delay within the first 600 ns. C^{2+} 97.7 nm line. Spectron laser (1064 nm, 15 ns, 200 mJ) and Surelite laser (1064 nm, 6 ns, 665 mJ) in dual-pulse collinear reheating mode in vacuum. 71
5.6 Emission intensity as a function of ambient gas pressure in helium with pressure from 0 to 400 mbar (a), a close look at the first 10 mbar in helium (b), in argon (c) and in nitrogen (d). Spectral lines presented: C^{2+}97.7 nm(■), C^{+}90.41 nm(●), Fe^{2+}98.39 nm(▲), Fe^{2+}89.12 nm(▼), gas element (N^{2+}91.6 nm or Ar^{+}91.98 nm)(◆). Spectron laser (1064 nm, 15 ns, 200 mJ) and Surelite laser (1064 nm, 6 ns, 665 mJ) in dual-pulse collinear reheating mode with inter-pulse delay 100ns. . . 74
5.7 Several VUV spectra under different argon pressures. Spectron laser(1064nm,15ns,200mJ) and Surelite laser(1064 nm, 6 ns, 665 mJ) in dual-pulse collinear reheating mode with inter-pulse delay 100 ns. 76

5.8 Influence of the nitrogen absorption on VUV emission. (a) Calculated nitrogen transmission curve for VUV radiation. (b) Recorded C^{2+} 97.7 nm line intensity from the spectrum. (c) Absorption corrected intensity compared to the recorded intensity. Spectron laser (1064 nm, 15 ns, 200 mJ) and Surelite laser (1064 nm, 6 ns, 665 mJ) in dual-pulse collinear reheating mode with inter-pulse delay 100ns. . . 78
5.9 Signal to background ratio (SBR) and line intensity plot in three types of gases: (a) Helium, (b) Argon and (c) Nitrogen. Spectron laser (1064 nm, 15 ns, 200 mJ) and Surelite laser (1064 nm, 6 ns, 665 mJ) in dual-pulse collinear reheating mode with inter-pulse delay 100 ns. 81

6.1 Effect of single-pulse laser beam defocusing. Intensities of C^{2+} 97.7 nm (■), S^{4+} 78.65 nm (●) and Fe^{2+}98.4 nm (▲) spectral lines are included. Plasma was generated by the Surelite laser (1064 nm, 6 ns, 665 mJ). The steel sample contains 0.041% carbon and 0.009% sulphur. The intensity of each line was normalized to unity for comparison reasons. Positive focus distance denotes that the laser beam was focused under the sample surface and negative position corresponds to the focus distance above the sample surface. 84
6.2 State of charge as a function of temperature for carbon, after Colombant and Tonon [79]. 85
6.3 Calculated dependence of electron temperature on laser power density and on focusing distance for carbon. 87
6.4 Effect of reheating laser beam defocusing in dual-pulse mode. Intensity of C^{2+} 97.7 nm line was recorded in vacuum (■) and three types of ambient gases: nitrogen at 0.3 mbar (●), argon at 1.5 mbar (▲) and helium at 28 mbar (▼). Intensities were normalized to (0,1) for easy comparison. Dual-pulse experiment was performed by the Spectron laser (1064 nm,15 ns,200 mJ) and the Surelite laser (1064 nm,6 ns,665 mJ) in collinear reheating mode with 100 ns inter-pulse delay. Positive focus distance indicates that the second laser beam was focused under the sample surface, negative distance corresponds to the above-surface defocusing. 89

7.1 Variation of C^{2+} 97.7 nm line intensity with inter-pulse delay time in nitrogen at 1.0 mbar, in argon at 2.1 mbar, in helium at 25 mbar and in vacuum (10^{-6} mbar). Spectron laser (1064 nm, 15 ns, 200 mJ) and Surelite laser (1064 nm, 6 ns, 665 mJ) in dual-pulse collinear reheating mode. 94
7.2 Trends in the C^{2+} 97.7 nm line intensity dependence on the inter-pulse delay time in the range of 0 - 600 ns. 4th polynomial fits were applied to the profiles for nitrogen at 1.0 mbar, argon at 2.1 mbar and helium at 25 mbar, corresponding to figure 7.1. 96
7.3 C^{2+} 97.7 nm line intensity dependence on inter-pulse delay time in nitrogen at several pressures. Spectron laser (1064 nm, 15 ns, 200 mJ) and Surelite laser (1064 nm, 6 ns, 665 mJ) in dual-pulse collinear reheating mode. 97
7.4 C^{2+} 97.7 nm line intensity dependence on inter-pulse delay time in helium at several pressures. Spectron laser (1064 nm, 15 ns, 200 mJ) and Surelite laser (1064 nm, 6 ns, 665 mJ) in dual-pulse collinear reheating mode. 99
7.5 C^{2+} 97.7 nm line intensity dependence on inter-pulse delay time in argon at several pressures. Spectron laser (1064 nm, 15 ns, 200 mJ) and Surelite laser (1064 nm, 6 ns, 665 mJ) in dual-pulse collinear reheating mode. 100
7.6 Comparison of the intensity enhancement vs. pressure at the 100 ns peak and at the 2 μs plateau. The intensity enhancement is indicated by the relative intensity of 100 ns peak to 0 ns starting point ($R_{peak} = I_{100ns}/I_{0ns}$) and the relative intensity of the plateau to the starting point ($R_{plateau} = I_{2\mu s}/I_{0ns}$), corresponding to the intensities recorded in figure 7.5. Spectron laser (1064 nm, 15 ns, 200 mJ) and Surelite laser (1064 nm, 6 ns, 665 mJ) in dual-pulse collinear reheating mode. 101
7.7 The intensity ratio of the plateau to the initial point (simultaneous pulses) vs. argon pressure. Spectron laser (1064 nm, 15 ns, 200 mJ) and Surelite laser (1064 nm, 6 ns, 665 mJ) in dual-pulse collinear reheating mode. Other settings were the same as in figure 7.5. 103
7.8 The intensity ratio of the plateau to the initial point (simultaneous pulses) vs. nitrogen pressure. Spectron laser (1064 nm, 15 ns, 200 mJ) and Surelite laser (1064 nm, 6 ns, 665 mJ) in dual-pulse collinear reheating mode. Other settings were the same as in figure 7.3. 104

7.9 The intensity ratio of the plateau to the initial point (simultaneous pulses) vs. helium pressure. Spectron laser (1064 nm, 15 ns, 200 mJ) and Surelite laser (1064 nm, 6 ns, 665 mJ) in dual-pulse collinear reheating mode. Other settings were the same as in figure 7.4. 105
7.10 Intensity dependence on inter-pulse delay time in nitrogen at 0.91 mbar. Spectron laser (1064 nm, 15 ns, 200 mJ) and Surelite laser (1064 nm, 6 ns, 665 mJ) in dual-pulse collinear reheating mode. 107

8.1 Imaging study of single-pulse produced aluminum plasma expanding in a background of the pressure of 1×10^{-6} Torr, by Harilal et al. [76]. 111
8.2 Imaging study of single-pulse produced aluminum plasma expanding in air at 1.3 Torr by Harilal et al. [76]. 112
8.3 Schematic illustration of the phased enhancement during the dual-pulse excitation process. 115
8.4 Gautier's work in 2005 [71]. Inter-pulse delay effect on Mg neutral line and Mg II line. The reported optimal Δt for Mg I was 0.2 μs and 5 - 12.5 μs for Mg II. However a small "peak" within 1 μs was shown on the Mg II intensity curve. 118
8.5 Gautier's work in 2006 [81]. Inter-pulse delay effect on several lines from steel sample. 119
8.6 Sattmann's work in 1995 [70]. Two peaks are clearly shown on the intensity curve with a comparison of the electron temperature and density. Coloured dashed lines and the arrows were drawn as guide lines for viewing. 120
8.7 Hohreiter's work in 2005 [72]. Two peaks were clearly shown on the signal-to-noise ratio (SNR) of Mg I and Si I lines. The author reported two optimal inter-pulse delays of 5 μs and 20 μs. 121
8.8 Ahmed's work in 2009 [80]. Two peaks were clearly shown on the intensity curve of several spectral lines, but the optimal inter-pulse delay was reported to be 25 μs and no discussion on the 1st peak. . . 122

9.1 Calibration curves of limit of detection (LOD) using C^{2+} 97.7 nm. Surelite laser (1064 nm, 6 ns, 665 mJ) in single pulse mode. The straight red line is a linear fit to the experimental intensity values. . 126

9.2 Calibration curves of limit of detection (LOD) using C^{2+} 97.7 nm. Spectron laser (1064 nm, 15 ns, 200 mJ) as ablation laser and Surelite laser (1064 nm, 6 ns, 665 mJ) as reheating laser in collinear dual-pulse geometry. Inter-pulse separation was 100 ns. The straight red line is a linear fit to the experimental intensity values. 127
9.3 Calibration curves of limit of detection (LOD) using S^{4+} 78.65 nm. Surelite laser (1064 nm, 6 ns, 665 mJ) in single pulse mode. 129
9.4 Calibration curves of limit of detection (LOD) using S^{4+} 78.65 nm. Spectron laser (1064 nm, 15 ns, 200 mJ) as ablation laser and Surelite laser (1064 nm, 6 ns, 665 mJ) as reheating laser in collinear dual-pulse geometry. Inter-pulse separation was 100 ns. 130
9.5 Calibration curve and derived limit of detection (LOD) using C^{2+} 97.7 nm. Spectron laser (1064 nm, 15 ns, 200 mJ) as ablation laser and Surelite laser (1064 nm, 6 ns, 665 mJ) as reheating laser were in collinear dual-pulse geometry with argon environment at 1.5 mbar. Inter-pulse separation was 100 ns. The straight red line is a linear fit to the experimental intensity values. 134
9.6 Calibration curve of limit of detection (LOD) using S^{4+} 78.65 nm. Spectron laser (1064 nm, 15 ns, 200 mJ) as ablation laser and Surelite laser (1064 nm, 6 ns, 665 mJ) as reheating laser were in collinear dual-pulse geometry with nitrogen environment at 0.2 mbar. Inter-pulse separation was 100 ns. The straight red line is a linear fit to the experimental intensity values. 135

C.1 Spontaneous and stimulated emission and absorption of radiation. . 152

D.1 Intensity dependence on inter-pulse delay time in argon at 1.3 mbar. 155
D.2 Intensity dependence on inter-pulse delay time in helium at 250 mbar. 156

List of Tables

2.1 List of topics discussed at LIBS-2008 conference 24
2.2 List of topics at LIBS-2010 conference 25

3.1 The steel samples used in the work reported in this thesis. The concentration is given in weight/weight percent (W/W%) which is normally defined as 100 $\times$ the ratio of the solute weight to the solution weight. Here the solute is the carbon (analyte) content (in grams) and the solution is the Fe (matrix) weight (also in grams). 35

5.1 Factors affecting quantitative LIBS analysis 62
5.2 Main technical specifications of the two lasers used in dual pulse VUV LIBS experiments. 64
5.3 Comparison of C^{2+} 97.7 nm line peak intensity in single-pulse (SP) and double-pulse (DP) configurations. 68

8.1 Summary of recent studies on inter-pulse delay time. ^{*1} C - collinear; O - orthogonal; ^{*2} air pressure vary from 0 to 1atm; ^{*3} dual-pulse is performed by one nanosecond laser, other cases are two lasers ^{*4} femtosecond laser is employed as pre-spark pulse with nanosecond laser as ablation pulse, other conditions are all with nanosecond lasers, other conditions are nanosecond lasers 117

9.1 Parameters as optimized in the current work for LOD calibration for C and S in steel using LIBS technique. 125
9.2 Statistics of LOD calibration of C in steel in various environments. . 131
9.3 Improvement on LOD values, result comparison based on improvement of LOD gain coefficient α. Data for C in steel derived from table 9.2. 132
9.4 LOD values in the literature compared to our results 136